9-2022

Finite Fatigue Life Prediction of Additively Manufactured Aircraft Engine Turbine Blade with Respect to Internal Defect Size and Location

Daniel G. Miller

Finite Fatigue Life Prediction of Additively Manufactured Aircraft Engine Turbine Blade with Respect to Internal Defect Size and Location

DISSERTATION

Daniel G. Miller, Maj, USAF

AFIT-ENY-DS-22-S-132

DEPARTMENT OF THE AIR FORCE
AIR UNIVERSITY

AIR FORCE INSTITUTE OF TECHNOLOGY

Wright-Patterson Air Force Base, Ohio

AFIT-ENY-DS-22-S-132

FINITE FATIGUE LIFE PREDICTION OF ADDITIVELY MANUFACTURED AIRCRAFT ENGINE TURBINE BLADE FOR INTERNAL DEFECT SIZE AND LOCATION

DISSERTATION

Presented to the Faculty

Graduate School of Engineering and Management

Air Force Institute of Technology

Air University

Air Education and Training Command

in Partial Fulfillment of the Requirements for the

Degree of Doctorate of Philosophy in Astronautical Engineering

Daniel G. Miller, B.S.; M.S.

Maj, USAF

15 September 2022

AFIT-ENY-DS-22-S-132

FINITE FATIGUE LIFE PREDICTION OF ADDITIVELY MANUFACTURED AIRCRAFT ENGINE TURBINE BLADE FOR INTERNAL DEFECT SIZE AND LOCATION

DISSERTATION

Daniel G. Miller, B.S.; M.S.
Maj, USAF

Committee Membership:

Ramana Grandhi, Ph.D.
Chair

Maj Ryan A. Kemnitz, Ph.D.
Co-Chair

Christine Schubert-Kabban, Ph.D.
Reader

Luke C. Sheridan, Ph.D.
Reader

Abstract

Current fatigue life modeling techniques with respect to defects emphasize the dependence on the defect size with respect to fatigue life, but does not account for the effects of where a defect might be located. This research outlines a process to include defect location into the model analysis for a more precise prediction of the number of cycles to failure and where the finial failure could occur within a component. The focus is on a turbine blade structure using IN718 subjected to a pure vibratory load. The basic model predicts component life using a stress map from the frequency analysis of the developed Finite Element Model (FEM) and synthetically generated defect sizes and location. Test specimens printed in IN718 are used to create experimental data to validate the model parameters, defect distributions, and predictions. The proposed results will be a map denoting the critical locations that may cause failure and predictions of fatigue life when both defect size and location are taken into consideration.

Acknowledgements

This research would not have been possible without the support and understanding from my wife and children. They are the bedrock that supported me.

To my committee: Thank You. Each of you brought a different skill set to the table, and played a crucial roll in bringing the research pieces into a cohesive analysis. Dr. Grandhi, your insights into the Ph.D. process, your lessons on how to write a good paper will stay with me for life. By discussing the hows and whys of becoming a Ph.D., the tasks became understandable. Maj Kemnitz, your expertise in the AM process, and knowledge in reading a fracture surface as easy as a book provided insights that I might never have seen. Dr. Schubert-Kabban, by further educating me in statistics, you gave me the words to explain the data. Your constant support and positive words encouraged me to reach further. Dr. Sheridan, I stand on your shoulders. Without the developments from your own research, this project would not have happened. Your constant feedback and use of your lab were crucial to my success.

I'm thankful for all the support from the TEFF Lab and across RQ. You all accepted me into your lab and treated me like family. Everyone was supportive and informative about the active research projects. For the use and support on the Vib Table, thank you Phil. For the assistance in wiring my test specimens to ensure I got great data, thank you Angie. For teaching me how to use the ATOS, thank you Trevor. For lending your expertise and turning point clouds into usable FEMs, thank you Alex. Finally, to Dr. Celli, you supported all of my day-to-day activities at the TEFF. Through teaching me how the equipment worked, demonstrating best practices for data collections, converting lab data into a usable format, and even running samples while I dealt with other problems, you easily prevented a dozen fatal testing mistakes.

Finally, to my colleagues and peers at AFIT (and many faculty not focused on my research). We all know that misery loves company, but being able to share lessons learned across departments was amazing. Having friends to sooth the stressful times and share in the milestone achievements made my time at AFIT. I've spent time de-stressing and celebrating little victories with too many of you to name everyone, but you know who you are, and you know that I deeply appreciated being able to steal some of your time.

Daniel G. Miller

Table of Contents

Page

Page

List of Figures

List of Tables

FINITE FATIGUE LIFE PREDICTION OF ADDITIVELY MANUFACTURED AIRCRAFT ENGINE TURBINE BLADE FOR INTERNAL DEFECT SIZE AND LOCATION

I. Introduction

1.1 Overview

Understanding how Additive Manufacturing (AM) defects impact fatigue life is vital to inspecting and certifying AM components in a high vibration environment such as a turbine engine. Literature demonstrated that defects such as voids, surface roughness, residual stress, and grain structure all impact the fatigue life in AM components [3, 4, 8, 14]. Each of these characteristics can be mitigated through optimized process control during the print or through post-processing steps. Some of the major process control steps are: laser scan speed, laser power, laser spot size, overlap between passes, and layer thickness. Modifications of these and other processing parameters impact the quantity and size of porous defect in the print [14, 15]. The impacts of residual stress and grain structure are mitigated through heat treatment processes [16, 17]. Surface roughness is mitigated through surface treatments such as polishing or machining, and the quantity and size of internal voids may be reduced through Hot Isostatic Press (HIP) [18].

Despite all of the developments into mitigating flaws, AM processes continue to exhibit defects that limit the fatigue life [3, 14, 19, 20]. Methods have been developed to predict the fatigue limit strength for a structure with respect to defect size [21, 22]. Recently the infinite life models have been extended to estimate finite life in the

presence of homogeneous uni-axial load cases [4, 11, 14]. To extend the finite life modeling to real world applications, a simulation process was developed to link the complex stress environments, such as the vibratory loading seen in a turbine engine, of a printed part with the finite life model. The final result was a method that drove damage tolerant design requirements based on the desired component life to define inspection criteria and critical locations to monitor.

By including an understanding of the defect formation process and a method to predict defect formations and their locations, the inverse problem can also be solved where the life of a part can be predicted by applying defect size and location data against the finite life model to determine the remaining life. To measure defects in an AM component, the popular method is Computed Tomography (CT) scans [14,19,23]. The CT scans directly measure the flaws in a part after manufacture. The process is valid for individual prints or as a statistical representation for consecutive print jobs which do not experience any anomalies [24].

1.2 Additive Manufacturing Applications

AM is gaining traction in the aerospace industry to create complex parts [25]. The largest challenge for using AM components in aircraft or spacecraft is the certification process [24, 26]. The AM process is currently viewed as a rapid prototype manufacturing process. However, by understanding how the AM process interacts with component design and loading, there is opportunity to create simplified certification processes for applications such as disposable hardware, temporary repairs, or satellites. In cases such as these, the environment that causes fatigue failure is limited in duration, allowing relaxed design criteria to meet the mission.

AM designs have been created and optimized for many different space applications from thrusters [27] and micro pumps [28] to chassis [29, 30] and support structures

[31–33]. There has been a lot of focus on the benefits AM brings to the space industry such as mass savings, multi-functional integration, part reduction, and reduced buy to fly costs to name a few [27, 29, 33–35]. However, very little has been published on fatigue life assessments due to AM defects.

One limitation for application of AM built components is certification due to defects inherent in the manufacturing process. While defect free AM parts are ideal for long life applications, often short design life systems are capable of meeting mission requirements despite generated defects. Accepting the realities of AM defects require the understanding that defects will impact the fatigue life [36, 37]. Previous works predicted a maximum design stress based on the maximum defect size and the infinite life El-Haddad model [32, 38]. The predicted maximum stresses created very conservative load estimates, buying back on the uncertainty risks associated with AM properties at the cost of extra mass.

On the aircraft front, significant weight savings are being achieved through optimization of wing spars [39]. Another application that will benefit from modeling fatigue life in the presence of defects are AM turbine blades. Turbine blades are complicated to machine using traditional manufacturing processes, but are relatively simple to print using AM processes. The AM process allows for quick manufacturing of novel designs for testing or to quickly build replacement parts to extend system life. This proposed research will extend the finite life models created under uni-axial, simple stress conditions where defect size is the driving constraint to predict the component life under a complex multi-axis stress environment which is driven by potential size and location of defects. One common alloy family used in manufacturing turbine blades are the nickel-based superalloys which includes Inconel 718 (IN718). IN718 is a popular material in the turbine engine industry due to its high corrosion and fatigue resistance. IN718 also maintains its strength at temperatures up to approximately

1600°F [40] enabling it to survive through engine operation environments [41].

1.3 Research Objectives

This research has:

1. (RO-1) Developed a finite fatigue life simulation that links defect size and location data with a Finite Element Model (FEM) to predict when a part will fail. If given a target life, the model is capable of predicting the critical regions of interest where failure due to internal defects is most likely to occur.

2. (RO-2) Performed a shaker table failure test on the printed components leveraging the 20 kilo pound shaker at the AFRL/RQTI Turbine Engine Fatigue Facility. Identified the size and location of the defect that caused failure.

3. (RO-3) Compared the finite fatigue life predicted results with the experimental test results. Analyzed the predictive quality of the finite fatigue life model and adjusted life prediction methodologies to better account for observed phenomena.

1.4 Contributions

1. Advanced the state of the art in modeling finite fatigue life with respect to defects by linking FEM outputs with defect dependent fatigue life modeling to incorporate defect location data (RO-1) (Chapter IV).

2. Advanced FEM techniques to encompass physical variations in the geometry of AM parts by a statistical study of deviations in printed components in relationship to the "as designed" geometry (RO-1) (Chapter III).

3. Developed a prediction technique for finite life components under complex stress states based on a modified El-Haddad finite life fatigue model and defect size/location data (RO-1) (Chapters IV & VI).

4. Developed criteria for identifying inspection criteria and critical failure locations in complex geometries (RO-1) (Chapters IV & VI).

5. Experimentally linked vibration fatigue life results with failure defect sizes and locations (RO-2) (Chapters IV & V).

6. Validated the finite fatigue life modeling predictions through experimental vibration-based bending tests (RO-3) (Chapter V).

1.5 Air Force Impacts

The Air Force Science and Technology Strategy 2030 listed five strategic capabilities. One of them was "Complexity, Unpredictability, and Mass" which cites additive manufacturing as a technological opportunity to advance. The strategy called for an augmentation of high-end platforms with low-end, inexpensive systems [42]. AM processes demonstrated the potential to diminish the dependence on expensive long lead hardware by enabling the quick manufacture of a part when it is needed [24]. The AM process reduces machining time for complex systems and enables joined functionality of parts to reduce the total system part count through changes in design limitations and manufacturing capabilities. Currently these benefits are countered by the higher defect generation, leading to a more complex part verification process [10].

NASA recognized the strengths that AM brings to space, but are concerned with the safe implementation of this rapidly changing technology [24]. The NASA Standard for Additively Manufactured Spaceflight Hardware by Laser Powder Bed Fusion in Metals in 2017 offered a conservative approach to requirements allowing the use

of AM in the spaceflight industry, while accounting for the development of defects in every component. The NASA standard required multiple witness samples to describe the potential defect population in an AM part process. Due to a lack of feedback control in current Laser Powder Bed Fusion (LPBF) systems, variability in the control, and lack of understanding of production failure methods, NASA also included periodic sampling to ensure that production parts are still acceptable [24]. The NASA standard required that all parts are subject to Non-Destructive Evaluation (NDE) for surface and volumetric defects, leaving it to design subject matter experts to define the inspection sensitivity and boundaries. The NDE is currently accomplished through techniques such as CT scans.

The Turbine Engine Structural Integrity Program (ENSIP) MIL-HDBK-1783B documented general requirements that need to be evaluated for the acquisition of turbine engines. ENSIP requirements ensured that the engine has the appropriate structural properties to perform the design mission for the required design service life [43]. Among the requirements was an initial flaw size requirement. The program suggested various flaw sizes that should be detected based on material, type of flaw, and inspection method used along with the reliability and confidence level for the detection of defects. The rationale was to establish the probable flaw size that can exist in a part to apply damage tolerance criteria. In the discussion of NDE techniques, ENSIP briefly discussed the use of Radiographic Inspection, of which CT scanning is a subset, to detect flaws at any depth in a metallic part. The process was listed as expensive, which was deemed a major disadvantage. CT scanning is a time intensive process which requires a skilled, trained technician to interpret the data and determine the best processing settings to highlight material voids and minimize scan artifacts.

ENSIP also established damage tolerant designs. The concept behind damage

tolerant design was to assure mission life in the presence of a defect. The damage tolerant design requirements specified detecting a crack two times the critical crack size as calculated from models such as the El-Haddad infinite life model. The El-Haddad model describes the transfer from defect free fatigue life predictions to the point where crack growth dominates fatigue life. The point of transition was defined as the critical crack length. [22]. ENSIP continued to specify that a component must be capable of surviving for at least two inspection cycles in the presence of a crack twice the critical crack length. The El-Haddad model has been modified to allow for arbitrary defect size/shape [8] and has been modified to predict finite life based on the defect size and cycle stress ratio [11]. RO-1 was designed to extend the modified El-Haddad model to include the effects of defect location in a multi-axis stress environment on the predicted design life of a component. RO-2 supplied the test data to quantify the predictive capabilities of an improved model.

1.6 Experimental Breakdown

The tasks required to perform the research broke down into three major categories. First, the modeling and simulation work which involved building the FEM and finite fatigue life model. The FEM was used to generate the stress and frequency analysis for the component of interest. The finite fatigue life model generated a fatigue life prediction based on the applied stress range and the defect size. Applied together, the models allowed for prediction of allowable defect sizes and locations for a given desired life and a life prediction based on the size and location of defects found in the part.

The second category was the creation and experimentation of the physical components. CT scanning proved in-feasible due to the combination of material density, geometry, and total volume to inspect. Instead, inspection of the experimental frac-

ture surfaces provided data on defect size and location formation. Surface scans of the test components generated the distribution of geometry variations that can be expected between the designed part and final AM processing. Performing a sine sweep on each component determined the optimal frequency to apply for each sample when the components were tested to failure with a steady single axis vibration excitation. Due to the complex geometry of the components, a uni-axial vibration test generated multi-axial stresses.

The third category of effort was applying results of the physical testing to validate the developed models. In addition to accounting for the statistical variations from the build process, samples were built to characterize the material properties generated in from this AM build. Samples for tension test and fatigue crack growth were printed along with the turbine blades parts to characterize the expected responses and to ensure that the processes applied in this research were consistent material properties from literature.

II. Literature Review

2.1 Overview

There are four primary elements that need to be established to model the expected fatigue life for an AM structure with respect to defect size and location: a Finite Element Model (FEM), a defect generation and distribution, material fatigue properties, and a fatigue life defect model.

Chapter II Reviews the literature associated with each topic. Section 2.2 discusses the relationship between FEMs and AM. This section also reviews FEMs used in literature for fatigue life testing as well as literature related to turbine blade modeling and load cases. Section 2.3 covers the creation of and the applicable mitigation steps for deformations due to the Additive Manufacturing (AM) process, as well as how to measure internal defects without destroying the test specimen. Section 2.4 discusses traditional fatigue life modeling and how AM processes can distort the material trends. Finally, section 2.5 walks through the creation of fatigue life estimates based on defects found on a component. Starting with infinite life modeling, modifications are developed to account for AM defects. The infinite life model is modified to enable finite fatigue life predictions which is the starting point for this research.

2.2 Finite Element Modeling (FEM)

Additive Manufacturing (AM) is an enabling technology to produce complex components designed from structural topology optimization of FEMs [44–46]. Highly efficient models generated from optimization solutions have been successfully produced and applied in many disciplines including the aerospace and medical fields. One example in the aerospace field is an optimized bracket arm for a satellite. The

bracket was designed for the minimum mass solution [32]. In the medical field, AM processes have been studied for bone implants. By scanning the bone geometries to be replaced, Finite Element Models (FEMs) have been optimized for minimum mass with constraints on the surface and required loads [47–49].

For fatigue modeling, an FEM is generally used to predict the maximum applied stresses along the principal axis based on the loading case of interest. Developing an FEM requires a geometry, load case, and mesh. Section 2.2.1 discusses open source turbine blade research in the realms of fatigue testing and AM creation. Section 2.2.2 briefly discusses turbine blade vibrational testing. Section 2.2.3 talks about the mesh types that have been used for vibration and fatigue modeling. Section 2.2.4 reviews the need to characterize the applied material properties and exact geometry of the AM print to improve the accuracy of an FEM representation.

2.2.1 FEM Geometry

The geometry of interest for this research is a turbine blade. Figure 1 is the turbine blade geometry being applied in this research. This geometry was previously used to characterize damping effects of enclosed pockets in the print design to quantify AM damping characteristics [50]. The same geometry, without internal pockets, will be applied for the fatigue life research with respect to process generated defects.

Due to the proprietary nature of turbine blades, there is not very much literature on fatigue life or testing procedures associated with operational turbine blades. The Air Force became interested in engine failure analysis in 1968, when two new engine designs failed on the test stands after thousands of hours of testing. These failures prompted the development of ENSIP to regulate the development and testing of engine designs [51].

Chinese researchers have been working on modeling Combined Cycle Fatigue

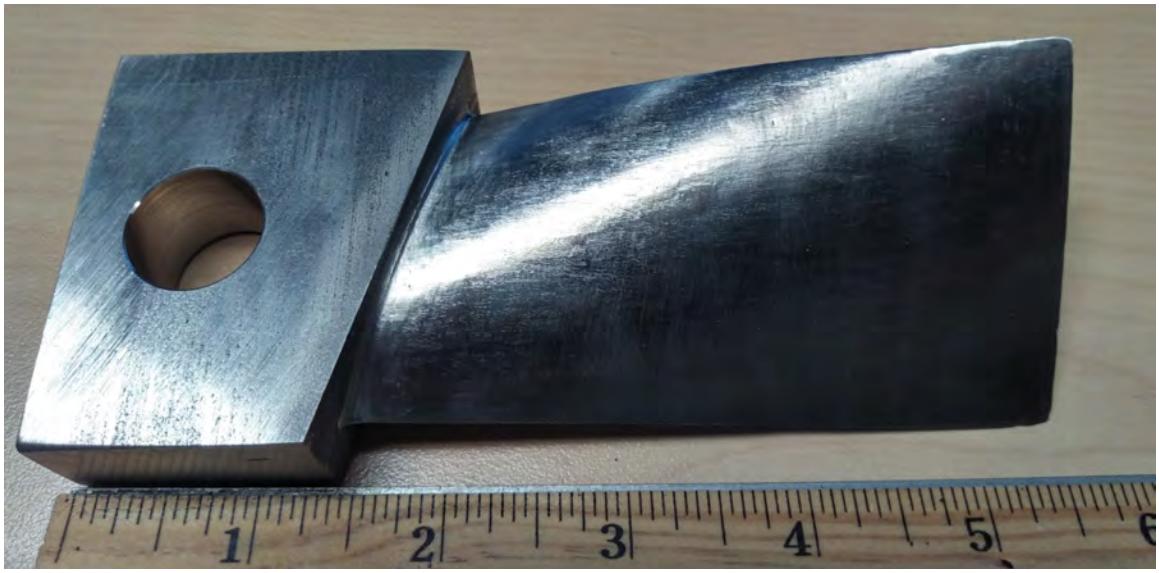

Figure 1. Printed turbine blade from IN718. This geometry was used to test damping of intentional voids in the blade. The same geometry will be applied for fatigue life in the presence of manufacturing defects.

(CCF) to account for simultaneous High Cycle Fatigue (HCF) and Low Cycle Fatigue (LCF). A variety of nickel-based superalloys such as single crystal SRR99 [52] and DZ125 [53] have been studied. None of these turbine blade studies involve Additive Manufacturing or defect-based modeling.

Oak Ridge National Labs (ORNL) has printed turbine blade structures in recent research to evaluate the printability of a new nickel-based superalloy [54]. The use of a turbine blade structure was to demonstrate printability of a long thin part (Fig. 2). The nickel-based superalloys are a popular family of materials for turbine blades due to the ability to maintain their high strength at elevated temperatures and the high corrosion and fatigue resistance [41].

The blade geometry to be tested in this research is a non-proprietary blade design created by AFRL for research studies as seen in Figure 3. This blade design has previously been used by Goldin with the addition of pockets of un-fused powder inside the blade to study AM unique damping opportunities [50].

Figure 2. Printed turbine blade sample from ORNL using a new variation of nickel-based superalloy [1].

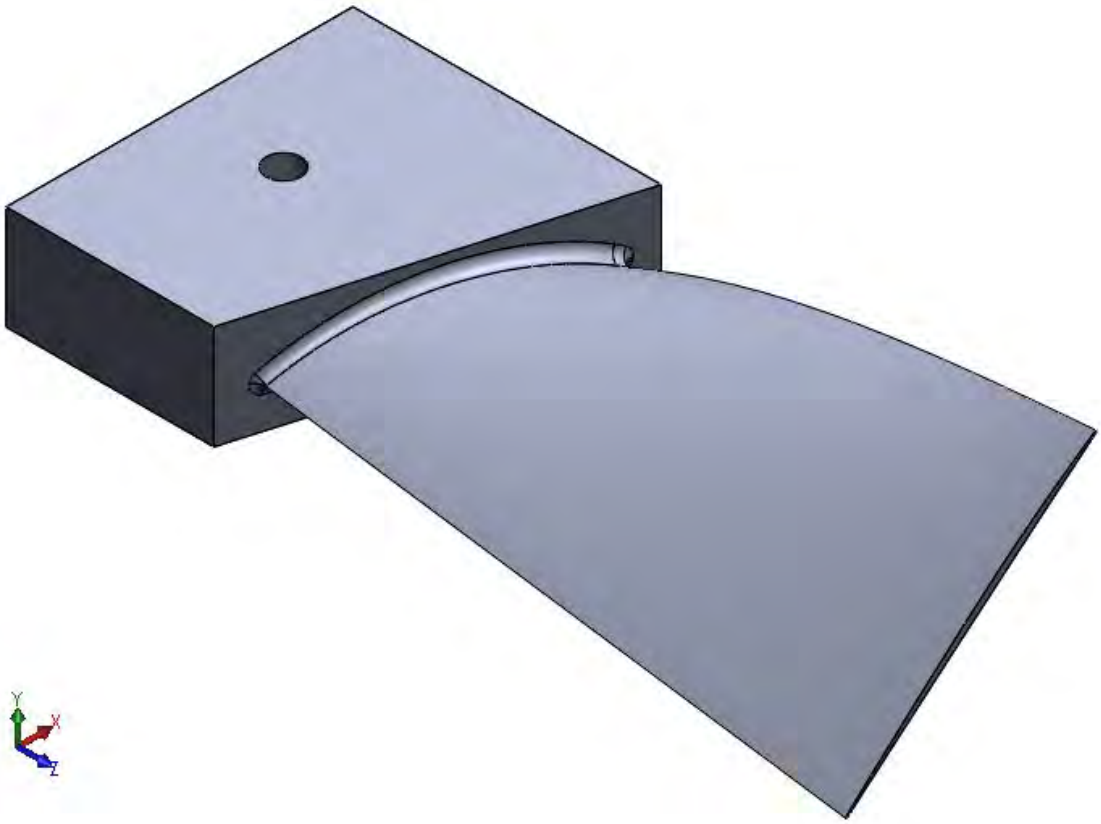

Figure 3. Research turbine blade of interest.

2.2.2 FEM Loading

High frequency vibrational inputs compose the majority of external excitation forces experienced by a turbine blade during operations. In a real-world system, there are several different frequencies associated with the engine configuration. However, there is typically one frequency that dominates the excitation. Therefore, frequency testing of turbine blades traditionally only apply a mono-frequency excitation force [55].

2.2.3 FEM Meshing

After identifying the geometry, a computer model of the part is analyzed using the FEM software of choice and the load case is applied. The computer model could come from the Computer Aided Design (CAD) file used to generate the printed part, or it could come from a scan of the part after manufacture. To account for part deformation and inaccuracies in the print geometry, this research will apply both methods to capture deviations in the printing process. The load case of interest is applied to the FEM to capture the minimum and maximum stresses in the part, generating the stress range seen at any given location.

To create an FEM, the element mesh type needs to be defined. There are four common element types used in literature [10, 56–58] for vibration and fatigue modeling: linear hexahedron (Lin Hex), quadratic hexahedron (Quad Hex), linear tetrahedral (Lin Tet), and quadratic tetrahedral (Quad Tet). Below are a few examples of each type used in similar research.

Chudzik [56] performed roller bearing fatigue predictions with a Lin Hex mesh with 170 thousand elements. Romano *et al.* [57] modeled a pre-notched, printed tensile test bar with a Quad Hex mesh with 23 thousand elements to model the fatigue life at the stress concentration point. At the same time Romano *et al.* [10] modeled a complex

AM support structure using 900 thousand Lin Tet elements looking at probability of failure due to extremely large defects. Finally, Huynh *et al.* [58] modeled AM micro trusses under tension fatigue testing using a Quad Tet with 10.5 million elements (14 million nodes).

Each element type has different strengths and deficiencies and must be studied to determine the best for any given application. The research here will perform a convergence study to identify the best mesh type and number of elements to appropriately capture the geometry of interest.

2.2.4 Digital Replica Development

There is an underlying assumption that using nominal material properties is sufficient for AM production processes and that printed parts will be identical to the applied Computer Aided Design (CAD) model. However, the AM process imposes challenges for predicting how the final component will perform due to process parameter controls, feedstock variability, and inherent material deviations.

Before building a digital replica and predicting how a specific AM component will respond, an understanding of the challenges to build a digital replica are required. There is significant variation in the material properties in AM influenced by the applied print parameters [59, 60]. By incorporating those relationships into a topology problem, the print processing parameters have been shown to change the optimal solution [61]. In addition to controlling the material properties, the AM processing parameters and post-print processing steps create changes from the geometry described by the CAD model.

2.3 AM Defects

Defects being studied in this research are naturally generated through the Additive Manufacturing (AM) process. The AM process has the potential to generate a number of different defect types that can impact the performance of the final part. Section 2.3.1 reviews the types of defects that the AM process can produce with various steps that can be applied to mitigate the impacts. Section 2.3.2 discusses how to detect these defects without destroying the component and the type of data that can be pulled from the detection process.

2.3.1 Natural Defects

Among the potential defects produced by the AM process are pores, Lack of Fusion (LOF), balling, residual stresses [2], and surface roughness [3]. Figure 4 depicts five of the various defect types. Figure 5 depicts how the surface roughness can change based on the print orientation of the print.

Pores fall into two categories, trapped gas particles, and key hole pores. Gas pores are typically spherical in nature and form when air particles that are bound to the powder are released when melted [62] (Fig. 4a). The trapped gas particles form pockets inside the melt pool and are unable to escape due to rapid solidification of the structure. Gas porosity is generally the smallest of the voids and is randomly distributed throughout the part. It is mitigated through control of the powder before fusion [62]. Key hole pores are generally formed during high energy density exposures which causes the print material to boil, creating a cavity under the layer (Fig. 4b) [2]. These defects tend to form along the laser path, creating a chain of defects [63]. The LOF defects occur when the energy applied is not sufficient to fully melt the metal particles in the path. Variations in powder bed thickness and laser parameters contribute to the formation of this defect (Fig. 4c) [15]. LOF defects are generally the

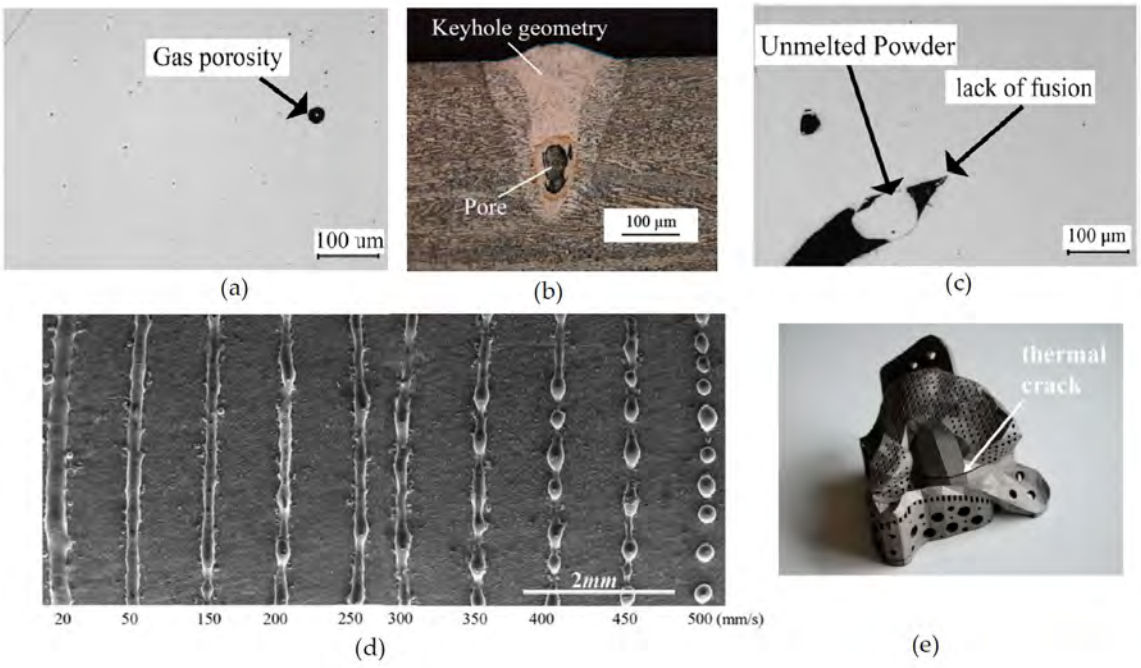

Figure 4. LPBF defect: (a) gas porosity, (b) key hole defect, (c) Lack of Fusion (LOF), (d) balling, (e) crack due to residual stresses [2].

largest of the void defects, creating large flat voids between build layers. The balling defect occurs when the melt pool becomes elongated. To reduce the surface tension of the melt pool, it breaks apart in to spherical balls that cool independently, creating a beaded melt track (Fig. 4d) [64]. The residual stresses in a build are formed during the localized heating and cooling cycles. The material expands when the laser creates the melt pool. As it cools, the material contracts, pulling on the already solidified material close by [16]. Sufficient residual stress causes the material to separate in extreme cases (Fig. 4e) or creates geometry deformation in lesser cases. Either way, the tensile residual stresses are detrimental to fatigue life.

Surface roughness is formed by sintering of free particles at the edge of the melt pool. Overhanging surfaces tend to generate increased roughness because the laser path passes over a bed of loose powder. Figure 5 depicts the surface of a downward face (left) and an upward face (right). The downward face gets more partially melted particles stuck to the part which contribute to surface defects.

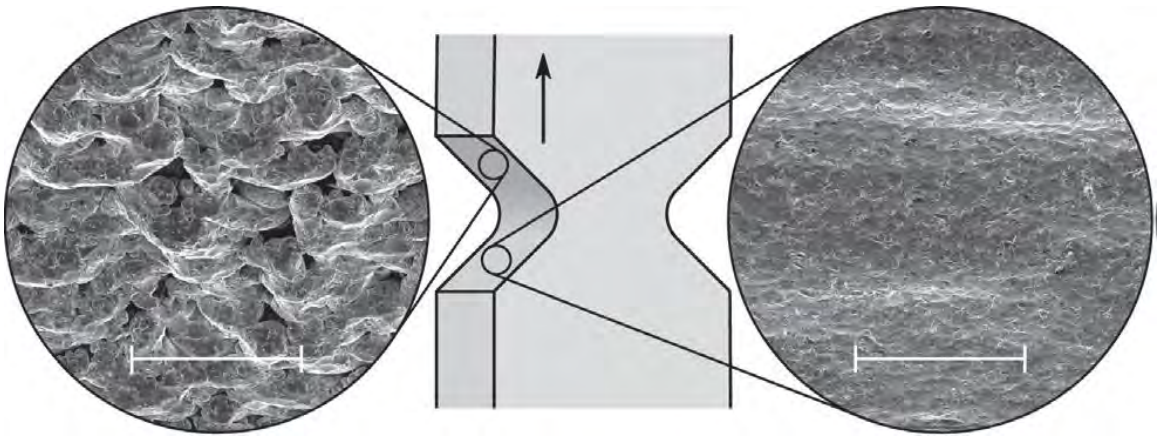

Figure 5. Specimen with a notch indention, the down facing edge (left) shows an increase in surface roughness over the up facing edge (right) [3].

Printer setting such as laser power, scan rate, spot size, and layer thickness all impact the quality of any print job [15,65,66]. Due to the layered build structure and the complex thermal environment of the AM process, structural designs such as print orientation and the amount of material associated with a print layer also impact the material properties [3, 41, 67]. Finally post processing steps such as heat treatments change the material properties [16, 18].

With the use of proper printing parameters and appropriate post-processing, many of these defects can be mitigated. Balling, keyhole defects, and LOF are controlled by the print settings. Over heating leads to conditions that form keyhole defects and/or balling of the melt pool, while under heating contributes to LOF defects. However, the problem is complicated by more than just energy into the system. Sheridan demonstrated that there is a range of Volume Energy Densities (VEDs) that produce a high-density part based on changes in the power input and layer thickness in Fig. 6 [4].

Residual stresses are mitigated by a stress relief heat treatment and machining processes such as grinding to remove stressed layers [16]. Machining processes are also a good method for cleaning up surface roughness by removing the partially fused

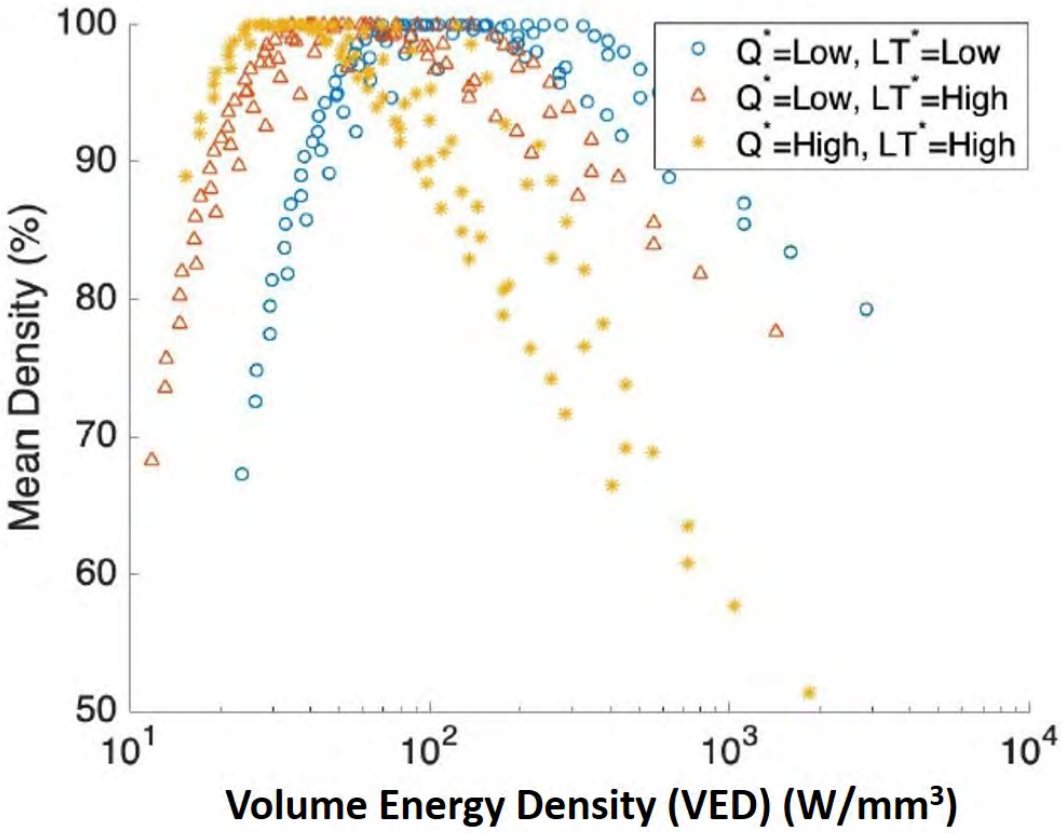

Figure 6. Plot of mean density vs Volume Energy Density (VED). Different processing parameters of power (Q) and layer thickness (LT) shift the optimal VED [4].

particles from the surface.

This research is interested in how the voids generated during the build process impact the fatigue life. The primary focus will be on porous defects that occur during standard build parameters such as trapped gas pockets and LOF. Optimal print parameters will be used to minimize the probability of key holing or balling in this research, and residual stresses and surface roughness will be managed through post process treatments.

2.3.2 Defect Mapping

Knowing that the defects exist requires some method of characterizing the size and location of these voids. The defect distributions that have been generated are region agnostic and almost invariably utilize Computed Tomography (CT) scans [8, 10, 15, 50, 57, 68–70]. The process shoots X-rays through the component at different angles and measures the changes in density though the structure. Due to the complex nature of AM, a defect map is only applicable for a single geometry with the exact processing parameters on one machine. Gumpinger noted differences in critical defect sizes and surface roughness between components printed with a contour pattern and those without [70].

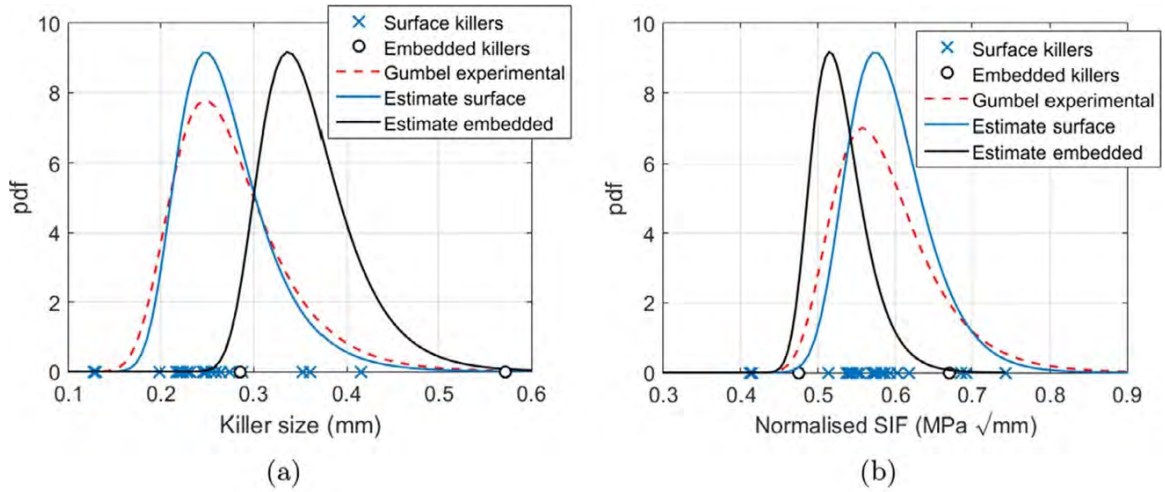

Figure 7. a) Experimentally captured killer defects with estimated extreme value distributions for the surface and interior. b) Defect size converted to SIF [5]

Romano *et al.* demonstrated extreme value distribution differences between defects near the surface and defects in the core using printed AlSi10Mg. Figure 7a showed different defect distributions between the surface and interior. The term "Killer size" refered to the initial defect that propagated to failure. While the largest defects were more likely to occur on interior locations for the tensile bars measured, a surface defect was nearly always the cause of failure. Figure 7b translated the defect

sizes to Stress Intensity Factor (SIF) showing that the higher SIF on the surface of the tensile bars made surface defects the most likely source of failure [5].

The CT scan data describes the range of defect sizes present in a component and where each defect is located. By separating defects by the print setting that generated them, different defect distributions can be created. A defect density distribution allows for statistical modeling of defect sizes that could exist based on the structure, processing parameters, and machine used.

2.4 Fatigue Life

The material fatigue properties of the part drive the output from the chosen fatigue life defect model. An understanding of fatigue life and how the AM process impacts traditional fatigue life models is vital to developing an improved fatigue life prediction. Section 2.4.1 covers the basics of material fatigue life. Section 2.4.2 discusses how the defects introduced by the AM process can impact the fatigue life. Section 2.4.3 touches on how AM processing choices can affect the material properties.

2.4.1 Fatigue Life Concepts

There are three primary factors to determining the fatigue life of a component: the size of the defect being analyzed, the applied stress to the component, and a shape factor which includes the geometry and depth of the defect being analyzed. The simplest fatigue life model is the Basquin Equation (Eq. 1) which assumes the initial defect size and shape are small enough to not contribute to the fatigue life, leaving a fatigue life equation that is only dependent on the maximum applied stress. This creates the traditional S-N curve (Fig. 8) which is purely material dependent with no input from the structure being used. The S-N curve denotes the number of cycles a given material should survive before failure. The Basquin Equation is a fit

to experimental data to predict the maximum stress for a desired number of cycles within the finite life range of the material. In Equation 1, A and b are crack growth material constants [71]. N is the desired life (Fig. 8, X-axis), and $\sigma_{max,N}$ is the maximum stress (Fig. 8, Y-axis). The Basquin Equation only fits the region of Fig. 8 labeled "Finite Life" between the yield stress (S_{max}) and the fatigue limit (S_f) and does not capture the roll over to yield stress at the top or the roll over to the fatigue limit at the bottom.

$$\sigma_{max,N} = AN^b \tag{1}$$

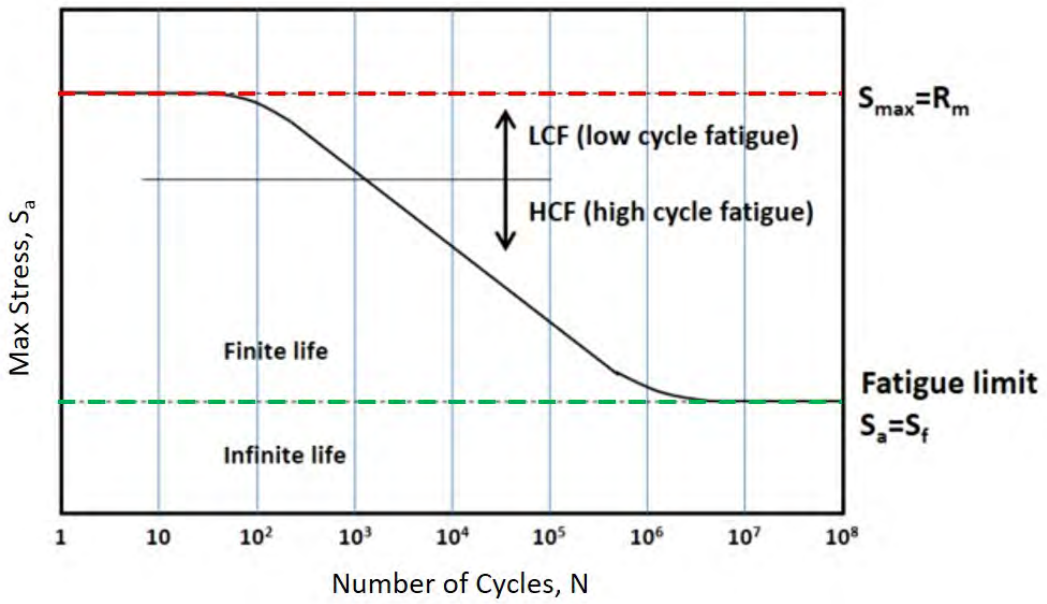

Figure 8. Generic S-N Curve [6].

Equation 1 gives the stress value in terms of maximum stress. To convert to a stress range, Equation 2 is applied, creating Equation 3. The conversion between maximum stress and the applied stress range ($\Delta\sigma_N$) is based on the applied stress ratio (R).

$$\Delta\sigma_N = (1 - R)\sigma_{max,N} \tag{2}$$

$$\Delta\sigma_{0,N} = A(1 - R)N^b \tag{3}$$

The stress ratio introduces a load type dependence on the fatigue properties and is described by Equation 4. σ_{min} and σ_{max} define the lowest and highest experienced stresses over one load cycle. In a fully reversed loading scenario, such as vibrational loading, $\sigma_{min} = -\sigma_{max}$, and $R = -1$. In tension-tension load cases, R will be a positive number between 0 and 1 [7].

$$R = \frac{\sigma_{min}}{\sigma_{max}} \tag{4}$$

For infinite fatigue life modeling, the fatigue limit (σ_0) and fatigue limit range ($\Delta\sigma_0$) are the important values from the S-N curve. For finite fatigue life modeling, the above equations (Eq. 1-4) are used to calculate the critical stress range ($\Delta\sigma_N$) based on the desired component life.

Another important fatigue life model is the Paris Law (Eq. 5). This model incorporates an initial defect size, stress, and shape factor into the Stress Intensity Factor (SIF) (Eq. 6) to predict the crack growth rate. The model assumes that Linear Elastic Fracture Mechanics (LEFM) is the dominant cause of failure and that the crack growth rate is log-linear to the SIF.

$$\frac{da}{dN} = C\Delta K^n \tag{5}$$

Figure 9 denotes a typical crack growth chart for metals. Region I is crack initiation, region II is crack growth, and region III is the final rupture.

The crack growth in region II is generally modeled by the Paris Law, where C and

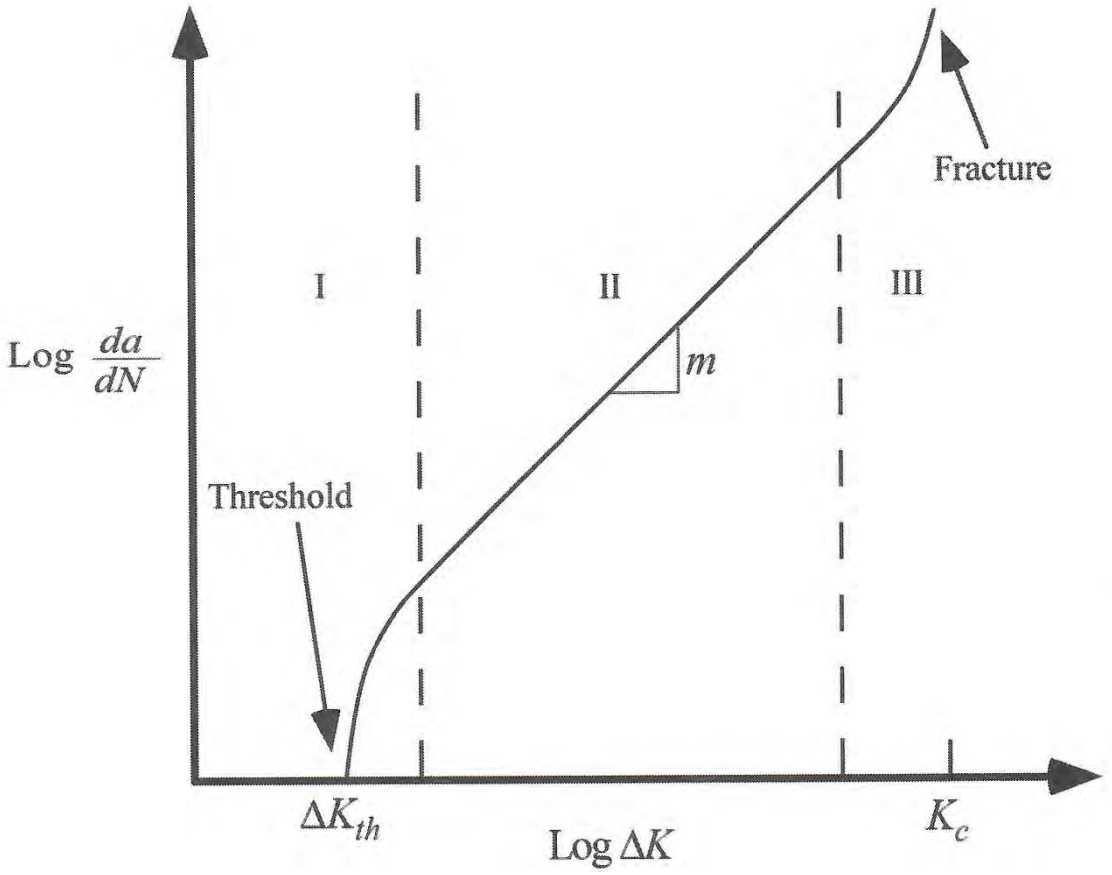

Figure 9. Typical crack growth behavior for metals [7].

n are material constants determined by sample testing. The Paris Law is a simplified fit of the slope relating the Stress Intensity Factor (SIF) to the change in crack length per change in number of cycles.

ΔK is the SIF, and describes the relationship between the applied load, defect size, and defect location as shown in Eq. 6 [7]. Y is the shape factor of the defect and is governed by shape and location of the defect in question. $\Delta\sigma$ is the stress experienced by the defect perpendicular to the crack growth direction and is governed by the load case and part geometry. a is the initial defect size.

$$\Delta K = Y \Delta\sigma \sqrt{\pi a} \tag{6}$$

The crack growth chart for a given material (Fig. 9) allows the extraction of the threshold SIF (ΔK_{TH}) and the fracture SIF (ΔK_{1C}). ΔK_{TH} is the SIF value below which cracks do not propagate and is used for infinite life modeling. ΔK_{1C} is the SIF where final rupture occurs.

The shape factor (Y) associated with each defect has a location dependence based on the defect's ability to interact with the surface of the part. Murakami demonstrated that for internal porous defects, a shape factor of 0.5 was appropriate, and for porous defects near the surface, a shape factor of 0.65 was appropriate [72]. Equation 7 defines the boundary for when a defect can be considered a surface flaw versus an internal flaw [5]. When the ratio of radius of the defect, r, divided by the distance from the defect center to surface, h, is greater than 0.8, then the defect in question may be treated as a surface flaw [73].

$$r/h \geq 0.8 \tag{7}$$

2.4.2 AM Variations

The AM process introduces several new variables in generating a standard S-N curve. Due to the stochastic nature of the defect formations with respect to size and location within an AM production, AM Stress to Life (S-N) curves have significant variation with defect sizes being one of the contributing factors [38, 70, 74, 75]. Additional variables are print orientation and post-processing steps.

Beretta *et al.* studied the effects of print orientation on AlSi10Mg using a three-point bending fatigue specimen using 86 specimens printed across the five different orientations [8]. Figure 10 depicts the print orientation for each test series. The data from each orientation generated a different S-N curve. The variations in the S-N curves, where the only manufacturing difference was the orientation of build, were

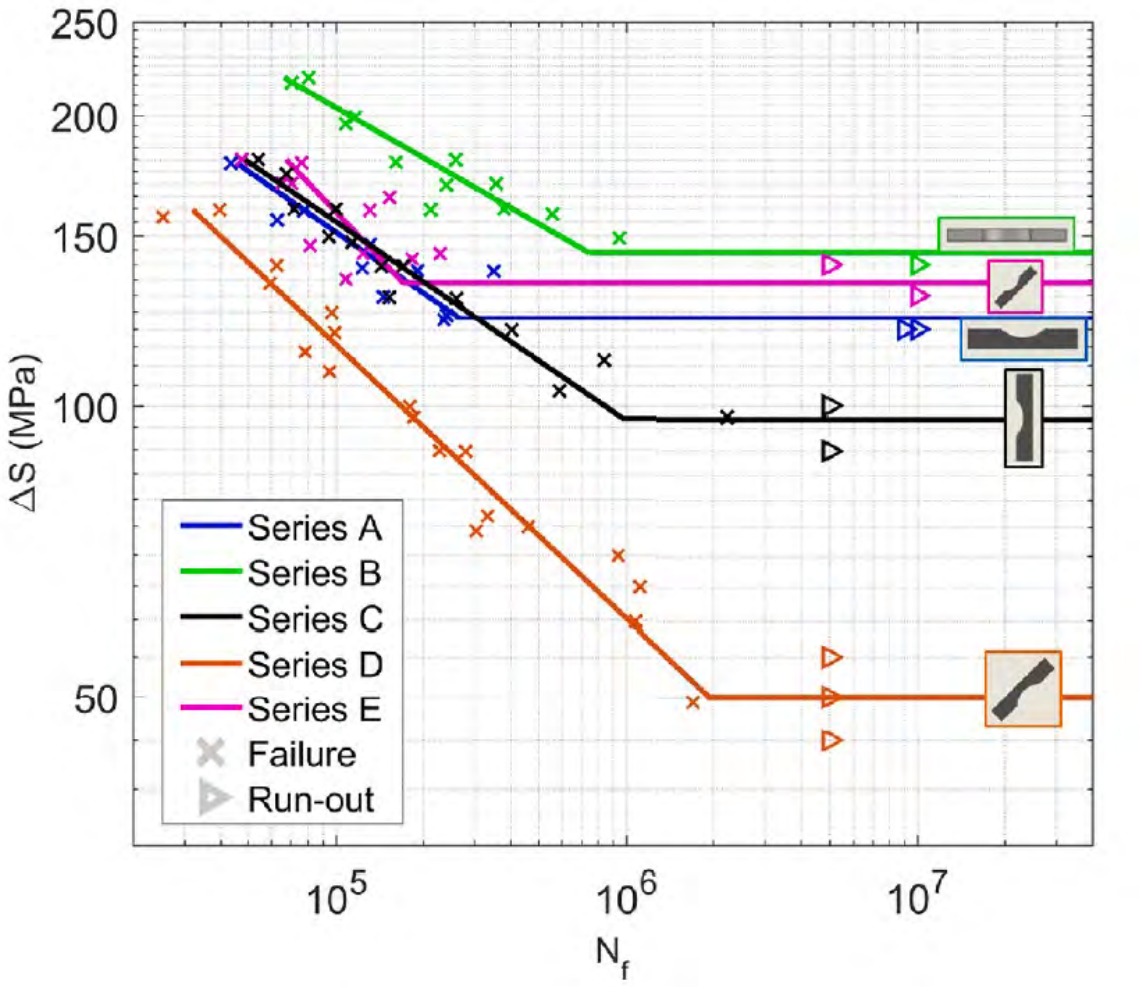

Figure 10. Variations of the S-N Curve for AlSi10Mg due to variations in the print orientation. Parts were tested "as-built" with no surface cleaning or heat treatment [8].

primarily attributed to surface roughness, with a secondary impact from residual stresses in the "as-built" components. The spread of S-N curves from 140 MPa delta stress fatigue limit down to 50 MPa delta stress fatigue limit correlates to the surface roughness along the sample curve radius. The samples with overhangs (series C & D) printed rougher surfaces due to the orientation which translated to large surface flaws that form into crack initiation sites, and have correspondingly lower fatigue limit values. A similar test campaign with axial fatigue test specimens using printed aluminum also generated different S-N curves for different print orientations. For this

case, the variation in fatigue life predictions was tied to the fatal defect sizes, where one orientation formed larger defects than the other [38].

Sheridan studied the effects of defect size on heat treated, machined IN718 tension fatigue specimens, and demonstrated a trend that as the maximum defect size decreased, the S-N curves for IN718 approach the fatigue performance for wrought IN718 as shown in Figure 11 [4]. By machining the fatigue bar surfaces, AM surface roughness was removed as a factor, and internal defects dominated failure. This trend allows for the use of wrought material properties for defect free predictions.

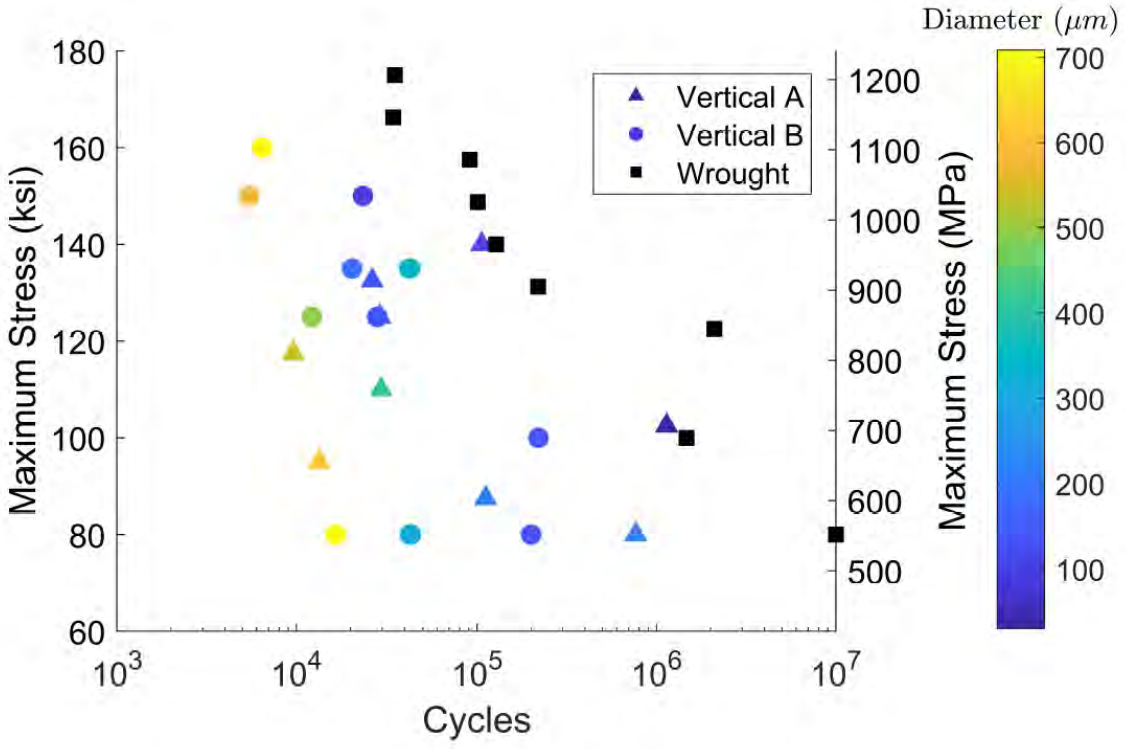

Figure 11. Fatigue stress vs number of cycles for IN718 samples. Data point coloration corresponds to the maximum defect size in the part [4].

Taylor *et al.* studied the effects of microstructure on short cracks, and found that grain size tends to impact crack growth behavior to approximately three times the grain size. Beyond that point, long crack growth dominates and the Paris Law fits the data well [76].

Experimental work using nickel-based superalloy 718 demonstrated that AM fatigue life failures were not always controlled by LEFM. Identical specimens from one build plate failed due to defects less than 50 μm and performed near the Basquin Equation or failed due to defects greater than 100 μm and were dominated by the Paris Law [77]. The test data suggested that both models must be considered when studying fatigue life. For AM components where defects are widely prevalent and failure defect size can vary greatly, a blending is needed to improve fatigue life predictions.

2.4.3 Material Properties

The fatigue resistance properties of AM materials have been studied extensively. The properties of an AM material vary based on the processing parameters used, part geometry, orientation, and post-processing steps [4, 8, 68–70, 78]. Sheridan's research indicates that wrought material properties for IN718 are a good estimate for a defect free AM IN718 [4]. The study of how the material properties vary is outside the scope of this research. Here the samples being tested will be stress relieved, polished, and age hardened using standard processes for IN718. The crack growth material properties used by Sheridan [11] for IN718 as shown in Table 1 will be utilized as the starting point until material testing provides data specific to the AM build.

A	b	γ	C	C_0	n	m
4623.4	-0.1558	0.3727	1×10^{-13}	1.25×10^{-14}	4	0.75

Table 1. Model constants for the Basquin Equation (Eq. 1) and Paris Law (Eq. 5) assuming defect free wrought material properties based off fit data by Sheridan [11].

2.5 Fatigue Life Modeling of AM Materials

Numerous research efforts have looked at how AM performs in uni-axial fatigue testing in the presence of defects [3, 4, 8, 18]. Initial fatigue life models focused on the

infinite life boundary [21, 22]. In recent years work has begun to focus on defining the fatigue life for finite life problems with respect to AM defects [11]. Section 2.5.1 reviews the development of the Kitagawa and Takahashi diagram as well as the El-Haddad model. Section 2.5.2 discusses how defects from the AM process are applied to the models. Section 2.5.3 highlights recent research with infinite fatigue life modeling, and section 2.5.4 extends the research to include finite fatigue life modeling.

2.5.1 Fatigue Life Model Development With Defects

Infinite life modeling of components begins with Kitagawa and Takahashi who developed the KT model for infinite life as a piece wise function as seen in Figure 12. Line 1 is a horizontal line that represents the fatigue limit stress of the material. Line 2 defines a constant SIF curve per Equation 8. ΔK_{TH} replaces ΔK in Equation 6, and is then rearranged to solve for the stress range, $\Delta\sigma$. The SIF threshold (ΔK_{TH}) from the material crack growth charts defines the boundary where any SIF larger will grow cracks.

$$\Delta\sigma = \frac{\Delta K_{TH}}{Y\sqrt{\pi a}} \tag{8}$$

Any defect predicted to be in the bottom left quadrant is modeled to have infinite life due to a lack of crack growth potential. Stress ranges above $\Delta\sigma_0$ are predicted to fail based on material fatigue properties. Defects to the right of the SIF Equation fall in the constant crack growth region governed by the Paris Law from Equation 5 [21].

El-Haddad modified the KT model to put both piece functions into a single equation that includes a transition region where virgin material properties and defect growth properties are blended together. The El-Haddad model used Eq. 9 to define an infinite life boundary based on defect size and the maximum applied stress to determine if a component is susceptible to failure [9, 22] as seen in Figure 12 line 3.

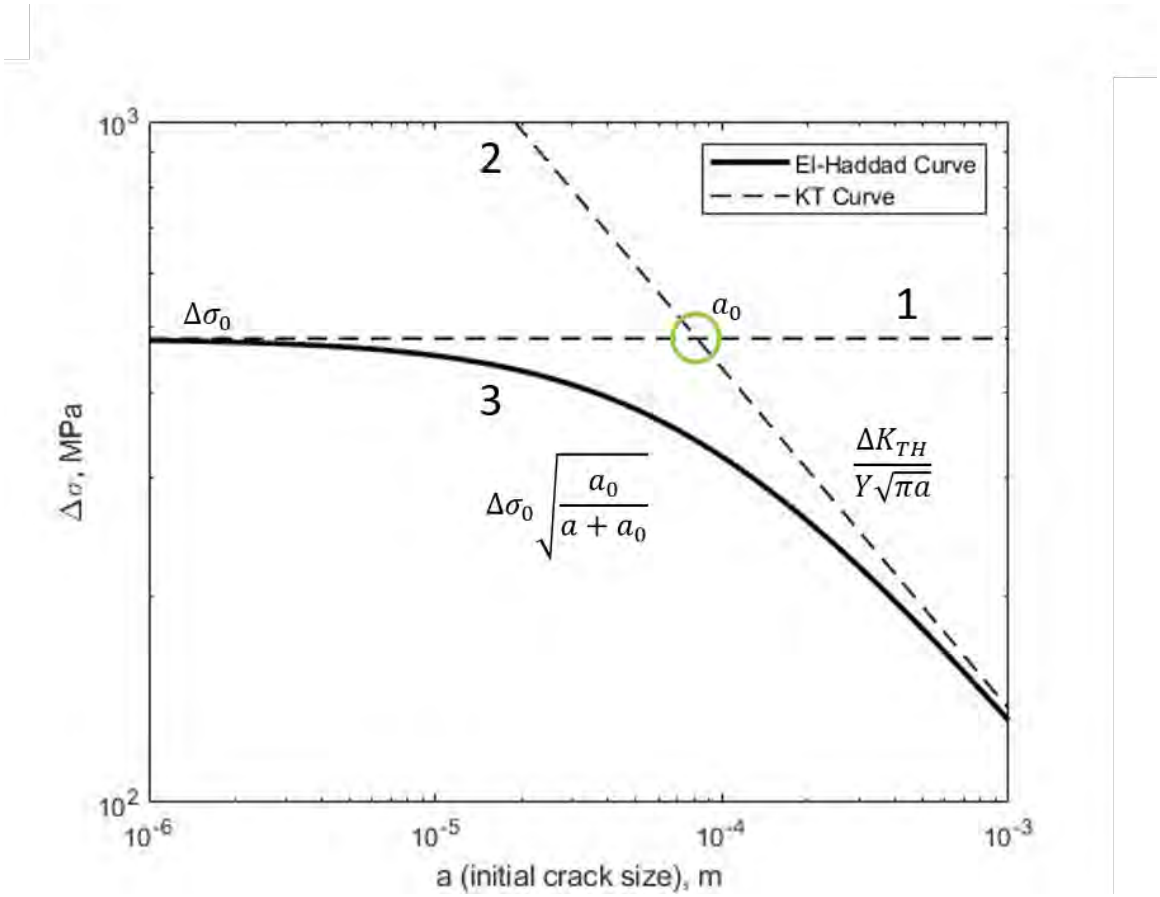

Figure 12. KT model and El-Haddad model for infinite fatigue life. Curve 1) The material fatigue limit. Curve 2) the LEFM crack growth rate. Curve 3) The El-Haddad curve to asymtotically approach curves 1 & 2 Plotted curves use printed IN718 material properties.

$$\Delta\sigma = \Delta\sigma_0\sqrt{\frac{a_0}{a+a_0}} \tag{9}$$

In Equation 9, $\Delta\sigma_0$ is the defect-free stress range that corresponds to the stress fatigue limit; a_0 is the critical crack length and a is length of the crack of interest.

The critical crack length is calculated by solving for the intersection of the two KT lines. Rearranging Eq. 8 for a, and putting $\Delta\sigma_0$ in place for $\Delta\sigma$ yields Equation 10 where a turns into a_0. This is the defining point where LEFM becomes the dominate crack growth process for the fatigue life. In the KT model, a_0 is a hard transition point. In the El-Haddad model, both failure methods are important in the region

around the critical crack length. When the defect being analyzed is significantly smaller than the critical crack size, the material stress fatigue limit dictates if a defect will grow into a crack and cause failure. As the initial defect size increases, the model becomes dominated by LEFM to determine the defect sizes that could grow to failure.

$$a_0 = (\frac{\Delta K_{TH}}{Y \Delta \sigma_0})^2 \frac{1}{\pi} \tag{10}$$

Aigner *et al.* performed a side-by-side comparison of the KT model with the El-Haddad model for Single Edge Notched Bending (SENB) samples of cast aluminum as seen in Figure 13. The triangular data points represented samples that never failed, and the circles, diamonds, and x's represent the samples that failed. Within the transition region around the critical crack length, the El-Haddad model was more accurate than the KT model at predicting if the sample would fail [9]. Any point below the respective curves should have hit runout. The majority of the failure samples fell below the KT (not predicted to fail) and above the El-Haddad curve (predicted to fail).

Both the KT model and El-Haddad model were built to account for any type of defect using the material crack growth properties and have a dependence on the load ratio (R) that is applied. The models define the boundary between the infinite and finite fatigue life based on the cyclic stress range and the crack size found on a part [21]. The El-Haddad model has been demonstrated to be a reasonable estimation for the boundary between fatigue limit behavior and finite life through extensive uniaxial tension testing [5, 9, 23].

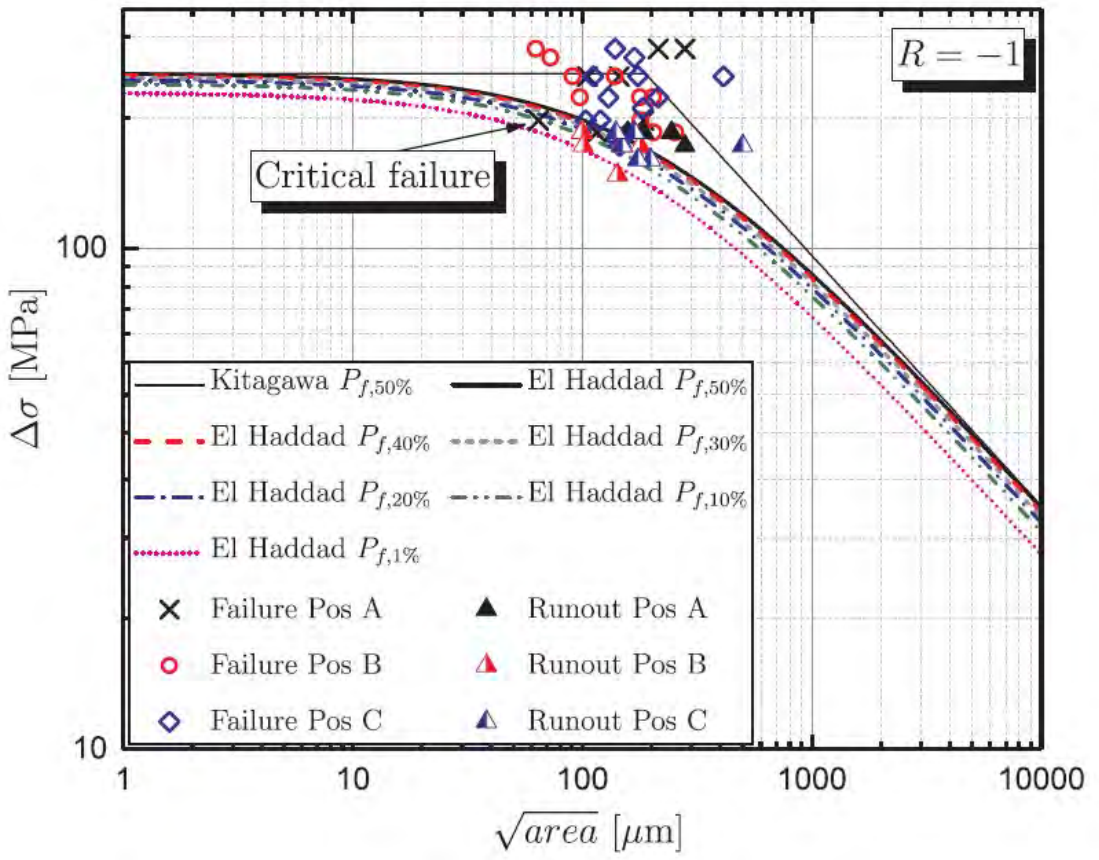

Figure 13. Comparison of KT and El-Haddad models for cast aluminum samples [9].

2.5.2 Modeling of AM Defects

To study the effects of AM defects on fatigue life Beretta *et al.* modified the El-Haddad Equation (Eq. 9) based on the work by Murakami which estimated crack length for an arbitrary crack shape as the square root of the defect area as projected onto the plane normal to the principal stress [72]. The modified El-Haddad Equation replaces a_0 & a with $\sqrt{area_0}$ & $\sqrt{area}$ to form Equation 11 [79].

$$\Delta\sigma = \Delta\sigma_0 \sqrt{\frac{\sqrt{area_0}}{\sqrt{area} + \sqrt{area_0}}} \tag{11}$$

When applied to AM defects, the $\sqrt{area}$ terms in Equation 11 is used to convert the cross-sectional area of an AM defect into a length term which can be applied to

Equations 9 & 10 exactly like any other defect. This adaptation to the El-Haddad Equation is used widely when studying AM defects with respect to fatigue life to simplify defect size estimation for LOF defects that can be have highly irregular geometries [9–11].

2.5.3 Infinite Fatigue Life Research

Romano *et al.* [10, 57] have been studying the probability of failure based on extreme value defect size distributions and the probability that a large enough defect will be created at the stress concentration point, causing eventual fracture. These models created binary fatigue failure predictions based solely on material properties with the assumption that component failure occurred at the point of maximum stress. Figure 14 is the process map used by Romano *et al.* outlining the steps needed when applying PRObabilistic Fatigue Assessment of Components with dEfects (ProFACE) to estimate the probability of failure. This approach used the extreme value defect distribution, FEM, and material properties as the inputs to the fatigue life model to predict the critical defect size and probability of failure at the stress concentration point.

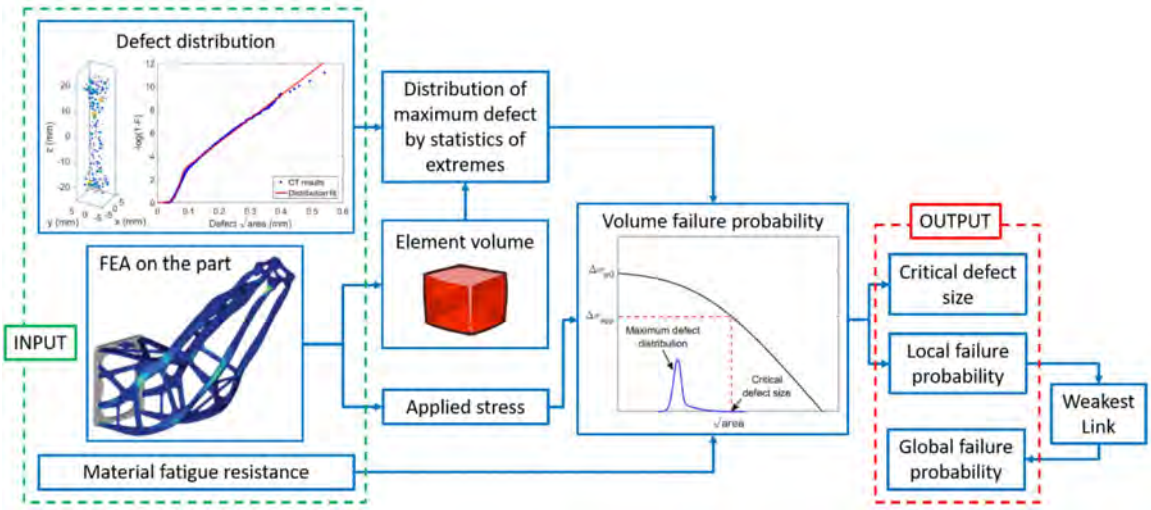

Figure 14. ProFACE modeling of critical defects [10].

2.5.4 Finite Fatigue Life Model Development

Recent developments to the El-Haddad fatigue life model led to a finite fatigue life version by applying Linear Elastic Fracture Mechanics (LEFM). The model updates enabled the predictions of the finite life boundaries by applying the functional applied stress as defined by the Basquin Equation (Eq. 1) in place of the fatigue limit ($\Delta\sigma_0$) and modifying how the critical crack length (a_0) is calculated [11]. Using the Basquin Equation (Eq. 1) from the S-N curve, $\Delta\sigma_N$ can be calculated for a defined finite life. Equation 12, which predicts an initial crack length that will reach fracture after N cycles, is created by integrating the Paris Law (Eq. 5) and separating the crack length (a) and the number of cycles (N). The critical defect size ($a_{0,N}$), which defines the transition between material limited fatigue behavior and LEFM behavior is a_N from Equation 12 [11].

$$a_N = (a_c^{1-\frac{n}{2}} - N(1-\frac{n}{2})C_0(Y\Delta\sigma_N\sqrt{\pi})^n)^{\frac{1}{1-\frac{n}{2}}} \tag{12}$$

C_0 & n are material properties, and Y is the shape factor for the defect of interest. a_c is the critical crack length when failure occurs, and can be calculated using Equation 13 which takes Equation 10 and replaces ΔK_{TH} with ΔK_{1C} of the material and Y with 1.12, which is the shape factor for a through crack that touches the surface.

$$a_c = (\frac{\Delta K_{1C}}{1.12\Delta\sigma_0})^2\frac{1}{\pi} \tag{13}$$

Figure 15 depicts the finite life models and collected experimental data that Sheridan compiled [11]. The El-Haddad formulation from Equation 11 turns into Equation 14, where the "N" subscript denotes the desired design life.

$$\Delta\sigma_N = \Delta\sigma_{0,N}\sqrt{\frac{\sqrt{area_{0,N}}}{\sqrt{area}+\sqrt{area_{0,N}}}} \tag{14}$$

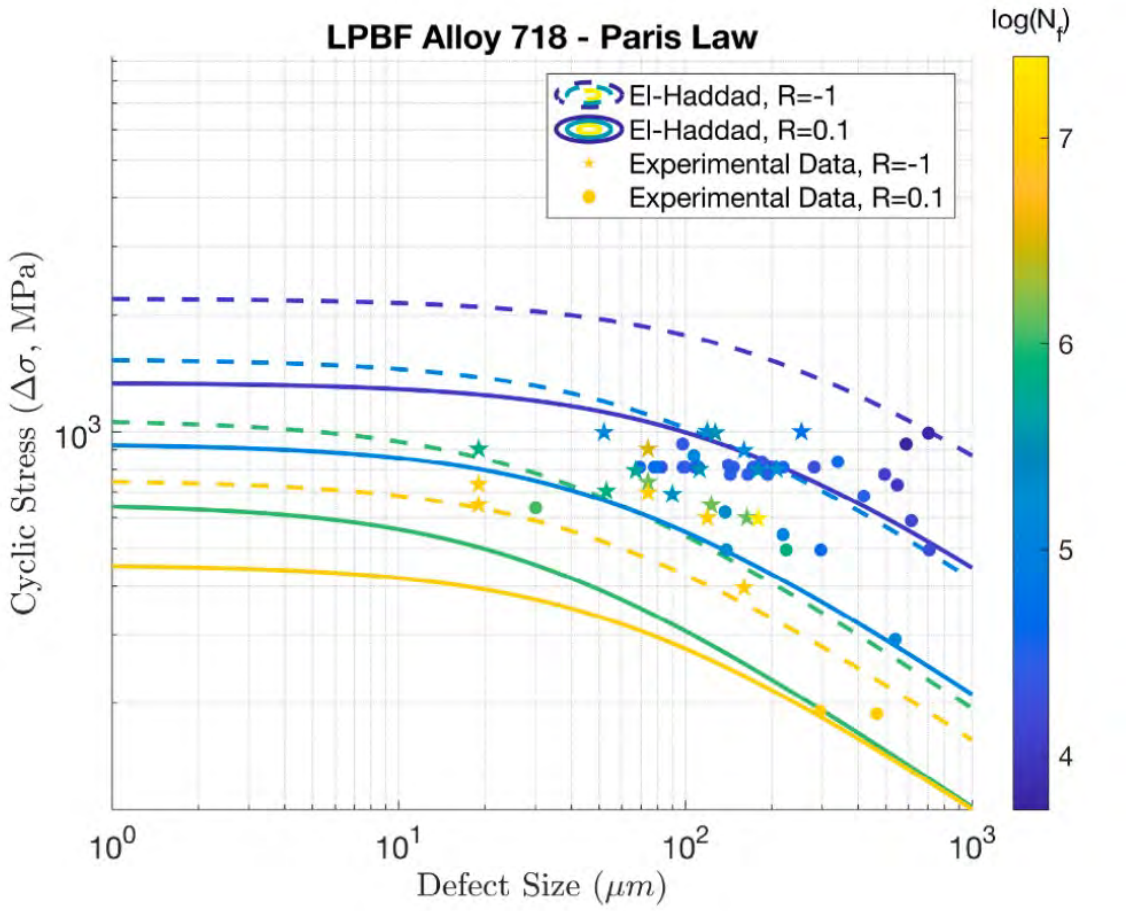

Figure 15. Modified El-Haddad model for finite life. The stress ratio, R, and the design life are the driving factors for determining the allowable defect size for a part [11].

Under the Murakami assumption that $\sqrt{Area}$ is equivalent to defect size, Equation 14 is simplified to Equation 15. The allowable stress range ($\Delta\sigma$) became an explicit function of defect size (a) and the desired design life (N), but there is also an implicit dependency on the designed stress ratio (R) which shows up in Figure 15. The finite model development was built on the foundation of uni-axial tension testing with a uniform stress field.

$$\Delta\sigma = \Delta\sigma_{0,N}\sqrt{\frac{a_{0,N}}{a + a_{0,N}}} \tag{15}$$

2.6 Summary

Chapter II covered FEM development, AM defects and impacts, fatigue life modeling, and the development from infinite life research to finite life research. The work by Romano *et al.* [10] is the nearest literature to the goals of this research. Where Romano applied the defect distribution and FEM to the fatigue life model to predict probability of failure, this research is interested in predicting the critical defect size and location combinations that would result in a particular finite life prediction based on the FEM and finite life fatigue model. Using the material fatigue property equations from section 2.4.1 and the finite fatigue life model discussed in section 2.5.4, this research evaluated and extended the work from a uniform stress field to a variable, multi-axis stress field, highlighting the importance of where a defect is formed in addition to the size of any given defect. Sheridan's finite fatigue life model [11] was combined with Finite Element Analysis (FEA) to incorporate geometric considerations in addition to the material properties. The FEA inclusion built the relationship between defect locations and applied stress, removing the need to assume that failure would always occur at the maximum stress location. Experimental data demonstrated that failures could initiate from locations with stress values as low as 50% of the maximum applied stress. This made component geometry an important consideration in fatigue life predictions. Improved accuracy in the predicted stress distributions also enabled crack initiation predictions [77]. This final version of the fatigue life model relied on the ability to accurately predict the stress values across the geometry for a given load case.

III. FEM Validation

3.1 Overview

This chapter develops an understanding of how changes to the component geometry and applied material properties due to printing and post-treatment steps from the designed model impact the FEM frequency and stress/strain values. The research experimentally measured the geometry deformations and material properties to produce digital replica FEMs of AM turbine blades, reducing the associated error with predicting the applied stress at any given location.

This research utilized a generic turbine blade design developed by Air Force Research Labs to be a structural representative of an airfoil without optimization for aerodynamics (Fig. 16). Prior research with the turbine blade design scaled the blade to optimize vibrational testing when exciting the second bending mode [50]. Using the same blade design and scaling, this work created digital replica models to account for the production variations associated with AM processing. The digital replica models were developed through three phases:

- Convergence study
- Hardware characterization
- Experimental validation

The convergence study informed on the required mesh sizing and element selection to create the initial FEM. Nominal wrought material properties were applied to a simplified blade geometry. Mesh type and density was selected based on the convergence of the natural frequencies and the stress values associated with the first three modes.

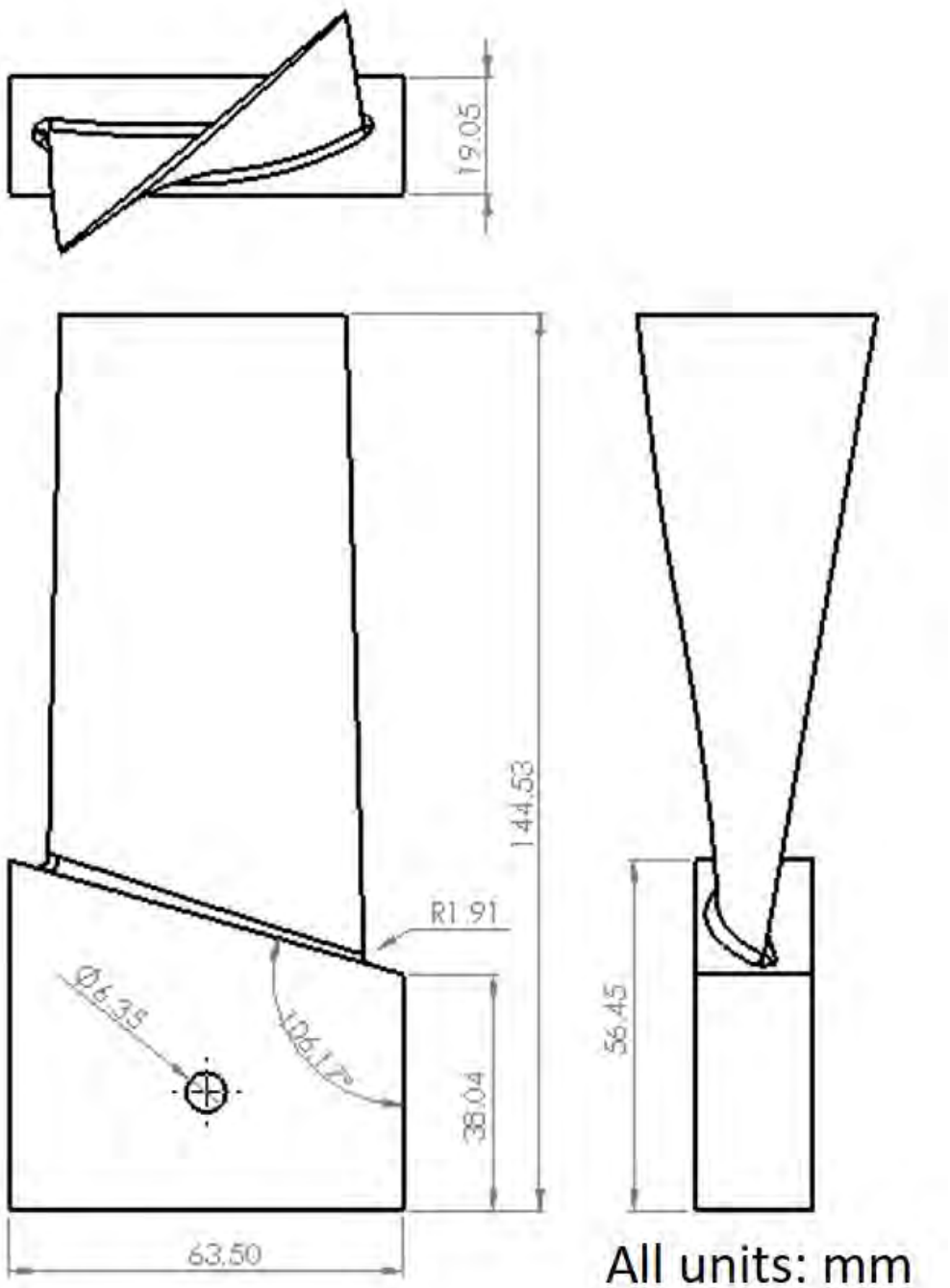

Figure 16. CAD geometry for the generic turbine blade.

The hardware characterization analyzed physical specimens to modify the initial FEM into digital replicas. Round fatigue bar specimens printed on the same build plate as the turbine blades were analyzed to adjust the material properties of density

and Young's Modulus. These parameters controlled the FEM vibrational responses. Structured light scanning of the printed turbine blades generated the variations between the "as-designed" CAD geometry and the final hardware dimensions. The structured light scanning has been applied to individual turbine blades to incorporate geometric damage into the models [80]. The process has also been applied to integrally bladed rotors to fine tune the vibrational response due to minor variations between integrated blades [81]. Application of the measured material properties and final hardware geometries created the unique digital replicas which were each linked to a single hardware component.

The experimental validation compared bench testing of the printed turbine blades against their digital replicas to quantify the model improvements related to the hardware characterization. The validation process studied the final mass and volume of the digital replicas against the hardware to verify the applied density values. Natural frequency assessments quantified the impacts to frequency predictions from both the material properties and the geometric variations. Finally, strain gauge data at select locations informed on the ability of the digital replicas to generate an accurate stress/strain map with respect to each turbine blade's unique geometry.

This work created digital replicas of AM turbine blades and quantified how variations due to AM production impacted FEM development. Developing the understanding of how AM deviations impact FEM predictions is the first step to understanding the critical parameters to monitor for a digital twin. The replicas were experimentally validated through vibrational blade testing. With the objective of applying these digital replicas to improve fatigue life predictive capabilities, matching the model stress maps to the experimental data was the most critical of the validation steps. These validated models can also be applied to size and shape optimizations for satisfying vibration and strength requirements.

3.2 Finite Element Model Development

The first phase developed the "as-designed" FEM based on nominal wrought material properties and the CAD based geometry using quadratic hexahedron elements (C3D20R) within the Abaqus software. A simplified turbine blade geometry formed the base of the FEM development (Fig. 17A). Upon completion of the convergence study to size the meshing based on frequency and stress convergence, the simplified CAD geometry was meshed (Fig. 17B). By morphing the simplified turbine blade FEM (Fig. 17B) against the full CAD model (Fig. 17C), idealized FEM of the turbine blades was built. Mesh refinements were applied to the edges and base of the turbine blade mesh to improve the morphing accuracy along the regions of large curvature changes (Fig. 17D). This final FEM was the baseline model used to develop the turbine blade digital replicas.

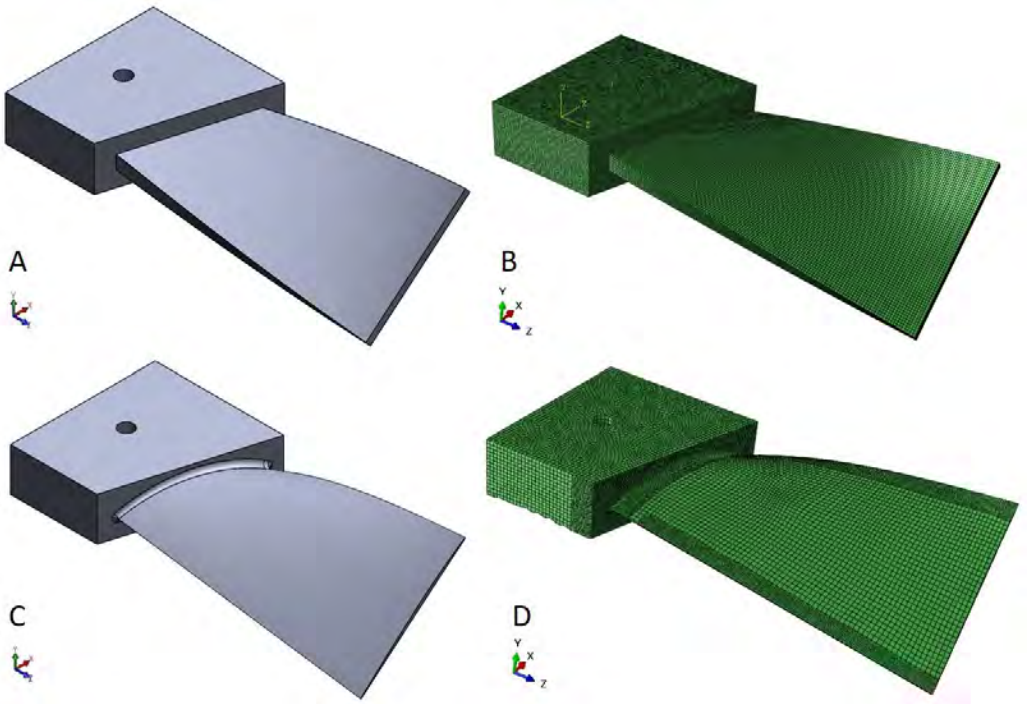

Figure 17. A) simplified turbine blade CAD file. The blade is reduced to a tapering rectangle with a 40 degree twist. B) Hex Mesh of the simplified blade. C) Original turbine blade design. D) Final morphed mesh to match the turbine blade geometry.

3.2.1 Convergence Study

The optimum FEM mesh type and element size was determined through a convergence study. Using Abaqus 6.14, four different solid 3-D element types were studied: a reduced integration Linear Hexahedron (C3D8R), a reduced integration Quadratic Hexahedron (C3D20R), a Linear Tetrahedral (C3D4), and a Quadratic Tetrahedral (C3D10). Every case was subject to a frequency analysis. The convergence was performed on the simplified turbine blade mesh (Fig. 17B) without the grip section. The base of the blade was fully constrained against translation across the surface that would connect to the grip. This simplification assumed that the grip would have no measurable impact on the frequency response of the blade. The grip was designed to be clamped on top and bottom during experimentation, and was significantly thicker than the base of the blade to prevent any strain within that region. The simplified blade geometry also significantly reduced the computation time for the convergence study enabling more cases to be run.

The frequency convergence for each mesh type was analyzed based on the first three vibrational modes. Figure 18 depicts the frequency and bound vibrational stress convergence for each case. The mesh density was converted to a total number of nodes applied in the mesh. A power law curve to predict the FEM response for each element type based on the mesh density was fit to the results. By averaging the limit of each curve fit as it approached infinity, an assumed truth value was generated for the frequency and stress value of each mode. Finally, a 5% error band was placed around these assumed truth values to depict the level of accuracy in the mesh convergence. For the natural frequencies (Fig. 18A-C), the quadratic elements converged very quickly, where only 1,000 nodes were needed to get within 5% of the steady state values. In comparison, the linear elements needed almost 40,000 nodes to converge across the first three modes.

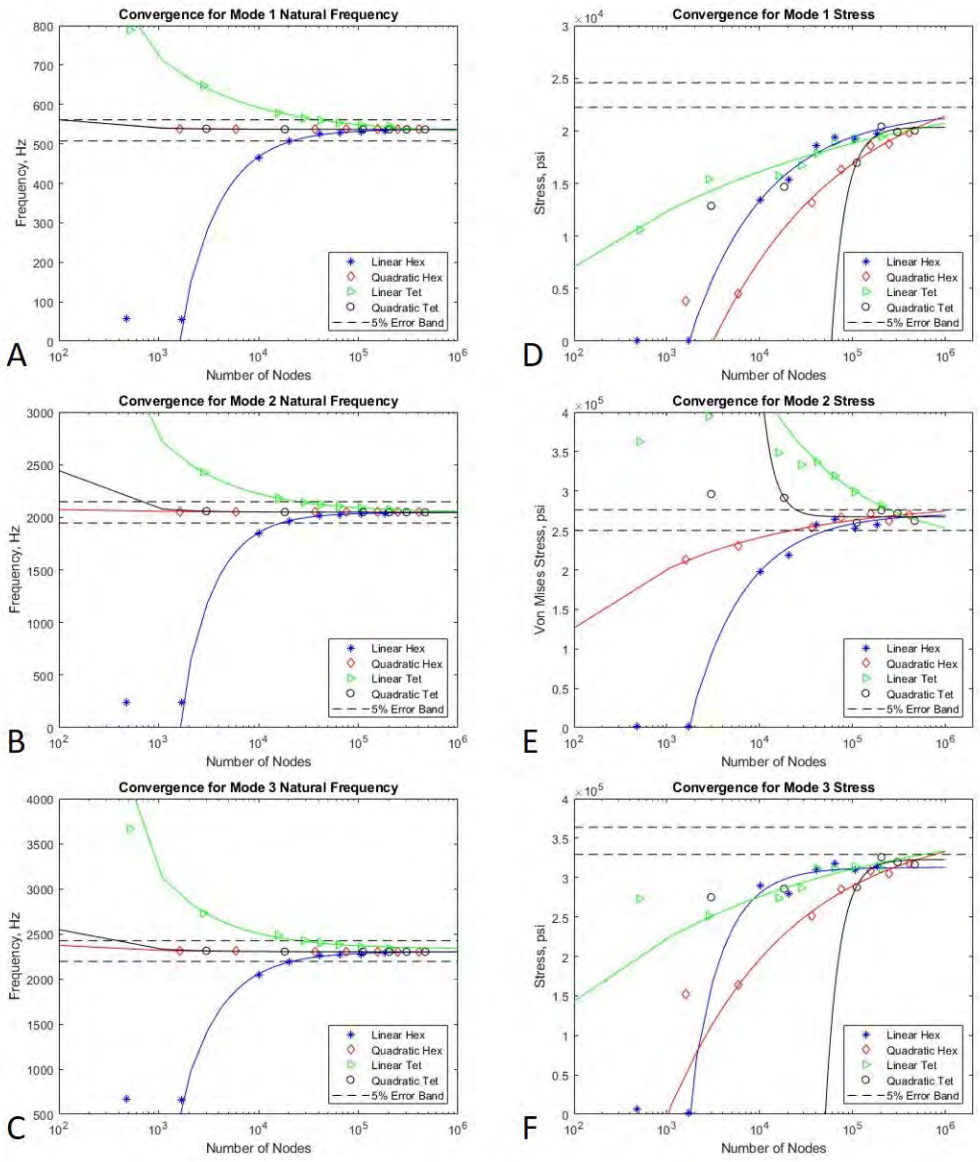

Figure 18. Convergence study of the simplified turbine blade for the first three modes. A-C: frequency convergence. D-F: stress convergence.

In addition to generating a mesh that accurately represented the vibrational response, the mesh also needed to accurately capture the stress response of the turbine blade. Figure 18D-F shows the convergence of the stress at one point along the blade. The maximum stress point was not used here due to the singularity from the simplified blade boundary conditions. Instead, a point approximately two thirds of the blade length from the root of the turbine blade was used. This point was a local maximum

associated with the second bending mode. Due to the selected evaluation point, the calculated stresses for mode 1 (Fig. 18D) and 3 (Fig. 18F) never came within 5% of the projected ideal values. For the mode 2 stress convergence, the quadratic elements needed at least 25,000 nodes to reach the 5% error band. In comparison, the Linear Hexahedron element needed approximately 50,000 nodes, and the Linear Tetrahedral element needed over 200,000 nodes.

The convergence study concluded that above 25,000 nodes, either of the quadratic element types are accurate, and above 200,000 nodes the element selection became user preference. The final considerations for element selection came down to ease of application. Within Abaqus, the hexaherdon elements were easier to apply across the whole geometry (blade and grip) and the quadratic elements offered more flexibility for the morphing software to match the CAD surface.

The final applied mesh was the Quadratic Hexahedron element type (C3D20R) with an average element size of 2.2×10^9 μm^3 (approximately 1.3 mm per side). The mesh was applied to simplified CAD geometry to create a baseline turbine blade FEM (Fig. 17B). Figure 17B was morphed using FEMorph against the target surface of the CAD model (Fig. 17C) to align the FEM with the "as-designed" geometry. The morphed FEM was further refined along the base of the blade, trailing edge, and leading edge to an average size of 6.2×10^7 μm^3 (approximately 0.4 mm per side). The mesh refinements improved the geometric fit with respect to the fine features in those regions. The final mesh (Fig. 17D) had 944,021 total nodes across the blade and grip sections. Of those nodes, 210,652 were contained in the blade. With this element type and node count, the frequencies have converged and the stress for mode 2 was within 2% of the predictive convergence value. This mesh was the "as-designed" FEM or CAD based FEM which created a predictive baseline. While the grip was not critical for the convergence study, it was vital for the model verification. The grip

defined a common origin for hardware characterization and validation steps.

3.2.2 Frequency Analysis

A modal frequency analysis was performed on the CAD based FEM to predict the first five natural frequencies and to estimate the modal stresses associated with the mode shape displacements as shown in Fig. 19. The applied material properties to the initial FEM used the wrought material properties of Inconnel alloy 718. As seen in Figure 11, when the print quality of AM components improves, the material properties approach wrought properties [75]. By starting with the nominal wrought material properties, assessments were made on the importance of accurate material properties for AM builds. The nominal material properties applied to this research were density of 8.22 g/cm^3, Young's Modulus of 199.9 GPa, and Poisson's Ratio of 0.294 [82].

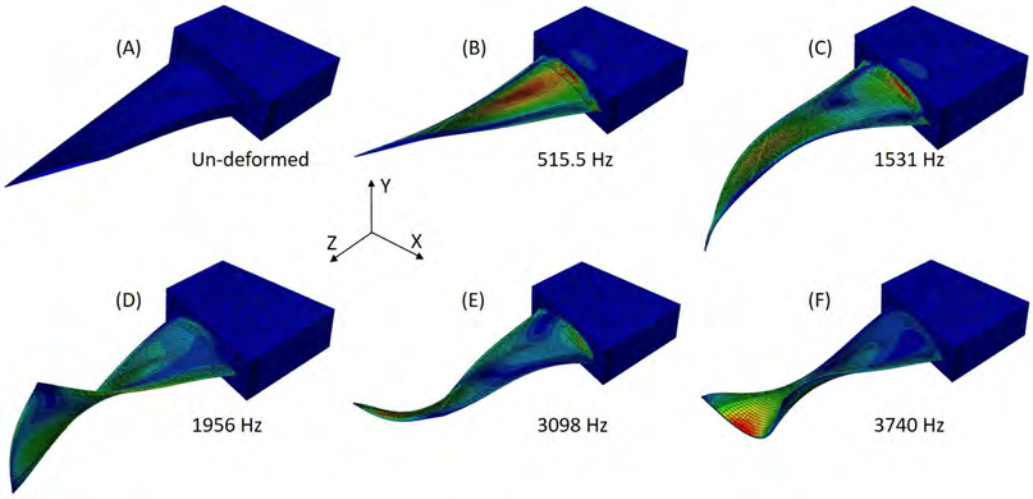

Figure 19. A) Base Mesh: no deformation. B) Mode 1: first bending. C) Mode 2: second bending. D) Mode 3: first torsion. E) Mode 4: third bending. F) Mode 5: second torsion.

Modes 1, 2, & 4 (Fig. 19B, C, & E) were the first three bending modes where the blade flexes along the ± Y-axis. Modes 3 & 5 (Fig. 19D & F) were the first and second torsion modes rotating the blade around the Z-axis.

3.3 Hardware Characterization

The "as-designed" FEM from phase one assumed the hardware was perfect to the design. However, the AM process introduced uncertainties in the material properties and created deviations from the baseline model geometry. The AM process had variations in the added material due to powder distributions and variations in the laser controls. There were additional variations in the component geometries during post processing while improving the surface finishes. To effectively utilize the FEM, the model needed to be adjusted based on the built components. Phase two controlled the input variables of material properties for printed IN718 (density, Young's Modulus, and the Poisson Ratio) and variations in the final geometry of each printed blade from the original design.

A total of eighteen cylinders and ten turbine blades were Additively Manufactured from nickel-based superalloy 718 on an M2 Cusing Laser Powder Bed Fusion (LPBF) printer. All specimens were annealed at 1000°C for one hour and then left to oven cool back to room temperature. The specimens were then separated from the build plate by wire Electrical Discharge Machining (EDM). The cylinders were machined according to ASTM E466-15 [12] to create fatigue bar specimens (Fig. 20) and the turbine blades were ground smooth to remove the AM surface roughness as described in [77]. Finally, all of the samples were heated to 718°C and held for eight hours, cooled to 621°C and held for another eight hours, and finally air cooled to age harden the material. Three of the fatigue bars were selected to characterize the material properties of density and Young's Modulus. Each turbine blade underwent Advanced Topology Optimalogy System (ATOS) scans to create a unique digital surface model for each turbine blade. The ATOS scans are a 3-D structured light scanning process which produced a point cloud corresponding to the components' surface geometries [83]. The structured light scans have been used in prior turbine blade research with a scan

accuracy of less than 8 μm to the target surfaces [80, 81].

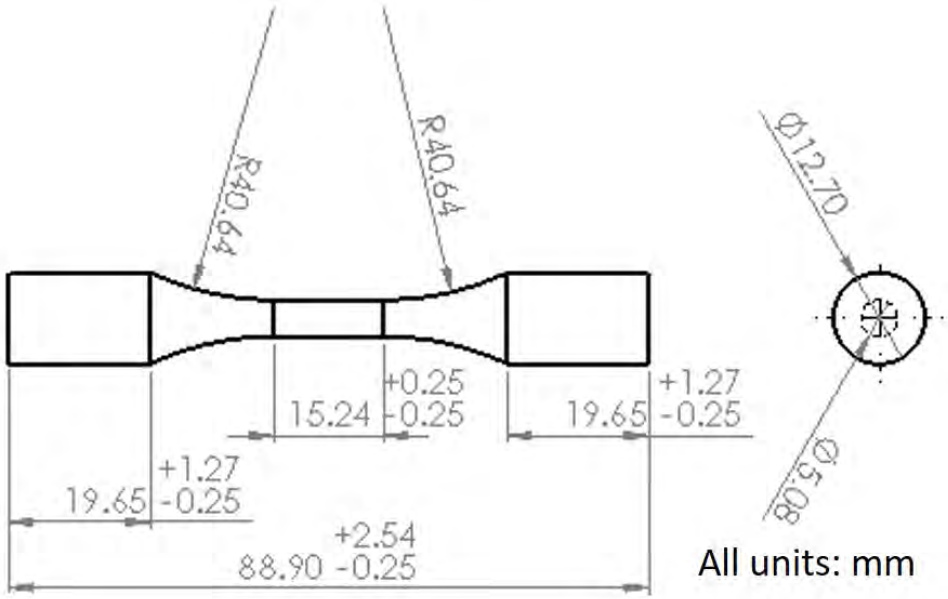

Figure 20. Fatigue bar geometry designed in accordance with ASTM E466-15 [12].

3.3.1 Material Properties

In powder based AM printers, parameters such as laser power, beam width, powder size, scan speed, and even print orientation have been shown to create different material properties for the same alloy [15, 18, 41, 67, 84]. After the print, post-processing steps further modified the material properties [17, 69, 85]. To understand how the applied print parameters and post-processing steps impacted the material properties, specimen from the same build plate were selected to measure the final properties for the AM samples.

The three selected fatigue bars (specimens 0, 11, & 14) were weighed to an accuracy of 1 mg and the volume measured by water displacement in a graduated cylinder to an accuracy of 0.5 mL. Averaging the results across the three specimens yielded a density of 8.19 g/cm^3 with a standard deviation of 0.032 g/cm^3. The measured

density was 0.4% lower than the cited wrought density, with one of the three measurements slightly above the nominal wrought density. Through these measurements, a Student T-test produced a probability of 0.316 that the measured densities and the wrought density value came from the same distribution. There was insufficient evidence to say if the AM printed material had a statistically different density from the wrought material.

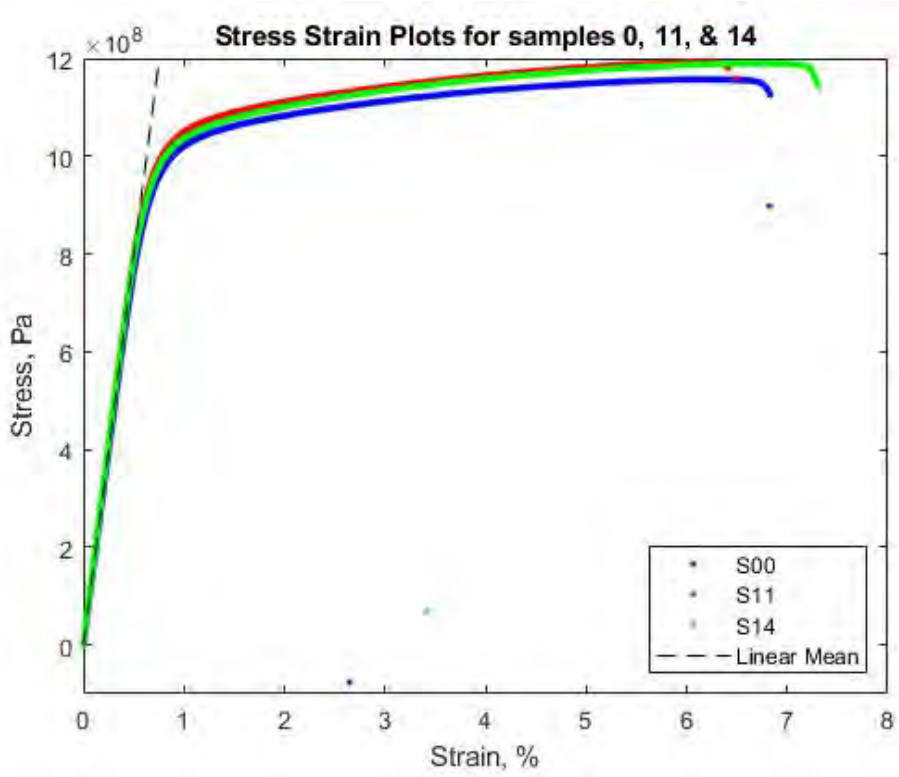

Figure 21. Stress-Strain curves from the monotonic testing.

Next the fatigue bar specimens were placed in an 810 MTS Load Frame with a 100kN Load Cell. Each specimen was instrumented with an MTS axial extensiometer (model #634.12E-24) with spring clip attachments and subject to a monotonic test to measure Young's Modulus. Figure 21 depicts the Stress-Strain curve generated from each specimen. Young's Modulus averaged 159.1 GPa with a standard deviation of 4.1 GPa across the three samples. Performing a Student T-test with the three spec-

imen measurements against the wrought material property of 199.9 GPa generated a probability of 0.0069 that the measured Young's Modulus values and the wrought value came from the same distribution. At an alpha of 0.01, the probability rejected the hypothesis that the measured values for Young's Modulus came from the same population as the wrought value for Young's Modulus.

Poisson's Ratio was not measured in these experiments and was assumed to remain at the wrought property of 0.294. Applying the measured material properties to the CAD based FEM reduced the natural frequencies in Figure 19 by 10%. Table 3 shows the new values for modes 1 & 2 with respect to the changes in material properties.

3.3.2 Geometric Deformations

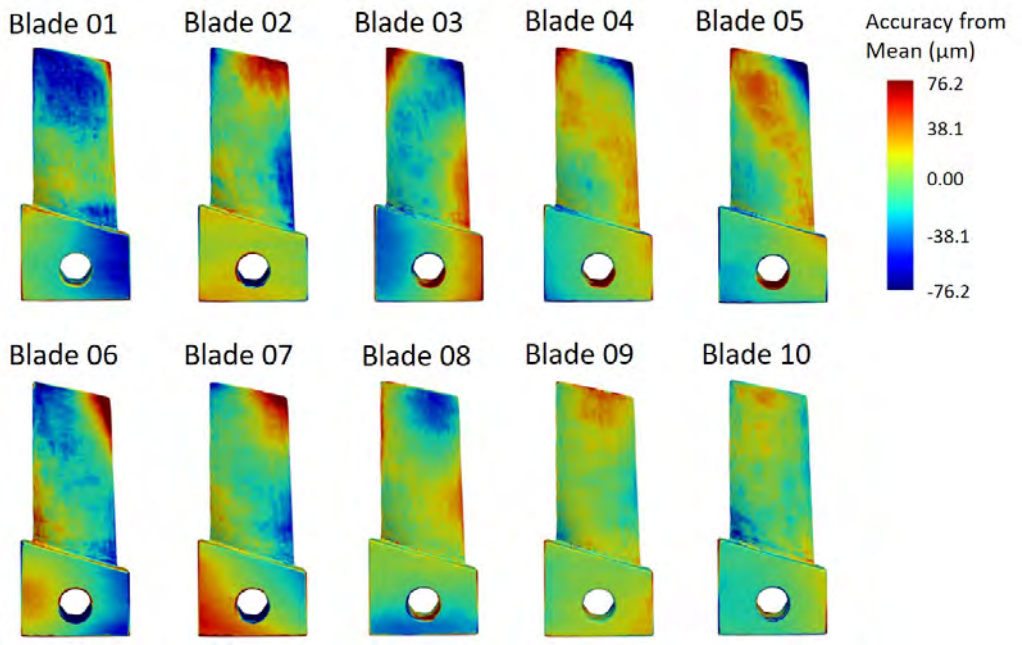

Figure 22. Heat maps between the Turbine Blade unique FEM surfaces and the average of the ATOS scanned surfaces. Red and blue areas depict where the morphed mesh was respectively above or below the scanned surface. Green areas depict where there is no variation.

Due to the rapid heating and cooling of material at localized points during the AM Process, printed specimen are subject to high levels of internal residual stresses that

cause deformations from the original design [16]. The machining process to reduce the surface roughness of the blade surfaces also added a level of uncertainty to the final shape and size of the turbine blades in relationship to the CAD design. These factors led to variations in material distribution between the printed samples and the total material in each turbine blade.

To quantify the differences between each turbine blade and the CAD model used in the AM process, each blade was subjected to an ATOS scan to accurately map the final surfaces. Three independent scans were taken for each of the ten blades. The average of the three scans created the unique blade surface. Applying the blade grip as the common reference point between surface scans and the FEM model (Fig. 17D), FEMorph re-shaped the final mesh according to the scanned surface profiles, creating a new unique FEM for each turbine blade. Across the ten blades, the mean geometric variation between the morphed FEM surfaces and the average of their scanned surfaces was 25 μm with a standard deviation of 5.5 μm. The maximum variation between the scanned surfaces and the morphed FEM geometry was 76 μm. Figure 22 is the comparison between the morphed meshes and the average of their surface scans. While the location of maximum variation was different for each mesh/scan pair, the largest discrepancies were always found in areas where the surface rapidly changed direction such as the blade edges, blade tip, and the base of the blade.

When the unique FEM surfaces were compared against the original CAD geometry (Fig. 23) with the grip region as the common reference point, the mean geometric variation across an individual blade increased to 315 μm with a standard deviation of 8.9 μm. The largest variation between the morphed FEMs and the CAD geometry was 762 μm. Figure 22 highlights the magnitude of the variation between the CAD geometry and the morphed FEMs. Where Figure 22 demonstrated that a level of variation remained between the ATOS surface scans and the morphed FEMs, that

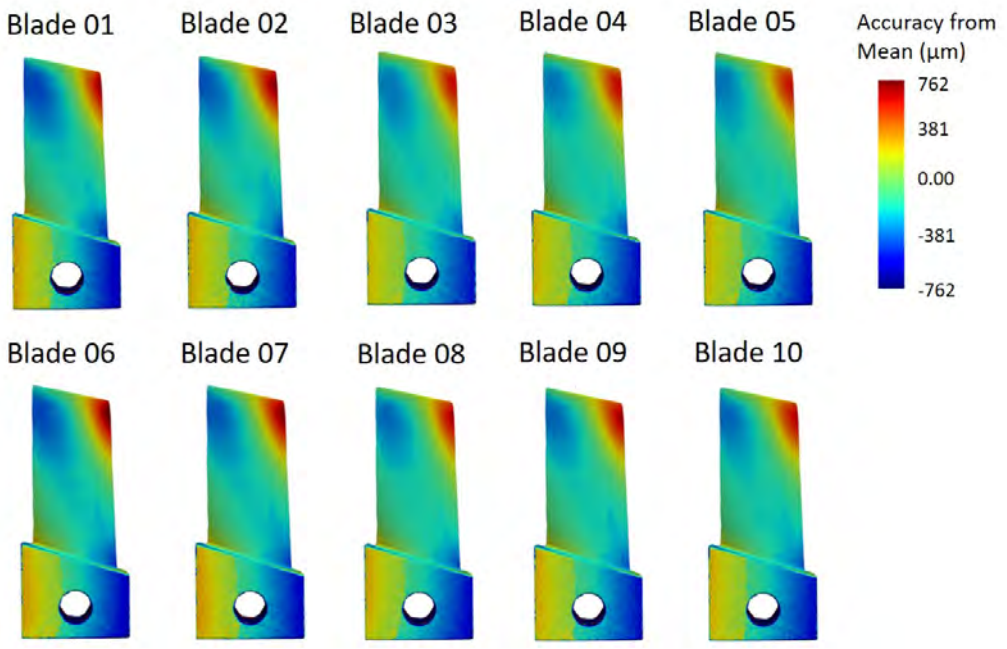

Figure 23. Heat maps between the Turbine Blade unique FEM surfaces and the CAD geometry. Red and blue areas depict where the morphed mesh was respectively above or below the scanned surface. Green areas depict where there was little to no variation. Each turbine blade demonstrated a consistent deviation from the CAD design, suggesting a repeat-ability to the final design with the applied processing steps.

variation was insignificant compared to the deviations between the CAD design and the final FEM geometries. Across all ten blades, the point of maximum variation was always at the top right corner of the turbine blade. The processing steps that generated the deviations from the CAD design proved to be consistent and repeatable for each hardware sample. That corner of the scanned blade surface deformed off of the CAD design between 300 μm and 762 μm. The CAD design was approximately 310 μm thick at the corresponding blade corner, making this distortion one to two corner thicknesses different from the designed geometry.

By morphing the CAD based FEM to match the ATOS scanned unique blade geometries and applying the measured material properties to each turbine blade FEM, a digital replica model was created for each AM turbine blade test specimen. The digital replicas generated unique natural frequencies, stress maps, and peak stress

locations. The concept was that a more accurate FEM model would produce a better representation of the hardware. For the desired fatigue life modeling, the stress mapping capabilities of the digital replica FEMs was the highest priority. The next step was validation that the generated digital replicas improved the representation of their hardware counterparts.

3.4 Digital Replica Validation

The final phase of the digital replica development was validation of the digital replica models against bench testing of the turbine blade hardware. To validate the digital replicas, the parameters of mass, volume, natural frequencies, and strain ratios were studied to quantify how much the digital replica process improved the software to hardware relationship.

3.4.1 Physical Variations

	Finite Element Models			Hardware	
	Wrought Mass (g)	Printed Mass (g)	Volume (mm^3)	Mass (g)	Volume (mm^3)
CAD	529	527	64356.98	-	-
Blade 01	495	493	60234.59	490	59845.61
Blade 02	495	494	60258.18	492	59785.49
Blade 03	495	494	60279.16	492	59837.36
Blade 04	494	492	60115.61	492	59671.88
Blade 05	494	492	60105.62	492	59651.01
Blade 06	496	495	60398.46	484	59957.17
Blade 07	496	494	60341.59	492	59872.46
Blade 08	496	494	60345.69	492	59893.43
Blade 09	496	494	60291.94	494	59821.73
Blade 10	494	492	60087.43	492	59797.50
Sample Mean	495.1	493.4	60245.83	491.2	59813.36
Sample Std Dev	0.88	1.08	109.37	2.70	94.09

Table 2. Mass and volume data for each model and measured data from the printed turbine blade specimen.

Table 2 is the mass and volume associated with each model. Applying a Student T-test between the digital replica FEM masses using the wrought density and the measured print density (Fig. 24A) generated a probability of 5.52×10^{-4} that the masses are from the same distribution. While the overall mass change due to the different densities was on the order of 1-2 grams, there were sufficient samples to demonstrate a statistically different mass distribution for the unique geometry FEMs between applying the nominal wrought density and the AM print density to the FEM volumes. Applying the same test between the digital replica FEMs with the printed material properties and the measured mass of the printed turbine blades (Fig. 24A) generated a probability of 0.014, which is not statistically significant with the desired alpha of 0.01. This demonstrated that while the change in density between the wrought and printed material was determined statistically insignificant, the small change in density created a statistically measurable difference in replicating the hardware masses in the digital replica models.

Looking at the total component volume, both the FEM volumes and the measured hardware volumes were statistically smaller than the CAD designed volume. This confirmed that a significant volume was lost through the print and post-processing steps. The comparison between the digital replica volumes and the measured hardware volumes produced a probability of 1.01×10^{-8} that the measurements came from the same distribution. Figure 24B depicts the distribution functions from the digital replicas and the scan volumes. While the probability of the digital replica volumes and measured hardware volumes were not considered statistically significant, the digital replicas demonstrated a large improvement over using the "as-designed" geometry volume.

Finally, with both mass and volume measured for the turbine blades, the density of each turbine blade was re-evaluated. Across the ten specimen, the density averaged

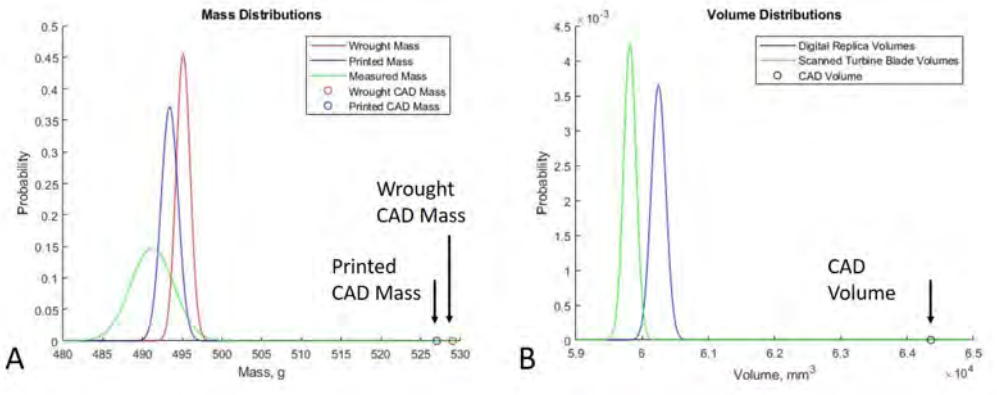

Figure 24. A) Mass distributions using the digital replicas with the wrought material properties, digital replicas with the measured material properties, and hardware measurements. B) Volume distributions between the digital replica FEMs and the measured ATOS scan volumes.

8.21 g/cm^3 with a standard deviation of 0.05 g/cm^3. While marginally closer to the wrought material properties than the fatigue bar based measured material properties, there is no statistical relevance between the density distributions.

3.4.2 Natural Frequencies

The next level of validation evaluated the natural frequencies of the digital replica FEM models against the measured natural frequencies of the printed turbine blades. Each turbine blade was mounted on an Unholtz-Dickie 20K Electrodynamic Shaker Table and subjected to a 0.1g-force sine sweep from 300 Hz to 1600 Hz. The test results were compared to the "as-designed" FEM with wrought and measured material properties as well as the unique blade FEMs with both material properties.

Figure 25 depicts the Probability Distribution Functions (PDFs) of the first two modes for the FEM material variations and the experimental turbine blade testing. The changes in material properties from the nominal wrought material properties to the printed material properties resulted in a 10% reduction in the predicted frequencies of the first and second modes. The geometry corrections from the CAD design to the unique measured surfaces accounted for a 1-2% reduction in the natural fre-

	Mode 1			Mode 2		
	Wrought (Hz)	Printed (Hz)	Test (Hz)	Wrought (Hz)	Printed (Hz)	Test (Hz)
CAD	515.52	462.58	-	1531.0	1379.3	-
Blade 01	507.13	455.21	485.8	1516.6	1366.8	1451.1
Blade 02	507.07	455.17	478.2	1511.7	1362.0	1451.6
Blade 03	505.61	463.82	490.8	1509.6	1360.1	1475.6
Blade 04	506.17	454.38	491.3	1511.9	1362.4	1447.1
Blade 05	507.35	455.41	491.6	1513.1	1363.2	1432.8
Blade 06	508.00	456.02	467.3	1517.3	1367.3	1478.0
Blade 07	506.45	454.60	472.8	1516.3	1366.3	1490.9
Blade 08	505.20	453.43	486.8	1510.6	1361.0	1493.4
Blade 09	507.61	455.69	482.3	1516.3	1366.5	1460.7
Blade 10	506.36	454.46	483.3	1512.4	1362.4	1458.9
Sample Mean	506.70	452.55	483.0	1513.6	1351.9	1464.0
Sample Std Dev	0.89	0.80	8.17	2.80	2.52	19.82

Table 3. Mode 1 and Mode 2 Frequency Data

quencies. Figure 25 demonstrated that the frequency predictions from Abaqus were dominated by the material properties. For any frequency dependent analysis, extreme care should be taken to understand how the AM design process impacts the material properties.

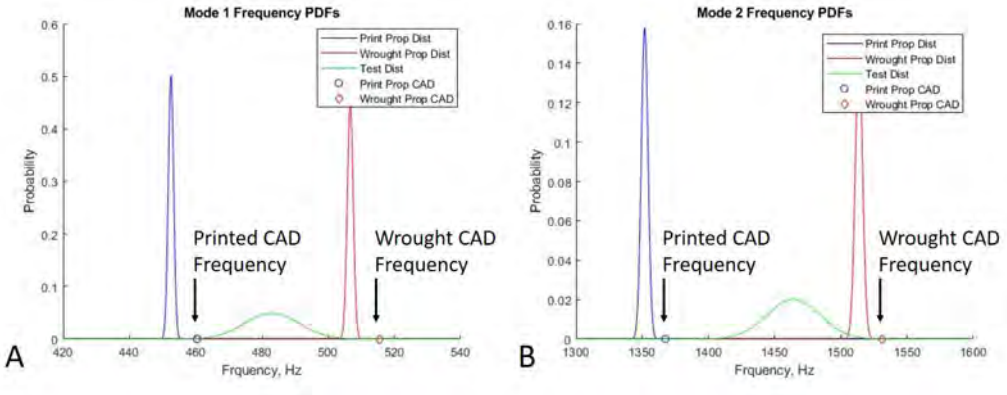

Figure 25. A) Frequency distributions for mode 1. B) Frequency distributions for mode 2.

From classical beam theory (Eq. 16), the natural frequency was controlled by λ (a constant dependent on the desired mode and boundary conditions), E (Young's

Modulus), I (Moment of Inertia), ρ (material density), and A (cross sectional area). With no change in the mode or boundary conditions, λ became a fixed constant. The geometric updates to the digital replica FEMs almost completely reduced the geometric variations between the FEMs and the experimental hardware, allowing I and A to be assumed constant as well. With those simplifications, the natural frequencies reduced to proportional to the square root of Young's Modulus over material density (Eq. 17) for each fixed geometry. With the density verified as statistically indistinguishable through the measured mass, Young's Modulus was the last input parameter to control the predicted natural frequencies. To determine the optimal value for Young's Modulus to match the digital replica models to the experimental frequencies, Equation 17 was applied twice, once to remove the modeled material properties and a second time to apply a new value for Young's Modulus. Optimally, Young's Modulus should have been 180 GPa to 185 GPa for the digital replica FEMs to match with the experimental values. The range of optimal values was not statistically different from the measured distribution of values for Young's Modulus. While none of the FEMs predicted the experimental frequency values, the predicted optimal Young's Modulus value was not statistically significant and did not warrant changing the printed material property applied in the FEMs.

$$\omega = \lambda^2 \sqrt{\frac{EI}{(\rho A)}} \tag{16}$$

$$\omega \propto \sqrt{\frac{E}{\rho}} \tag{17}$$

3.4.3 Strain Ratio Comparisons

The strain ratios between the digital replicas and the tested hardware were based on the second bending mode. Prior research with these blades [50] demonstrated that

the second bending mode had the best balance between test duration and the ability to add energy to the system. Above 2,000 Hz, the Unholtz-Dickie 20K Electrodynamic Shaker Table had diminishing capabilities to generate fatigue life failure for this blade design. While the first mode could also generate fatigue life failure, the driving frequency would increase test duration by a factor of three. The second bending mode (Fig. 19C) of the printed turbine blades was the nearest mode to minimize the test duration while optimizing the applied energy to the turbine blades during testing.

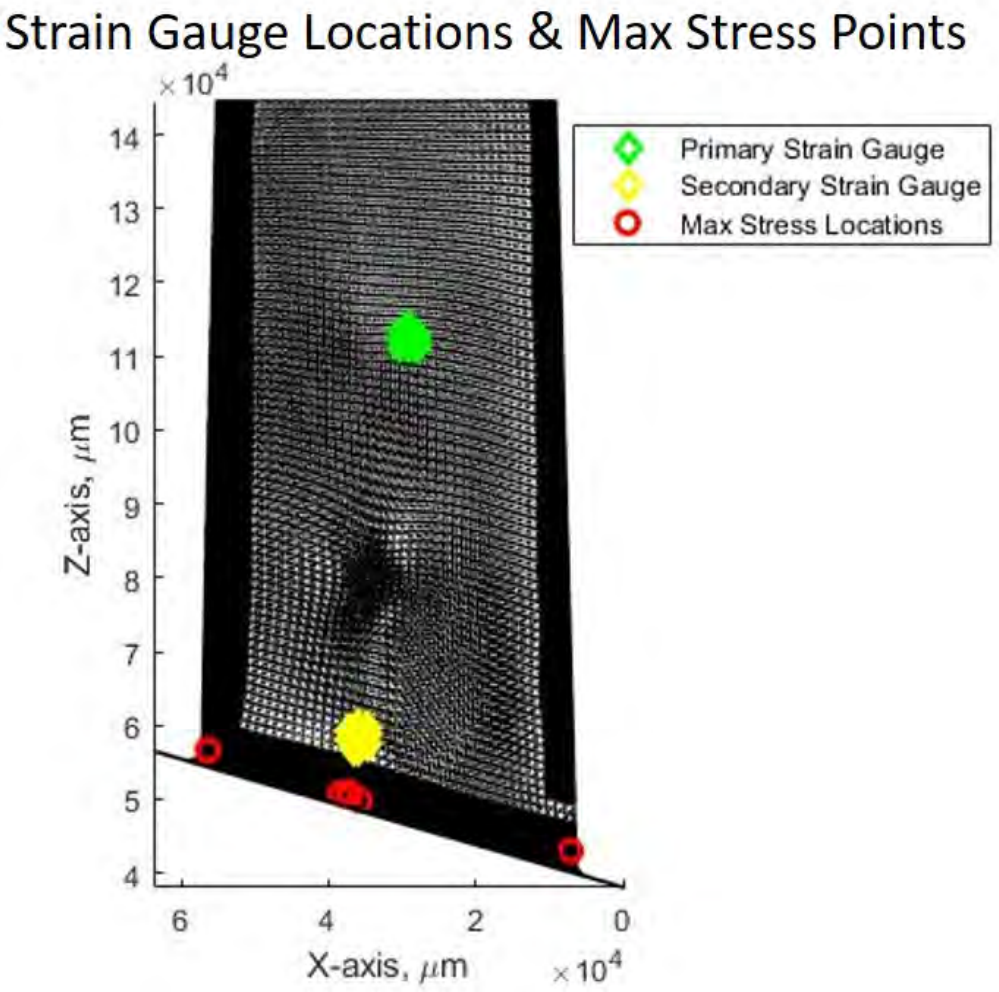

Figure 26. Primary and Secondary strain gauge locations on the turbine blades in green and yellow. The red circles along the bottom are the points of maximum stress for each turbine blade digital replica FEM.

Three points of interest were analyzed on the FEMs to relate the strain prediction accuracy. Two axial strain gauges collected data on the turbine blade surfaces (Fig. 26). Application points were identified on each blade through filtering techniques to find common points where the strain values fluctuated by less than 1×10^{-4} mm/mm within a 2 mm radius for the second bending mode and where the surface geometry did not contain large variations for ease of application. The primary strain gauge was at the local maximum strain point of the second bending mode. The secondary gauge location had an additional criterion to be on the other side of a mode 2 vibrational node from the primary strain gauge. This requirement allowed confirmation that the mode being tested was the second bending mode.

The third data point of interest was the maximum strain point for each digital replica model (Fig. 26) and the "as-designed" CAD FEM. The CAD FEM predicted the maximum strain point at the center of the blade root. Five of the digital replica models predicted similar maximum strain points with minor differences due to the geometric variations. The other five digital replica models predicted either the leading or trailing edges of the blade root to experience the maximum strain.

The FEM frequency analysis generated the natural frequencies, mode shapes, and a strain map for each mode normalized to a maximum displacement of one unit length. Since the FEMs only generated normalized values, this development used the ratio of the measured strain gauge values over the predicted gauge location strains. Averaging the ratio between the applied gauges for each turbine blade created the scale value for the digital replica FEMs. By scaling the digital replica strain maps, the maximum applied strain for each component was computed.

The measured strain values from the primary strain gauge ranged between 43% and 185% of the predicted value based on the CAD model. The same measured values were between 105% and 110% of the predicted strains when compared to their digital

replicas. The addition of geometric variations significantly tightened the quality of the predictive strain values. While the measured components were both higher and lower than the CAD based FEM, every specimen tested measured a marginally higher strain than what its digital replica predicted.

The secondary gauge location was analyzed by the same process. The measured strain values divided by the CAD based prediction were 49% to 231%. When divided by their digital replica predictions, the percentages changed to 93% to 98%. The collected strain data and the comparisons to the different FEMs demonstrated the criticality of the geometric variations generated during the AM process. Across the sampled locations, the measured strain values differed from the CAD based predictions by a factor of two with no consistency for a high or low estimate. Any optimization work based on the FEM stress/strain values would require a large factor of safety to produce a reliable component. By accounting for the the geometric variations in the AM process, the digital replica FEMs produced strain values that were within 10% of the experimental data, freeing up the design space to solve for the optimal solution.

Due to the normalized nature of the FEM results, the applied material property changes did not impact the strain ratios. For this research the strain relationship was the primary purpose of the digital replica models.

3.5 Summary Remarks

The digital replica models developed here were good representatives of their hardware counterparts and proved to be significant improvements over the "as-designed" models for vibrational analysis. By analyzing the material properties and geometric deformations and applying the measured results to create digital replica models, incremental improvements were made to the FEMs, generating a more precise rep-

resentation of the test hardware. The amount of model variation depended on the parameters being changed.

- The measured geometric variations for the AM build only accounted for 1-2% of the variation in natural frequency predictions. For analysis where natural frequency is the primary consideration, the geometric precision gained through the ATOS scans was not significant.

- The measured geometric variations for the AM build significantly improved the stress and strain maps generated from the FEM frequency analysis. Where the measured stain values ranged within 2x of the predicted "as-designed" model, the same measurements were within 10% of their respective digital replicas.

There are several areas of uncertainty that can be considered for improving the model fidelity.

- The variations in material properties due to changes in the AM process is an active area of research. The measured material properties were from fatigue bars printed on one side of the build plate. The fatigue bars were also machined to shape instead of printed to shape, which changed the surface structure. Both factors introduced a level of uncertainty when applying the material properties to the turbine blades. The frequency validation demonstrated that even seemingly insignificant changes to the material properties yield large variations in the frequency response.

- Uncertainties associated with the the final surface geometry when compared to the CAD design still exist. The ATOS scanning framework gives the opportunity to conduct probabilistic analysis on the expected variations between the design and final product due to the AM processes. Each turbine blade was

scanned three times to help control imaging artifacts. By further analyzing how the scanned geometries vary from the CAD design at different process phases, a comprehensive distortion matrix will be developed.

- The FEM morphing process introduced additional variations to the scanned geometries due to internal smoothing filters. This work demonstrated that the digital replica FEMs were different from the ATOS scanned geometries. Further development of that relationship will lead to additional FEM convergence requirements, denoting the required mesh density based on the desired level of geometric accuracy.

The parameters presented in this paper are a good foundation for digital replica development of AM components for structural analysis. Small variations to the material properties and component geometry created large differences in the vibrational response and predicted strain maps. The level of fidelity in the digital replica model and purpose of creation drives the required precision in the component characterization. A frequency analysis was driven more by material properties than geometric variations, while stain mapping was dominated by the geometry. The validated digital replicas developed for this research were for the purpose of improving fatigue life predictions.

IV. El-Haddad Model Development

4.1 Overview

AM presents several challenges to aircraft and satellite design. A leading drawback to applying AM techniques to an aircraft structure is the degradation in fatigue performance due to the naturally forming defects [86]. The AM process generates defects from small voids to large cracks, and several studies have looked at how the defect size can be used to predict the fatigue life of AM components [4,8,11,19] based on the Kitagawa-Takahashi (KT) fatigue life model and the El-Haddad fatigue life model [21,22]. The current techniques assume that the worst-case defect will occur at the highest stress concentration point. This creates a conservative fatigue life estimate that restricts component geometry design space and inhibits the development of AM components for limited life applications.

The LoF defect type is of particular interest to fatigue life as a crack initiation point due to the size and shape. LoF defects tend to form flat separations that cover a relatively large area. This creates a large stress concentration point that propagates crack growth. In contrast, void defects are t̃wo orders of magnitude smaller and are spherical in nature. The difference in size and lack of sharp edges typically minimizes the importance of void defects in fatigue life studies. However, a small defect in a high stress location can be more damaging to fatigue life than a large defect in a low stress region.

Digital twin techniques utilize Finite Element Models (FEMs) to simulate load cases and predict mission capabilities [87]. By applying the same techniques, this research advanced the El-Haddad model by combining it with Finite Element Analysis (FEA) to explore the effects of defect location in conjunction with defect size to predict where and when critical fatigue failure could occur. The experimental

component studies fatigue bars in axial loading and a turbine blade design subjected to vibrational loading fatigue tests. The fatigue life data is compared to the model predicted life to validate the model as an accurate representation of the relationship between defect size, location, and fatigue life. The measured defect locations are evaluated against the model predicted failure locations to assess the accuracy of the augmented model to predict where a fatal defect can form for a given design life and maximum defect size.

This paper develops the criteria to predict where a component will fail using the finite fatigue life El-Haddad model in conjunction with FEA. The critical failure location criteria is developed using a simulated defect distribution across a turbine blade model with the design choices of maximum defect size and design life. Critical failure location predictions are then verified through testing of AM printed turbine blades (Fig. 27).

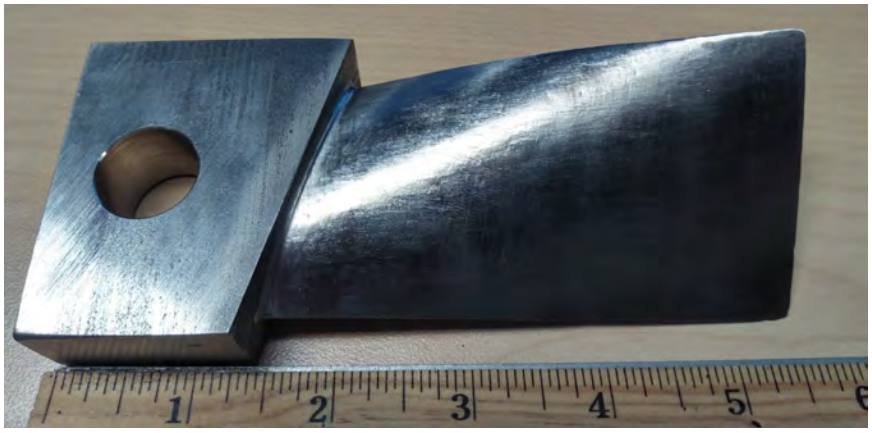

Figure 27. Turbine blade specimen printed in IN718.

4.2 Fatigue Life Modeling with Defects

The El-Haddad fatigue limit model was previously converted to model finite fatigue life (Eq. 15) [11]. Using the material properties defined in Table 1 and applying the outputs from Equations 1 and 12 into Equation 15 across a range of finite fa-

tigue life values and crack sizes yields Figure 28. View A is in the orientation of a traditional S-N curve. As the cyclic stress decreases, the fatigue life increases. The top bound in view A is the Basquin fit (Eq. 1) using the material properties from Table 1. View B shows the traditional El-Haddad curves calculated at various design life levels. As the initial crack size increases, the allowable applied stress range to maintain a constant life curve decreases. The bend in the curve between material fatigue limit and LEFM shifts to the right as desired life decreases. This shift means that as the life requirements decrease, larger defects are allowed to exist before LEFM becomes the dominate crack growth mechanism. If the defects are kept below $a_{0,N}$, they have negligible impact to the fatigue life when compared to the material fatigue limit. When the crack size gets above $a_{0,N}$, LEFM and the material crack growth properties become important factors in determining fatigue life.

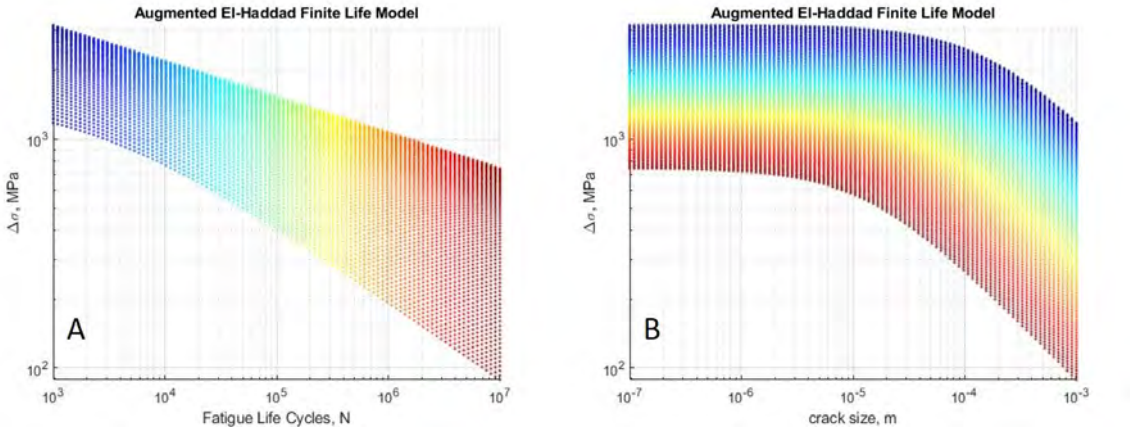

Figure 28. Finite Life surface relating initial crack size, cyclic stress at the fracture initiation point, and final fatigue life. A) Life/$\Delta\sigma$ relationship. The Basquin equation defines the upper limit of the model. B) Crack size/$\Delta\sigma$ relationship. Traditional El-Haddad curves build from equation 15 for different design lives, N.

There is a defect location dependence buried in figure 28 based on the stress profile of the component being tested and the volume of the component that experiences the maximum applied stress. For a specimen, such as fatigue bars, subject to uniform uniaxial loading, there is a substantial volume of material experiencing the

maximum applied stress. This enables the assumption that a large defect will form in the maximum stress region and initiate failure. The defect location information is simplified down to surface or interior defect and only impacts the applied shape factor [57]. In other cases, such as bending loads, the volume of material subject to the maximum applied stress is very small. In three point bending tests, failure has been documented in AM components due to defects located away from the maximum stress location [78]. The augmented El-Haddad model (Fig. 28) is a surface defined by three values: the defect size, the applied stress, and the life associated with growing the defect to failure. In many real-world situations, the applied stress is varied throughout the geometry and is determined by the component geometry and the applied boundary conditions. Knowledge of two values enables the prediction of the third. For simple structures the defect location applied stress may be directly calculated, but for more complicated systems, a Finite Element Model (FEM) creates a map to relate location to stress for an assumed load case.

4.3 Turbine Blade Simulation

Simulations using the augmented El-Haddad model utilize a generic turbine blade design subject to a vibrational load state to generate a mapping of stress to location. An FEM is created to estimate the stress profile across the turbine blade when the base is fixed, and the blade is subjected to a vibrational load to induce the second bending mode. The turbine blade (Fig. 29A) is meshed with 223,500 quadratic hexahedral elements and processed in Abaqus 6.14. When the grip is fully constrained on the top and bottom surfaces and the model subjected to a dynamic frequency analysis, the second bending mode and the associated normalized stress map is computed (Fig. 29B). After completion of the FEM simulation, the grip is removed leaving just the blade material composed of 47,500 elements with 210,600 nodes.

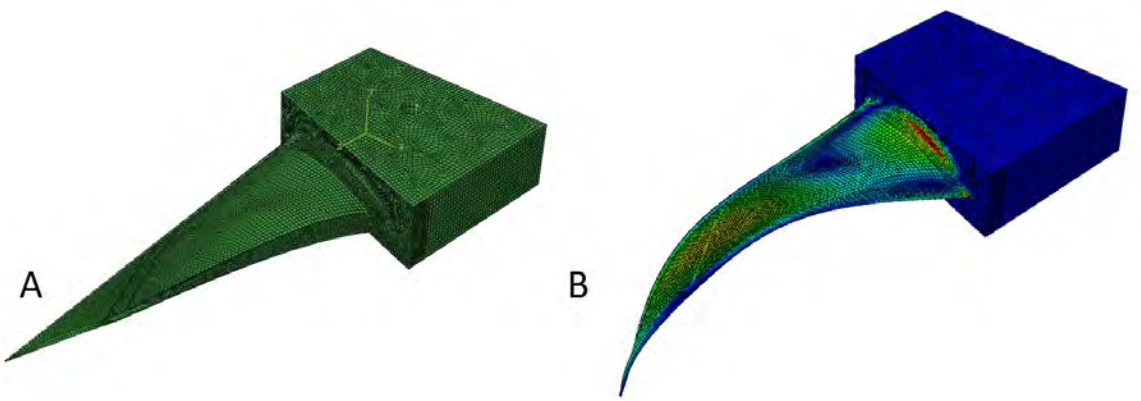

Figure 29. A) Mesh of the generic turbine blade. B) Second bending mode.

4.3.1 Defect Generation

The defect sizes and locations needed for the augmented El-Haddad model are initially simulated using a fitted defect distribution (Fig. 30) for nickel-based superalloy 718 [66]. The distribution mean fit equation was developed for the same material across a range of print parameters encompassing those applied to this research. The integers on the Y-axis correspond to the number of nines in the Cumulative Distribution Function (CDF) probability (ex: y = 3, F = 0.999). Defect sizes of assumed spherical shape are pulled at random from the population until the volume of defects reaches 0.1% of the total volume of the blade. The procedure generates 155,000 to 160,000 defects that are randomly assigned by a uniform distribution to FEM nodes within the turbine blade. Generated defects range from $14\mu m$ up to $960\mu m$.

4.3.2 Stress Map

The FEM frequency analysis calculates the natural frequency, mode shape, and the relative stress and strain profile for the first five modes. The second bending mode for the constrained turbine blade is 1379 Hz and the shape is seen in figure 29B. The maximum stress for this load condition is located on the surface of the blade at the root. Only 2.5% of the blade volume is subject to stress levels within 50% of the

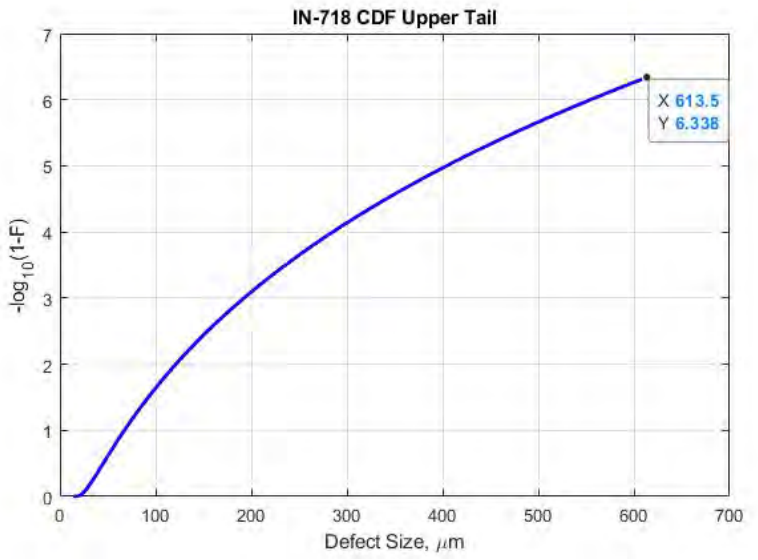

Figure 30. Defect CDF for nickel-based superalloy 718

maximum stress. From equation 6, if the stress level is cut in half, the defect size must increase by a factor of four to maintain the same SIF. The Abaqus default stress and strain profiles are normalized to a maximum displacement of 1 unit, by scaling the stress values that generated figure 29B to the stress range calculated by equation 1 for a desired defect free life, an estimate of the applied stress is generated for every point within the turbine blade.

Coupling the developed stress map with the locations of the defects randomly simulated across the turbine blade creates the second parameter needed for the augmented El-Haddad model: the applied stress at the defect locations. For these simulations, the maximum applied stress is scaled to 1075 MPa, which corresponds to a defect free design life of 10^6 cycles. Applying the defect size and stress at location for every defect in one case to the augmented El-Haddad model creates figure 31. Every defect has an associated fatigue life based on the maximum stress at its location that is calculated without any influence from the other defects. The white line in figure 31A represents the 10^6 fatigue life curve. Any defect above the curve is predicted to cause pre-mature failure. Defects below the curve are predicted to fail after the design

life. In this case, the largest defect generated is 495μm diameter at a location that only experiences 21.7% of the maximum stress. The largest defect has been randomly placed in a location that does not experience enough stress to grow the crack within the design life. The first failure point is predicted at a 139μm diameter defect at a location experiencing 93% of the maximum stress. Only 4% of the 1064 cases ran predicted the largest generated defect to cause first failure, while 30% of the cases failed due to a small defect at the maximum stress location.

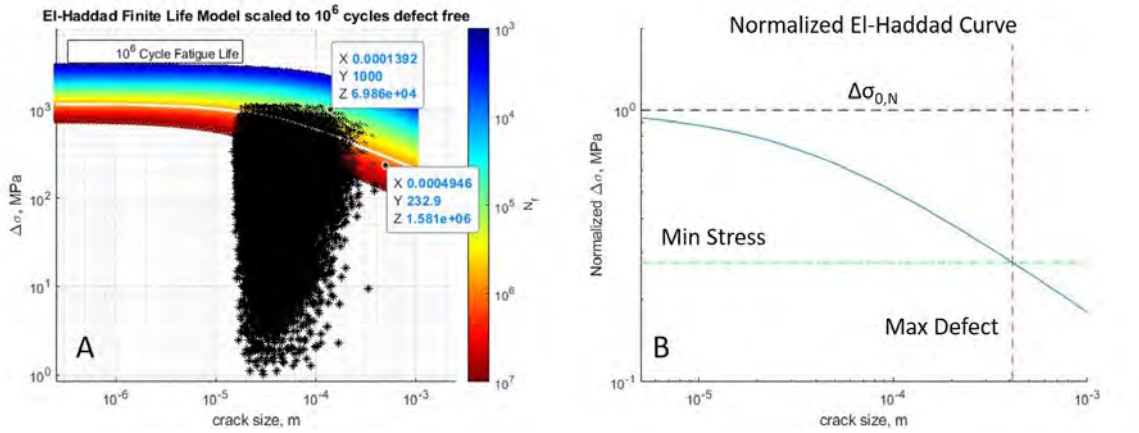

Figure 31. A) Finite life model with 159,000 defects randomly distributed throughout the component. Sizes range from 0.015 mm to 0.41 mm. B) Minimum stress level that could cause failure for a design life and maximum defect size.

4.3.3 Model Outputs

There are many outputs that can be generated from the model. The simplest outputs involve picking two of the values and solving for the third as was done in figure 31A where the defect size and stress are defined, and the life is predicted. The model works just as easily to pick a desired life and defect size to determine the maximum allowed stress at the defect location. This level of output only requires knowledge of the material properties to build the augmented El-Haddad model.

The next level of outputs make inferences on parameter limits. Using the applied defect distribution (Fig. 30) with a desired probability of occurrence to generate a

maximum defect size and applying a design life, N, a minimum stress level is identified by the intersection of the El-Haddad curve for N cycles and the maximum defect expected (Fig. 31B). This value of minimum stress defines the stress level where defects will not interfere with the material fatigue life. Likewise, by intersecting the maximum defect size with $\Delta\sigma_{0,N}$ (Fig. 31B), the worst case life assessment is made. This is the life that will be achieved if the largest defect does coincide with the maximum stress location.

The final level of outputs requires knowledge of the geometry and load case. By plotting every location on the geometry that experiences the minimum stress from figure 31B or higher, critical failure locations are predicted. Both shorter design lives and smaller maximum defects reduce the size of the critical failure locations. In the examples in figure 32, when the CDF probability is desired at 0.99999, the maximum defect corresponds very near to $400\mu m$. Similarly, when the CDF probability is only desired at 0.999, the maximum defect is approximately $200\mu m$. From figure 32A to 32B the reduction in maximum defect size of interest moves the intersection of the maximum defect and El-Haddad curve up and to the left, allowing higher stresses to be considered non-critical and reducing the critical failure location volume. Figure 32A to 32C keeps the same maximum defect size, but decreases the design life from 10^6 to 10^5 cycles. The reduction in design life shifts the El-Haddad curve up and to the right, minimizing the effects of LEFM on the fatigue life for the same defect sizes. These critical failure maps inform where a component needs to be inspected for a given load case and expected defect population.

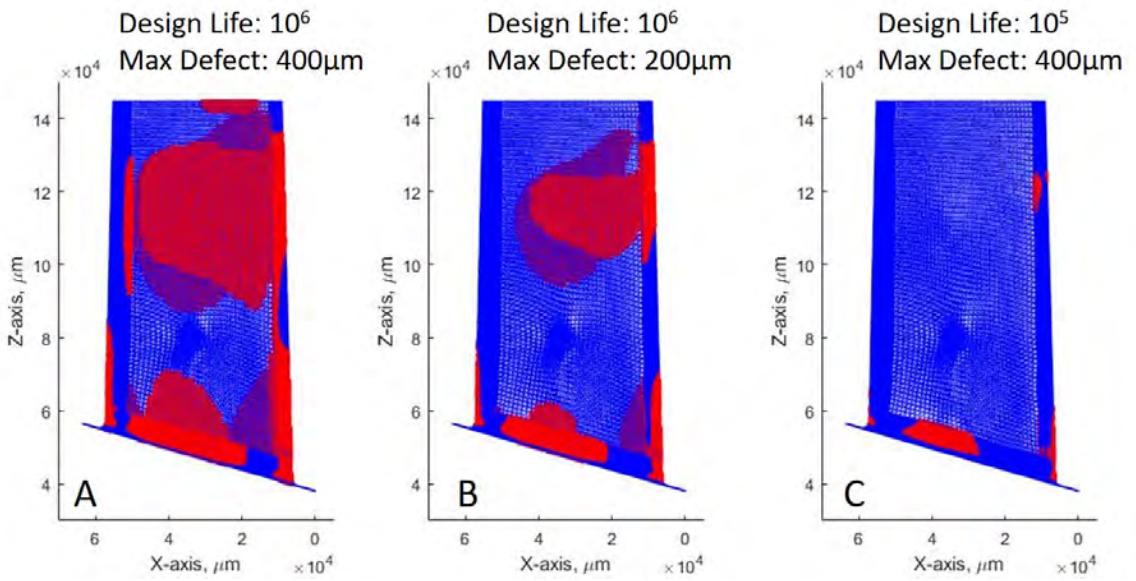

Figure 32. Turbine blade geometry represented in blue with red regions denoting the critical failure locations. A) 10^6 **cycle design life, assumed maximum defect of** $400\mu m$**. B)** 10^6 **cycle design life, assumed maximum defect of** $200\mu m$**. C)** 10^5 **cycle design life, assumed maximum defect of** $400\mu m$**.**

4.4 Hardware Development

To verify the functionality of the augmented El-Haddad model and the accuracy of the outputs, ten turbine blades and eighteen cylindrical specimen were printed from nickel-based superalloy 718 (Fig. 33). Post-print, the specimen were subject to a stress relief anneal and the cylindrical specimen were machined to fatigue bars according to ASTM E466-15 [12].

As seen in the aerospace industry, uncertainties and variabilities in the hardware make performance predictions from a single FEM challenging [88, 89]. This research performed preliminary testing and characterization on the specimen post-processing. Material characterization testing limits the variability associated with AM material properties. Measuring the surface geometry of each turbine blade quantifies the variability associated print geometry tolerances and thermal stress based deformations.

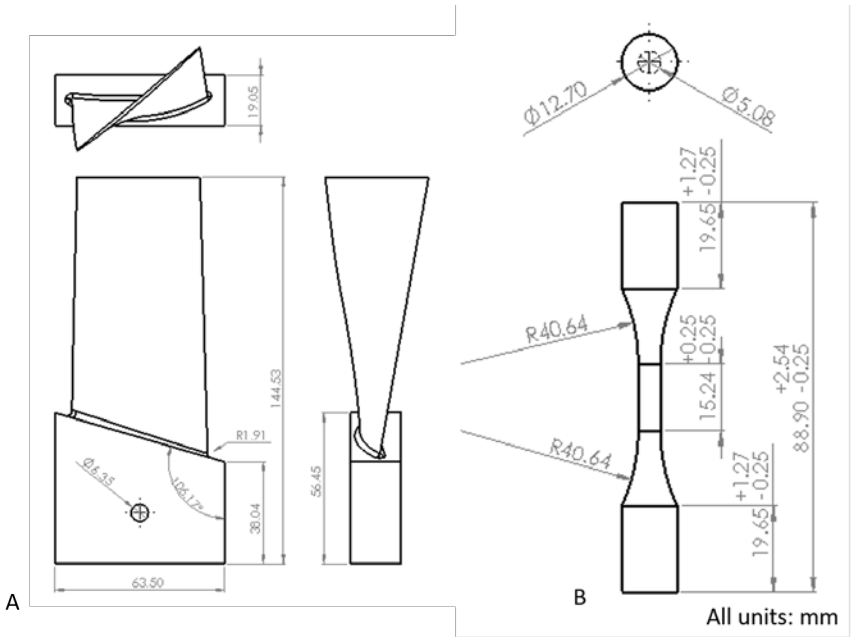

Figure 33. A) Dimensions for the turbine blades. B) Dimensions for the fatigue bars [12]

4.4.1 Specimen Post-Processing

The parts were printed on an M2 Cusing Laser Powder Bed Fusion (LPBF) printer with three regional parameter settings: core, skin, and contour (Table 4). The contour scan is a single thin line around the edge of the surface to ensure a good melt along the geometry surface. The skin scan is the small region from the surface $\sim 1.5mm$ into the geometry. This is a tight scan pattern near the surface to create a high-density region near the surface of the component with fewer defects. Finally, the core scan is a high power setting that scans every other build layer on the interior of the part following an island scan pattern. The core parameters sacrifice print quality to improve print speed.

Post-print, the parts were processed by a stress relief heat treatment, machining, age hardening, and a final polish process. The stress relief heat treatment put the whole build plate into an oven at 1000°C for one hour and then left to oven cool back to room temperature.

	Contour	Skin	Core
Power (W)	120	180	320
Layer Height (μm)	40	40	80
Scan Speed (mm/s)	280	800	700
Spot Size (μm)	50	130	180
Trace Spacing (μm)	N/A	105	130
Offset (μm)	90	95	130

Table 4. M2 Cusing Printer scan settings.

The specimens were then removed from the build plate. The cylindrical specimen were machined down according to ASTM E466-15 [12] to match the specification in figure 33B. The turbine blades were machined along the grip to ensure parallel surfaces on the front and back and enlarge the grip hole to 19mm (0.75in) for a secure mount to the test fixture. The blades were rough polished with sandpaper to remove the oxidation layer before aging. The sanding process reduced the surface roughness to a value of $S_a = 4.35\mu m \pm 1.26\mu m$. The surface roughness measurements are in accordance with ISO 25178 [90].

The aging process was performed according to AMS2774-G [91]. The nickel-based superalloy 718 components were heated to 718°C and held for eight hours, cooled to 621°C and held for another eight hours, and finally air cooled. Post aging, the turbine blades and fatigue bars were subject to a final polishing. The turbine blades were polished using a pneumatic dremel with polishing stones and finished with a very fine polishing pad. The final surface roughness for the turbine blades is $S_a = 3.19\mu m \pm 0.81\mu m$.

4.4.2 Geometry Variability

To bypass the variability associated with using standard material properties in the FEM, three of the fatigue bars (Fatigue Bars 00, 11, & 14) were subject to monotonic tensile testing to measure the density and Young's Modulus for this print

to improve the accuracy of the FEM. The density and Young's Modulus were directly measured for this build as $8.19e^{-3}g/mm^3$ and $159GPa$ respectively. Due to AM printing processes, post processing thermal environments, and the various polishing steps involved to make each turbine blade ready for testing, some level of structural variation was expected between the turbine blade Computer Aided Design (CAD) file and the final blade geometries. Using Advanced Topology Optimalogy System (ATOS) scans to generate a point cloud of each turbine blade surface, a measured surface geometry was built for each blade. Three scans were taken for each turbine blade and averaged together to create a geometrically accurate surface for each blade. The scanned surfaces have a maximum variation of $76\mu m$ from the individual scans to the mean blade surface, and an average variation of $25\mu m \pm 5.5\mu m$ across all of the blade specimen. Finally, the turbine blade FEM (Fig. 29A) is morphed to align with each unique turbine blade surface using FEMorph to create an FEM for each turbine blade that matches the final geometry for every specimen. When comparing the scanned blade surfaces to the CAD file (Fig. 34A), there is an average variation of $315\mu m \pm 9\mu m$ with a maximum variation of $750\mu m$. In every case, the printed geometry tilts slightly forward of the CAD file so that the largest variation is at the blade tip (Fig. 34B).

Using the unique FEM for each turbine blade and the measured material properties from the monotonic testing, a frequency analysis was run for every turbine blade. Where the CAD based FEM predicted the second bending at 1379 Hz, the geometrically variant turbine blade FEMs predicted the second bending at 1364 Hz $\pm$ 2.5 Hz. From each unique turbine blade FEM, individual stress maps were generated from the second bending mode. At this point, each turbine blade has a digital twin FEM with minimized variability between the FEM and hardware sample. Uncertainties still exist in the form of defect size and location in the hardware that is not captured

by the FEMs.

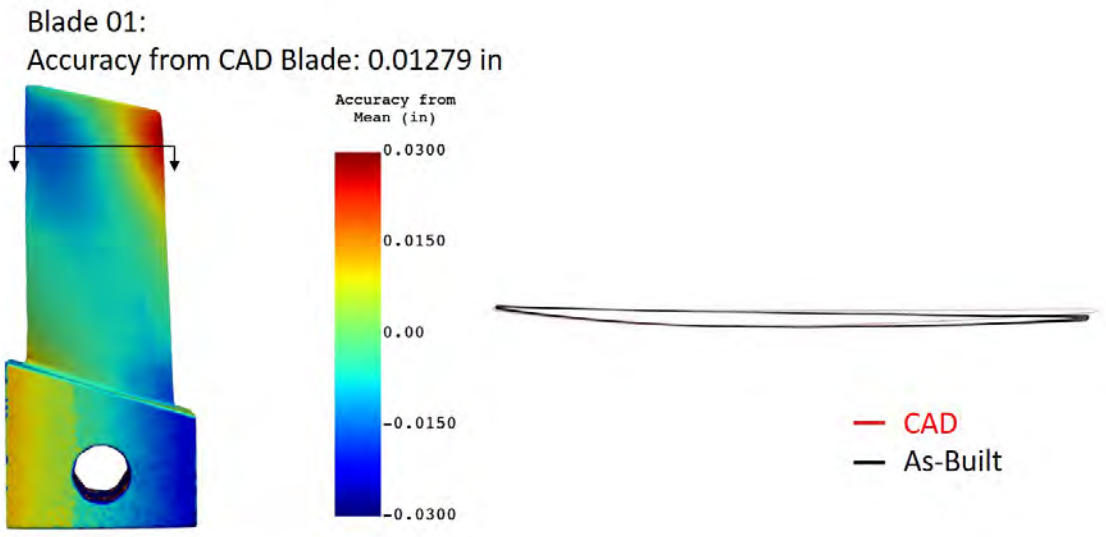

Figure 34. A) Heat map of the variations between the CAD file and Turbine Blade 01. Red denotes where the scanned geometry is above the CAD surface. Blue denotes where the scanned geometry is below the surface. B) Cross-section (top down view) of variation between the scanned surface geometry and the CAD file. The blade edges are slightly shorter and the blade surface tilts away on the right edge.

4.5 Fatigue Testing

Two different fatigue tests were run to verify the augmented El-Haddad model. The first is an axial tension-compression test applied to the fatigue bar specimen executed on an 810 MTS Load Frame with a 100kN Load Cell. The second fatigue test is a vibrational induced bending test with the turbine blades performed on an Unholtz-Dickie 20K Electrodynamic Shaker Table. The testing sets the maximum stress level seen by each sample, the fatigue life to failure, and by analyzing the fracture surface, the failure defect size and location. Combining the defect location

with the stress map for the part yields the stress experienced at the defect. The failure defect size, defect location stress, and fatigue life are all the data needed to determine if the augmented El-Haddad model is an accurate representation of finite fatigue life with respect to defects and if it can accurately predict where a failure will initiate.

4.5.1 Fatigue Bar Testing

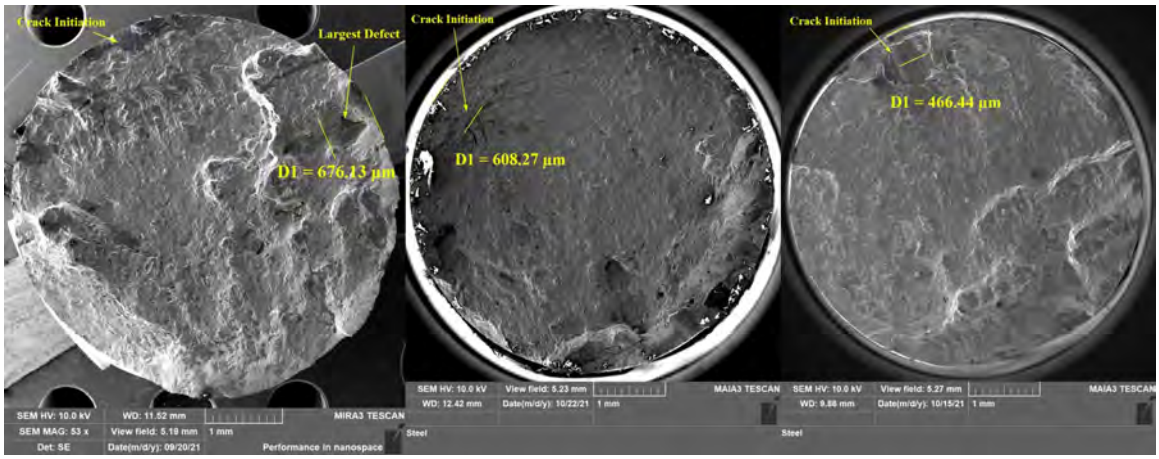

Figure 35. Fatigue bar fracture surfaces that potentially start from internal defects. A) Fatigue Bar 08, while a larger internal defect initiated one crack growth region, the dominate region grew from a surface defect. B) Fatigue Bar 09. C) Fatigue Bar 10.

The fifteen remaining fatigue bars were broken into three groups. Each group was tested at a different stress level and ran at 20 Hz until failure. Table 5 depicts the test results. Columns 2 and 3 are the data generated directly from the fatigue tests. To convert from σ_{max} to $\Delta\sigma$ for the augmented El-Haddad model, the maximum stress is multiplied by $(1-R)$, where R = -1. Column 4 is generated by analyzing the fracture surfaces under a Scanning Electron Microscope (SEM) to identify the initial failure defect sizes. On every fatigue bar, the failure defect is identified as a LoF defect on or near the specimen surface. With failure defects ranging in size from $236\mu m$ up to $656\mu m$, every fatigue bar failed to a large defect outside the 99.95 percentile of the assumed defect distribution depicted in figure 30. Defects $400\mu m$ or larger have

the probability of occurrence of once per fatigue bar based on the assumed defect distribution and total fatigue bar volume. Factoring in that the region of maximum stress is 28% of the total volume, it is expected that four to five of the fifteen fatigue bars should fail due to defects $\geq 400\mu m$. From Table 3, five of the fatigue bars were assessed to fail due to defects larger than $400\mu m$. In total, seven defects $\geq 400\mu m$ are visible across all the measured fracture surfaces. Fatigue Bars 07, 08, and 10 all contain defects over $400\mu m$ that did not initiate the fatal crack. Fatigue Bar 08 (Fig. 35A) contains two defects $\geq 400\mu m$ and grew from the smaller defect. The larger defect does not touch the surface and is assessed as an internal defect according to equation 7. The decrease in shape factor reduces the criticality of the larger defect. Fatigue Bar 10 (Fig. 35C) also contains two of these large defects and grew the fatal crack from the larger defect. Fatigue Bar 07 (Fig. 36C) grew from a much smaller defect ($248\mu m$). While the larger defect propagated a crack growth region, it is not clear why the smaller defect region grew faster and dominated the total crack growth.

The initiating defects for Fatigue Bars 09 and 10 (Fig. 35B & C) do not touch the edge of their bars. Applying equation 7 to the fatal defects yields values of 0.22 and 0.70 respectively, concluding that these defects may safely be classified as internal defects.

Fatigue Bars 02, 05, 07, 08, and 13 all appear to have multiple regions of independent crack growth (Fig. 36 & Fig. 35A). In every case of multiple crack growth regions, the failure defect is taken as the defect that initiated the largest crack growth region.

Column 5 of Table 3 is the stress experienced at each fracture surface. Measuring the diameter of the fatigue bar at the fracture surface allows the calculation of the stress experienced by the failure location. Figure 37 depicts the location of every fracture surface with respect to the fatigue bar dimensions. In every case the fracture

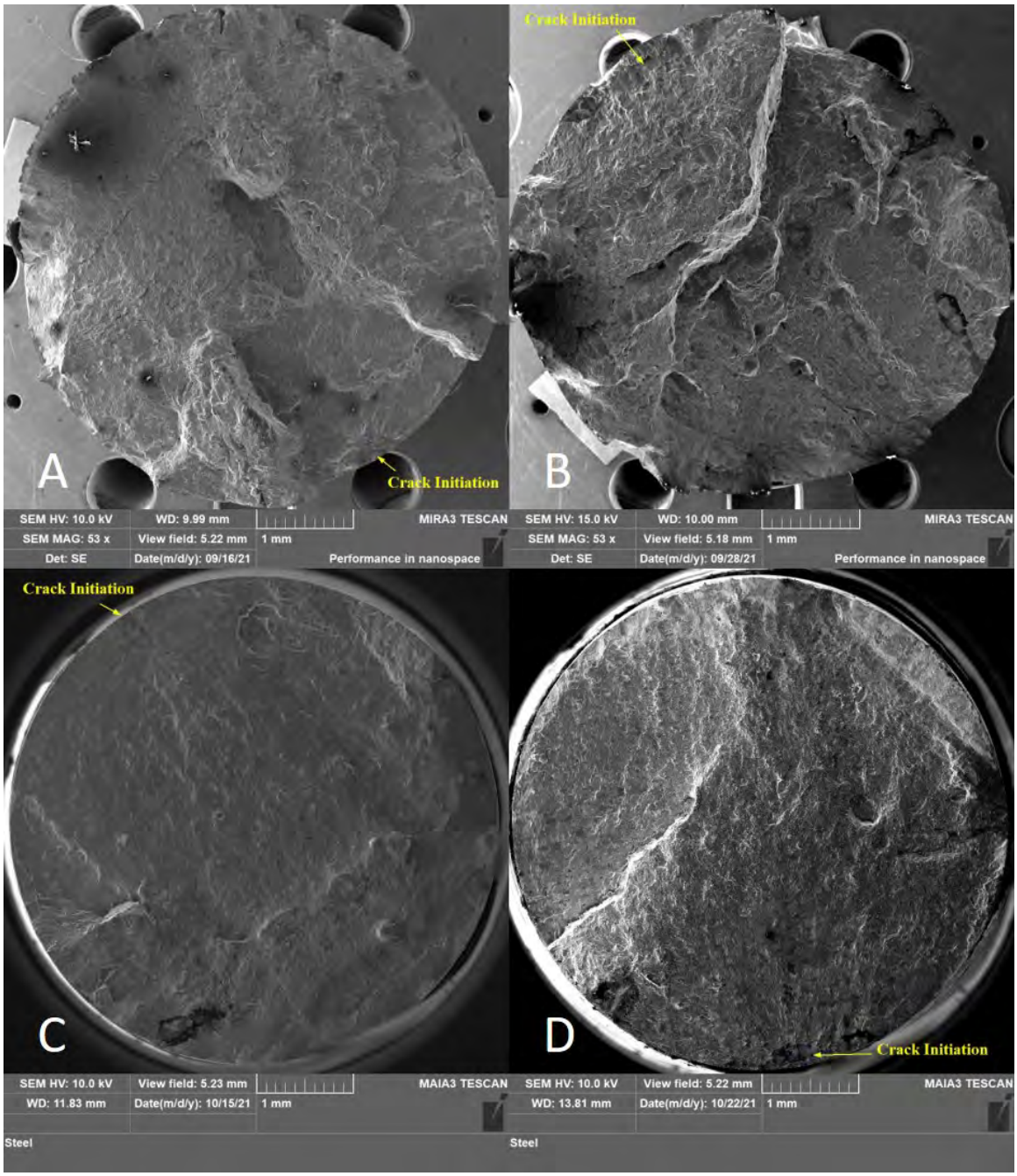

Figure 36. Fatigue bar fracture surfaces with multiple crack initiation points. Identified initiation points belong to the dominate crack growth region for each specimen. A) Fatigue Bar 02: contains four different crack growth regions. B) Fatigue Bar 05: contains two different crack growth regions. C) Fatigue Bar 07: contains two different crack growth regions. D) Fatigue Bar 13: contains two different crack growth regions.

surface is at or near the maximum applied stress. The largest deviation is Fatigue Bar 04, which is far enough into the flare to experience a stress at 93% of the maximum

Fatigue Bar	Applied σ_{Max} (MPa)	Fatigue Life (N)	Defect Size (μm)	Defect σ (MPa)
01	345	230,416	236	341
02	517	22,356	262	517
03	221	464,646	314	218
04	345	75,059	538	321
05	517	23,888	448	516
06	221	553,711	425	219
07	345	118,499	248	345
08	517	20,368	402	514
09	221	1,075,687	269 (I)	220
10	345	95,388	656 (I)	345
12	517	23,776	370	514
13	221	541,165	261	217
15	345	134,758	355	335
16	517	23,250	330	517
17	221	5,883,002	351	220

Table 5. Fatigue bars subject to axial fatigue testing and fractography. The (I) next to Defect Size denotes that the defect is an internal defect.

applied stress. Fatigue Bar 04 is an example of an extremely large defect at a lower stress location that dictates the final failure.

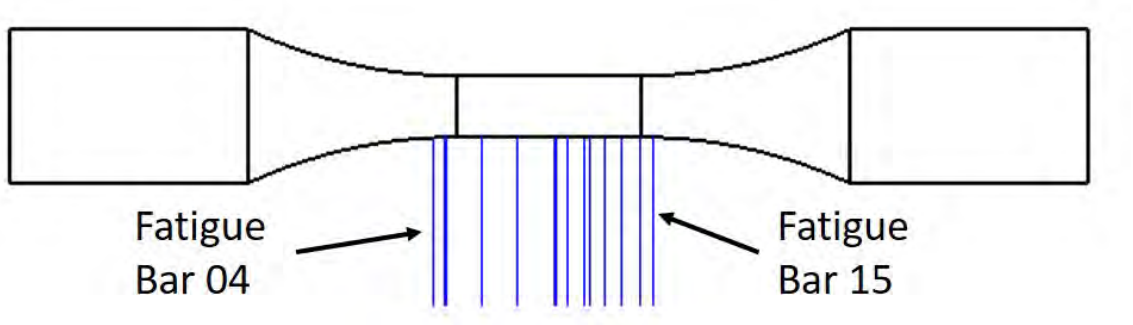

Figure 37. Failure locations for every fatigue bar test. While the majority fail within the specimen neck, a small group fail in the flare with Fatigue Bars 04 and 15 being the farthest out on each end.

The application of columns 4 and 5 of Table 5 to the augmented El-Haddad model enables a predictive fatigue life that may be compared to the experimental fatigue life from column 3 to assess the quality of the model to capture the relationship between

defect size, applied stress, and fatigue life.

4.5.2 Turbine Blade Testing

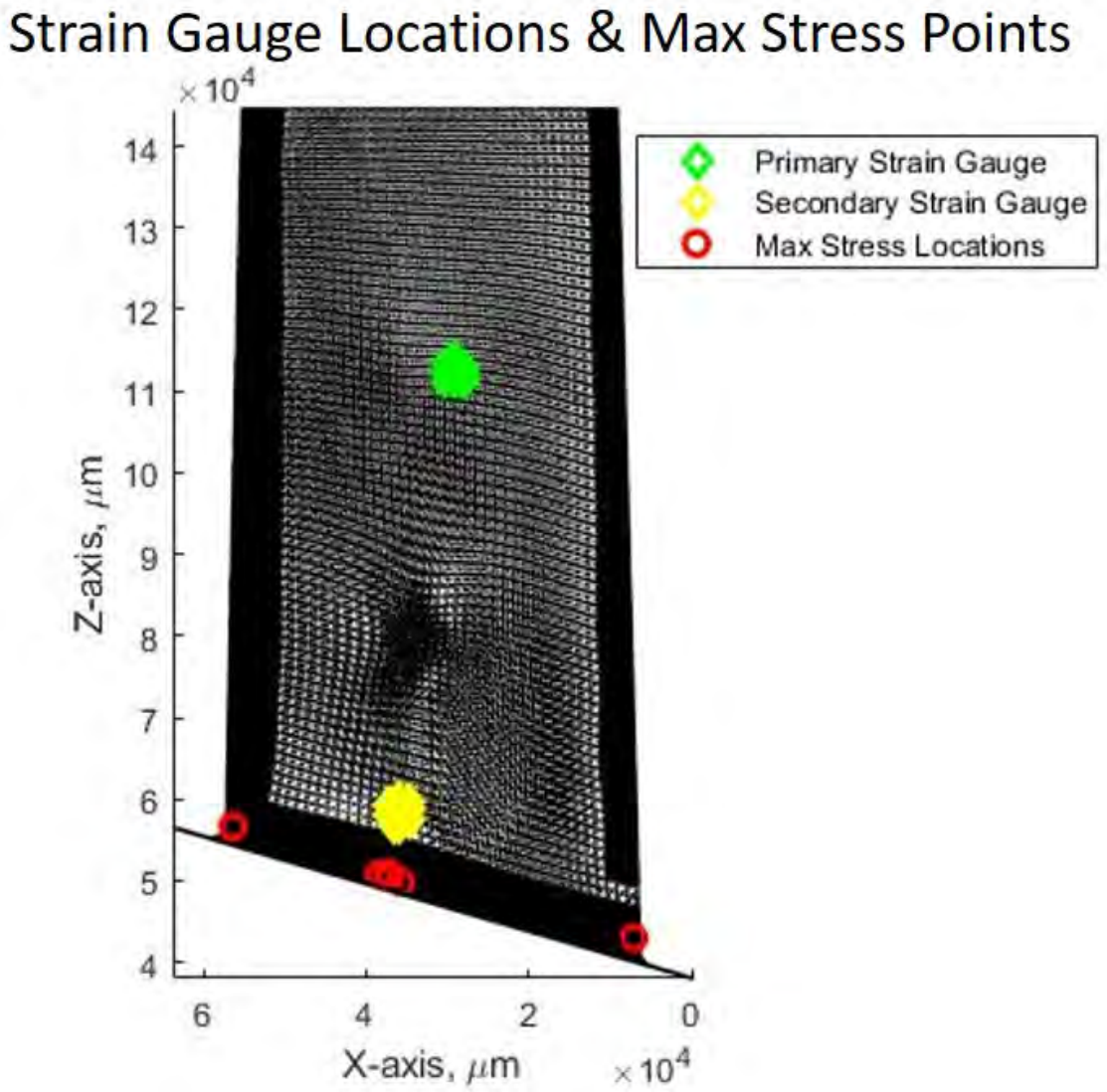

Figure 38. Locations of the primary and secondary strain gauges. Gauges attached to the same locations for every turbine blade. The position of the maximum stress point for each unique FEM.

The turbine blade testing is a more involved process to control the applied stress. A Polytec OFV 500 Laser Vibrometer measures the peak blade velocity at one point on each blade during testing. Two strain gauges, for redundancy, are applied along

the length of the blade to measure the axial strain (Fig. 38). Application of a strain gauge at the point of maximum stress is not feasible due to the geometry of the turbine blade. Instead filtering techniques identify two gauge locations where the FEM strain value has a range of less than $1e^{-4}mm/mm$ across a 2mm radius and that the average strain within the 2mm radius is within 1% of the maximum strain in the region. The filtering criteria ensure that the strain measurements represent the expected peak strain at their locations. The applied strain gauges are 1.6mm across ensuring that any minor variation in gauge placement does not influence the accuracy of relating the measurement values to the FEMs. The primary strain gauge is co-located with the maximum stress associated with the second bending mode (Fig. 29B). Using the linear relationship between the measured peak velocity and the strain gauge measurements [92], the stress and strain at the gauge locations are controlled by setting the peak measured velocity in a closed feedback loop in the 20K electrodynamic shaker table. From each turbine blade's unique FEM, the relationship between maximum stress/strain and stress/strain at the gauge locations are calculated. While the exact ratio changes for each turbine blade FEM, on average the primary gauge measures 44.3% of the maximum strain with a standard deviation of 2%. By extension the same ratio applies to the maximum stress. Applying the transforms of laser vibrometer peak velocity to strain gauge measurement, strain to stress at the strain gauge location, and measured stress to peak stress fully defines the system to control the maximum stress from the peak velocity.

The point of maximum stress for every turbine blade is along the root where the blade meets the grip (Fig. 38). The maximum stress location varies between each turbine blade due to small geometric variations. The ten turbine blade FEMs predict three primary regions where the maximum stress appears: left, right, and center of blade on the convex side near the root. Due to the unique geometry of each turbine

blade FEM, even blades that trend to similar peak stress locations have some regional variation. Five of the ten turbine blades have their maximum stress point along the center. Turbine Blades 03 and 08 have their maximum stress points on the right edge of the blade and Turbine Blades 01, 05, and 07 all have their maximum points on the left edge of the blade. While the global maximum stress point varies due to the geometric variations between the turbine blades, the three identified regions are local maximum stress points for every blade (Fig. 29B).

The turbine blade fatigue testing applies the stress step function test (Eq. 18) [92, 93]. A desired fatigue life is selected for the test, N_t, specified in Table 6. The sample is cycled at an initial peak stress level until N_t is reached, then the stress is stepped up by an incremental value. For the testing here, the incremental value is 34.5 MPa (5 ksi). The fatigue stress level, σ_a, is the linear interpolation between the last stress level that reaches N_t cycles, σ_{pr}, and the stress level that causes failure, σ_f based on the percentage of completion for the final step, $\frac{N_f}{N_t}$, where N_f is the number of cycles ran in the final step.

$$\sigma_a = \sigma_{pr} + \frac{N_f}{N_t}(\sigma_f - \sigma_{pr}) \tag{18}$$

The results of the fatigue testing for each turbine blade are found in Table 6. The fatigue testing of the turbine blades reached the limits of the vibration table without growing any of the cracks to full separation. Applying a Fluorescent Penetrate Inspection (FPI) to each blade surface revealed the location and width of each crack (Fig. 39). With the exceptions of Blade 01 and Blade 08, the cracks initiated in locations near the center of the blade root. In Blade 03, the crack initiated at the left edge of the blade, far from the Blade 03 global peak stress. In Blade 08, the crack initiated along the right edge in close proximity to its global peak stress. After growing the cracks, the blades were separated to expose the full fracture surface by applying

notches as the crack tips. During the separation process, the failure initiation point for Blade 08 was mistakenly destroyed.

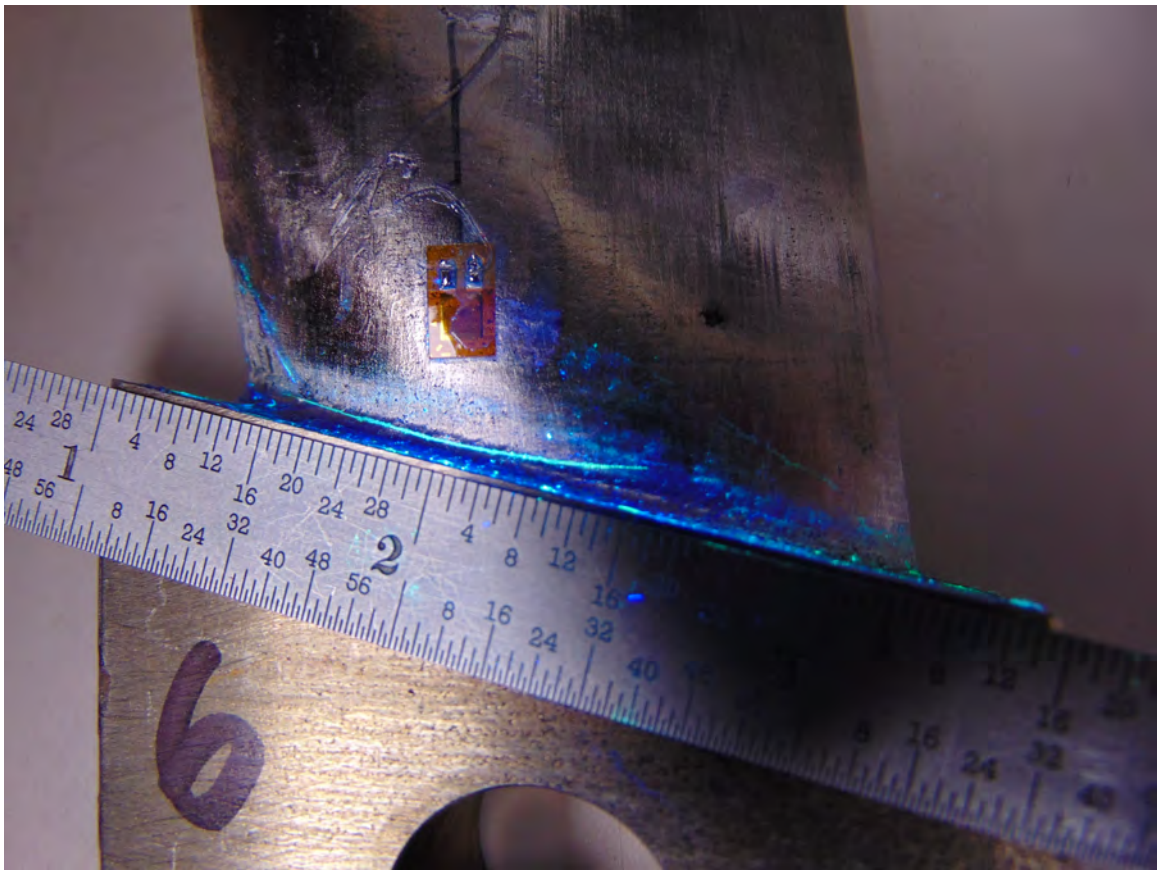

Figure 39. FPI of Turbine Blade 06. Measurements indicate that the crack front is approximately 27mm long and started near the center of the blade root.

Fractography on the blade crack growth surfaces provides the critical defect size (Table 6, column 4) and location that appears to initiate crack growth for each turbine blade. Unlike the fatigue bars where LoF defects caused every failure, two of the turbine blades (Blades 01 and 04) failed due to notches on the surface associated with surface roughness. The other blade failure defects are LoF defects. The failure defects for Blades 02 and 05 do not touch the surface, applying equation 7 yields values of 0.15 and 0.32 respectively, classifying those defects as internal. Applying the measured defect locations back to the FEM for each blade generates the ratio between maximum stress and defect location stress to generate column 5. The calculated stress

at the defect locations range from 53% to 72% of the maximum stress.

Blade ID	Applied σ_{Max} (MPa)	Fatigue Life (N)	Defect Size (μm)	Defect Type	Defect σ (MPa)
01	587	10^6	19	Notch (Surface)	409
02	463	5×10^5	41	LoF (Internal)	337
03	679	10^6	195	LoF (Surface)	462
04	330	10^7	23	Notch (Surface)	237
05	722	10^5	44	LoF (Internal)	492
06	376	5×10^6	207	LoF (Surface)	203
07	486	5×10^6	60	LoF (Surface)	308
08	440	10^7	-	-	-
09	517	5×10^5	116	LoF (Surface)	366
10	732	10^5	33	LoF (Surface)	439

Table 6. Turbine blades subject to vibration induced bending fatigue tests and fractography.

4.6 Experimental Validation

Applying the measured defects sizes and the defect stresses from tables 5 and 6 into the El-Haddad model predicts life values. The predicted life for each specimen is compared to the measured fatigue lives to generate figure 40. The predicted versus measured fatigue life plot informs on the quality of the augmented El-Haddad model against the experimental data sets. Applying the measured defect locations for each turbine blade to their unique FEMs with the experimental fatigue life evaluates the ability of the augmented El-Haddad model to predict critical failure locations.

4.6.1 Fatigue Life Evaluation

The fatigue bar data trends very well with the augmented El-Haddad model that was trained from prior testing [11]. Only three of the fifteen specimen (Fatigue Bars 09, 10, and 17) tested more than twice as long as the model predicted (Fig. 40). Fatigue Bars 09 and 10 failed due to an internal defect instead of a surface defect.

The model assumes a surface defect which has a higher shape factor, Y, and is therefore conservative when an internal defect becomes the root cause of error. When the model is adjusted to account for an internal defect both data points fall within the 2x bands. The final fatigue bar specimen that that model under predicts the fatigue life is Fatigue Bar 17, which lasted 16.4 times longer than the model prediction. It is unclear at this time why Fatigue Bar 17 lasted so much longer than the rest of the set. The remaining fourteen fatigue bars have a mean ratio of measured life over predicted life of 1.54 ± 0.59. With the material properties built into the El-Haddad model, the fatigue bar data demonstrates a slightly conservative trend in the model prediction while keeping very accurate results.

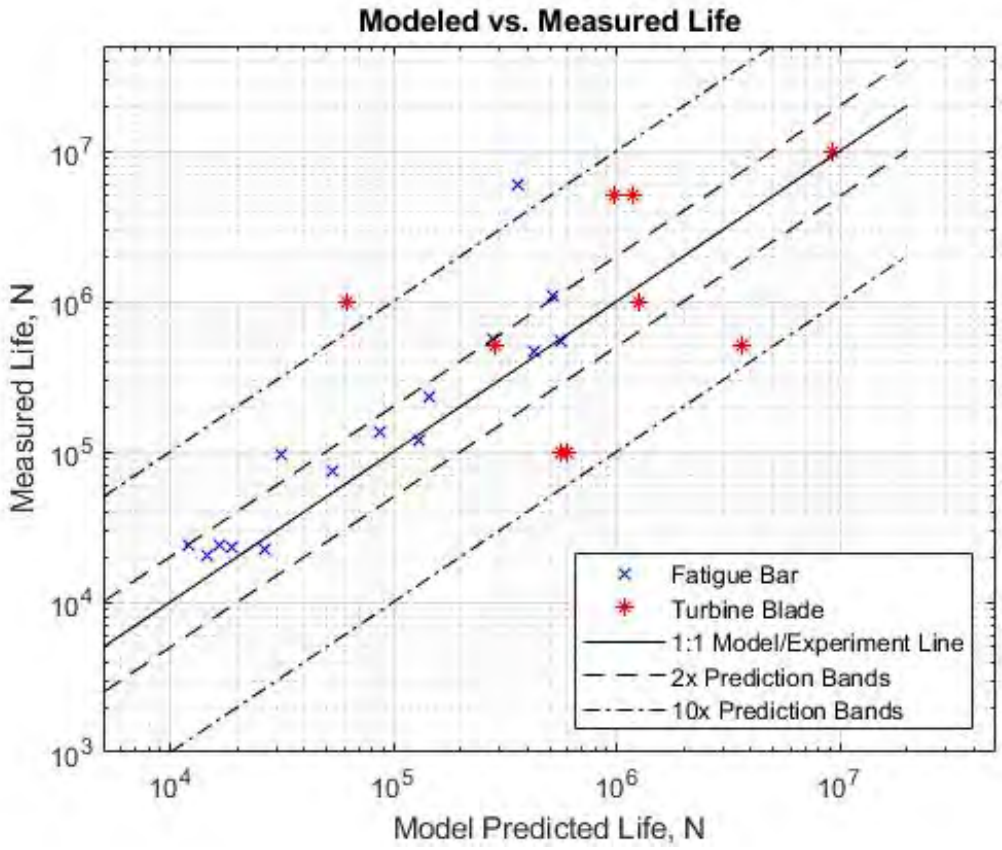

Figure 40. Measured fatigue life of the axially loaded fatigue bars and the bending loaded turbine blades versus the augmented El-Haddad model predictions based on the measured fatal defect size and location.

The turbine blade data demonstrates the same trend as the fatigue bars with an increase in the scatter. Evaluating all nine turbine blade data points has a mean ratio of 3.30 ± 5.15 for the measured life over the predicted life.

Turbine Blade 03 has the largest variation between the model prediction and the experimental data at a ratio of 16.1. This specimen is one of the two unique cases where the crack grew from the edge of the blade instead of the center. The edge growth means that the crack crosses the blade at a very early stage and that it is only attached to the main body on one side. The critical defect associated with Blade 03 is also smoother than any of the defects seen on the other fracture surfaces implying that there was additional friction between the fracture surfaces not seen in any of the other specimen. The smoother surface makes identification of the initial size harder to measure. As a result, anything that might be part of the original defect is factored into the reported defect size in Table 6 creating an over-estimation of the defect size being processed through the augmented El-Haddad model. There is also a strong possibility that the extra degree of freedom imparted by having half of the crack surface free of any applied loads or constraints absorbs some of the applied energy and further inhibits the crack growth.

Removing Turbine Blade 03 from the set due to the unique nature of failure, the remaining eight blades have a mean of 1.69 ± 1.96. In either case, there is insufficient data to reject the hypothesis that both the fatigue bars and turbine blades use the same trend line.

Figure 41 depicts all of the test specimen against the El-Haddad model. There is a clear separation in failure defect sizes between the fatigue bars and turbine blades despite being printed on the same build plate. Every fatigue bar contains sufficiently large defects to have the fatigue life dominated by LEFM. In contrast, the turbine blades failed due to smaller defects and responded closer to the material fatigue limit,

creating a mixture of the two failure mechanisms.

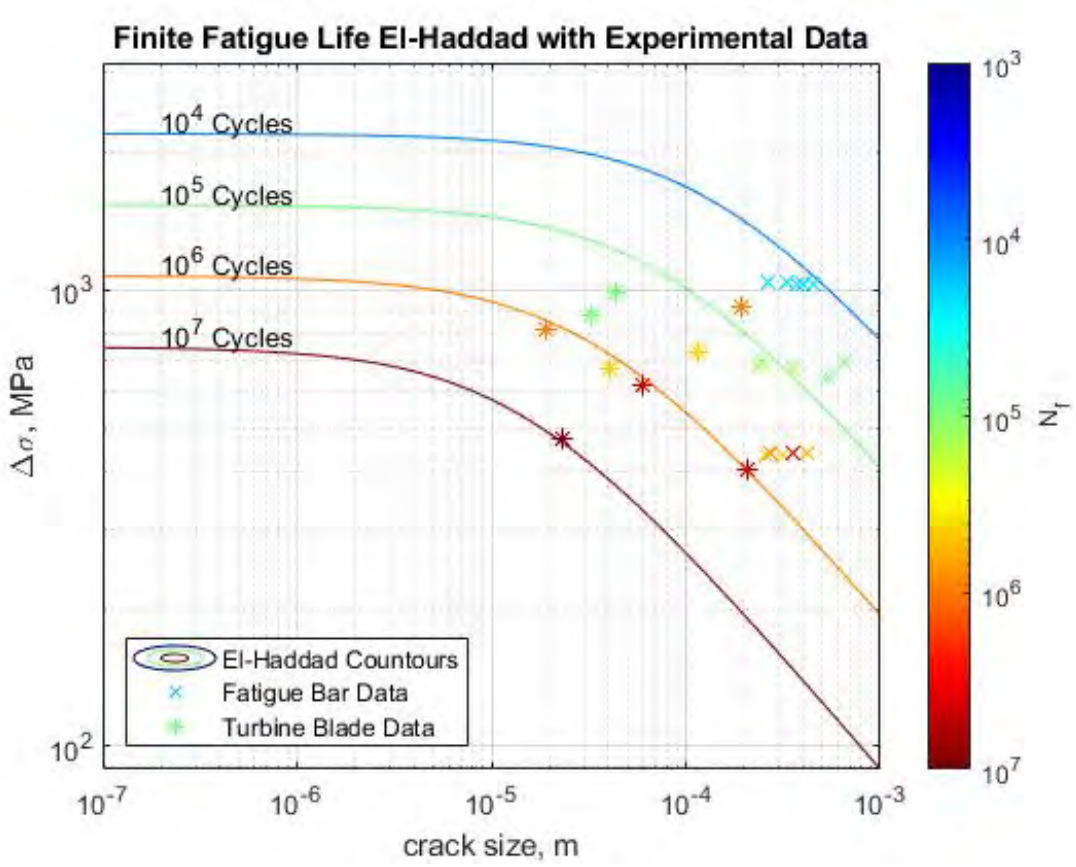

Figure 41. Fatigue bar and turbine blade experimental data on the augmented El-Haddad model.

4.6.2 Critical Failure Evaluation

Evaluating the critical failure locations looks at a single design life and a maximum defect size in conjunction with the augmented El-Haddad model and FEM. Figure 42 outlines the steps required to generate the critical failure locations on any component. This research built and tested a number of specimen and verified that the initial finite life El-Haddad model creates an accurate representation of the relationship between defect size, location, and desired life. For the expected maximum defect size, the best practice is to generate a defect distribution to inform on the maximum defect size of interest. In this section maximum defect sizes are identified based on the measured

failure defects in the turbine blades to explore the accuracy of the identified critical failure locations. The desired design life for each turbine blade is the tested fatigue life value (Table 6). Finally, the minimum stress level for each choice of design life and defect size is combined with the blade unique FEMs to identify every location that could initiate failure. In every case here, the measured failure locations fall within the predicted failure locations.

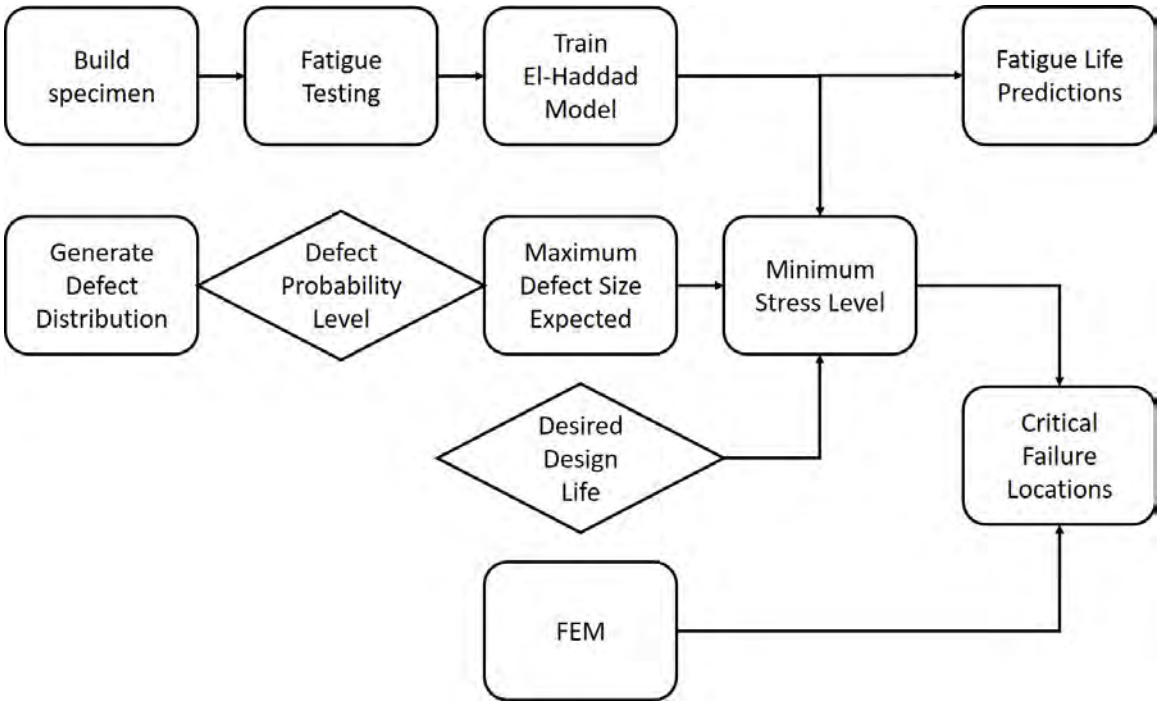

Figure 42. Flow chart to generate predictions of fatigue life and critical failure locations.

For Turbine Blades 01 and 03 with a fatigue life of 10^6 cycles, the largest failure defect is measured at $195\mu m$ on Turbine Blade 03. Figure 43 looks closely at Turbine Blade 03 with respect to the choice of maximum defect size when determining the critical failure locations. Figure 43A shows the predicted failure areas where a defect $\leq 50\mu m$ has the potential to grow into a fatal crack. The measured location for the $195\mu m$ defect is just outside of the identified region at the left edge. When the evaluation maximum defect size is increased to $200\mu m$ (Fig. 43B), the predicted area of crack growth expands to include the identified failure location.

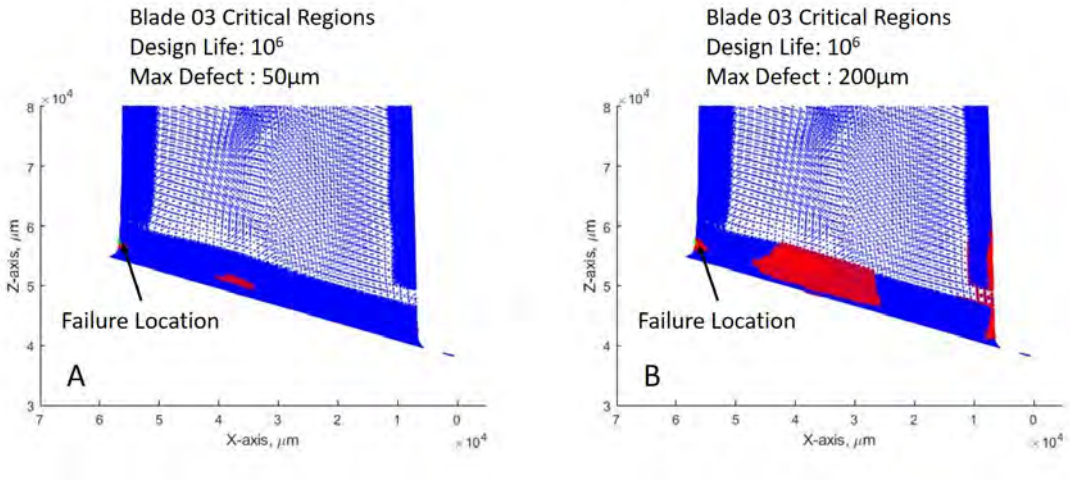

Figure 43. Critical failure locations for Turbine Blade 03 assuming A) A defect $\leq 50\mu m$ causes failure and B) A defect $\leq 200\mu m$ causes failure

The predicted critical failure locations for Turbine Blades 05 and 10 (Fig. 44) are depicted for the case of 10^5 cycles fatigue life and a failure-inducing defect $\leq 50\mu m$. Both turbine blades fail due to defects smaller than $50\mu m$, and in both cases the measured defect location falls within the predicted failure location along the center of the blade.

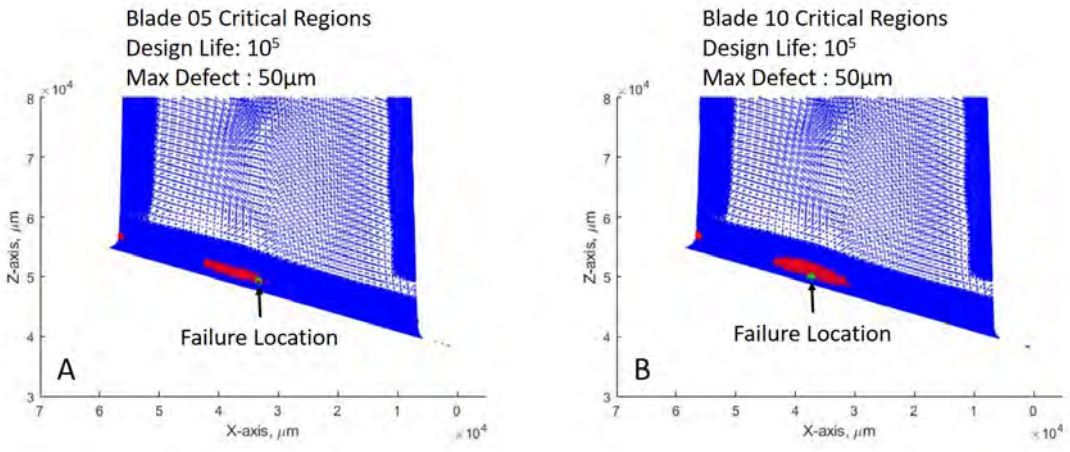

Figure 44. Critical failure locations for A) Turbine Blade 05 and B) Turbine Blade 10. In both cases the identified failure defect falls within the bounds predicted by the augmented El-Haddad model.

4.7 Summary Remarks

This research expands the finite fatigue life El-Haddad model by augmenting the analytical model with an FEM. The combination emphasizes the importance of accounting for the defect location in conjunction with the defect size. The augmented El-Haddad model demonstrates the ability to accurately predict the fatigue life for both axial and vibrationally loaded specimen. Here the values for defect size and stress are measured from the fracture surface to minimize the uncertainties in the defect that causes failure. However, the model does not require that to generate a fatigue life prediction. Any technique to generate a defect size and location, when coupled with an FEM will generate the parameters required to make a fatigue life prediction. Other techniques that could be used to make a fatigue life prediction are: surface penetrating scans (ex: X-ray scans), defect estimations from process monitoring during a print (ex: in-situ data collections), or stochastic evaluations from a known or assumed defect population.

The model is also shown to accurately predict where failure can start from for a design life and defect size. By linking the augmented El-Haddad model with an FEM load case, maximum expected defect, and desired component life, the model predicts sections of the component where failure can initiate. From an inspection view, the capability to minimize the search region for root causes of failure saves time and money. By developing a better understanding of potential defect sizes and location based on AM printer settings and materials, this feature of the augmented El-Haddad model will become even more accurate and move the research toward the certification of AM components for the aerospace industry.

V. Validation of El-Haddad Model

5.1 Overview

By combining the traditional S-N curve for a material and the El-Haddad model that defines a constant life curve based on applied stress and defect size [22], a response surface is created relating defect size, applied stress, and expected life. Selecting two of the values either through design criteria or experimental data gives a model prediction for the third value. This paper demonstrates the validation process for the developed model against both uni-axial tension-compression tests on standard fatigue bars (ASTM-E466) and vibrational bending tests on a simple turbine blade design.

5.2 Background

Applying the calculation of the critical crack length (a_0) according to Equation 12 and applying the stress range for the same life from the material S-N curve for $\Delta\sigma_{0,N}$ using the material properties from Table 1 generated a finite fatigue life El-Haddad curve that predicted how the maximum defect size and applied maximum stress impact the ability to hit a target life (Fig. 45). By identifying two of the three parameters (defect size, maximum applied stress, and design life), the augmented model predicted what the third value should be. Uni-axial stress tests demonstrated that the updated model generates a good prediction of boundary for any desired life [11]. This version of the El-Haddad model still contained the underlying assumption that failure would occur at the maximum stress location.

To enable defect location dependencies in the finite fatigue life El-Haddad model, it was combined with a Finite Element Model (FEM). The FEM mapped out the stress distribution for a given load case and demonstrated that crack initiation may occur at locations other than the peak stress point [77]. Under the uni-axial loading

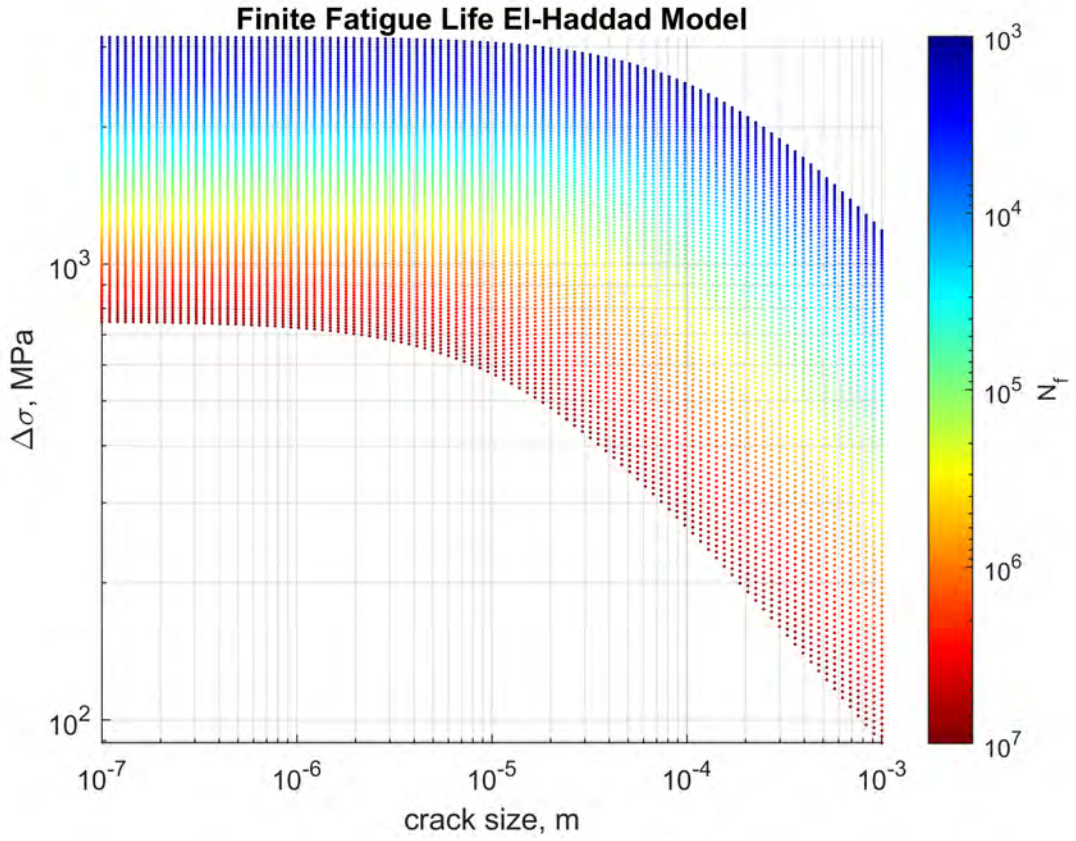

Figure 45. Finite fatigue life El-Haddad model. Design lives plotted from 10^7 cycles down to 10^3 cycles.

condition where the stress state was consistent across a relatively large volume, it was reasonable to expect the largest defects to appear inside the region of maximum stress. When the stress profile was not uniform, such as with complex bending loads, the peak stress region became a very small percentage of the total material volume, significantly lowering the probability that a large defect existed at the peak stress location. Research with the FEM augmented El-Haddad model enabled predictions of where failure was most likely to initiate based on the stress map and an assumed defect population [77].

The importance of where a defect appears was found throughout literature. In 3-point bending experiments, cases of component failure due to defects not in the maximum stress region have been seen [78]. In addition, the relative position of

defects to the surface, shape ratios, and orientation have been identified as causes of experimental variations that impacted how quickly a defect caused failure [94].

5.3 Experimental Processing

Ten turbine blades (Fig. 46A) and eighteen cylinders were additively manufactured from nickel-based superalloy 718. The cylinders were machined down to fatigue bars according to ASTM E466 (Fig. 46B) [12]. The specimens were all post processed by a stress relief of 1000°C for one hour, age hardened according to AMS-2774-G [91] (718°C for 8 hours, furnace cooled to 621°C and held for eight hours, then air cooled). The printed blade surfaces were ground smooth to an average S_a of 3.2 ± 0.8 to minimize the impacts of surface roughness.

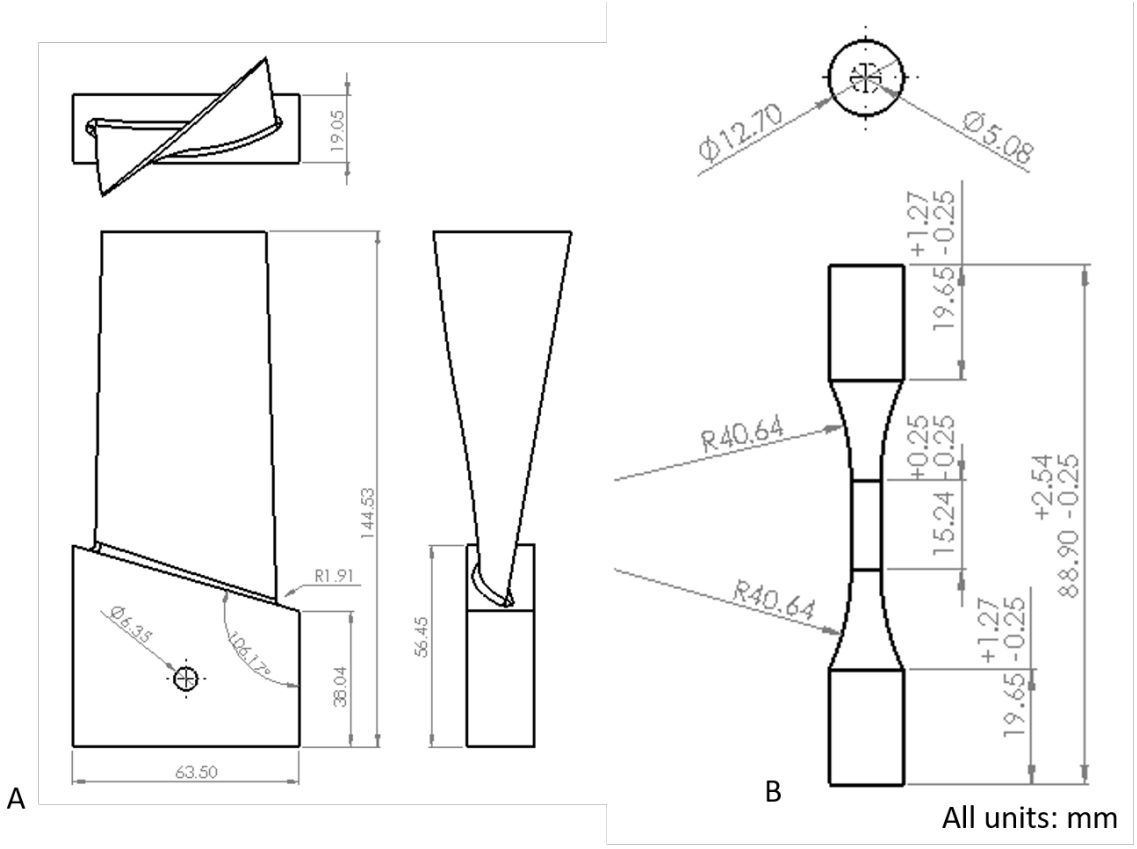

Figure 46. A) Turbine blade geometry. B) Fatigue bar geometry.

5.3.1 Fatigue Bar Testing

Three of the fatigue bars were selected to measure the final material properties from the build plate. Mass and volume measurements yielded an average density of 8.19 g/cm^3 with a standard deviation of 0.032 g/cm^3. The three specimens were also subjected to monotonic tensile testing on an 810 MTS Load Frame with a 100kN Load Cell, and instrumented with an MTS axial extensiometer (model #634.12E-24) with spring clip attachments. The test generated an average Young's Modulus value of 159.1 GPa with a standard deviation of 4.1 GPa. The remaining fifteen fatigue bars were separated into three groups and subjected to fully reversed ($R = -1$), uni-axial fatigue life testing (Table 7). Each group was tested on the same MTS load frame at the maximum stress range values of 441.3, 689.5, and 1034.3 MPa respectively. The testing frequency was set to 20 Hz until fatigue failure occurred.

	Experimental Life (N)	Applied $\Delta\sigma_{max}$ (MPa)
Fatigue Bar 01	230,416	689.5
Fatigue Bar 02	22,356	1034.3
Fatigue Bar 03	464,646	441.3
Fatigue Bar 04	75,059	689.5
Fatigue Bar 05	23,888	1034.3
Fatigue Bar 06	553,711	441.3
Fatigue Bar 07	118,499	689.5
Fatigue Bar 08	20,368	1034.3
Fatigue Bar 09	1,075,687	441.3
Fatigue Bar 10	95,388	689.5
Fatigue Bar 12	23,776	1034.3
Fatigue Bar 13	541,165	441.3
Fatigue Bar 15	13,4758	689.5
Fatigue Bar 16	23,250	1034.3
Fatigue Bar 17	5,883,002	441.3

Table 7. Experimental results from the fatigue bar testing

5.3.2 FEM Development

Using Abaqus 6.14, two FEM model types were developed. The first FEM used the nominal Computer Aided Design (CAD) model to generate the blade geometry (Fig. 47A). This model created a single stress/strain map across the nominal blade geometry and was applied to each of the turbine blade samples. The second FEM applied structured-light surface scans using the Advanced Topology Optimalogy System (ATOS) to generate a geometrically accurate surface map of each turbine blade after all of the post-processing steps were completed. The ATOS surface maps morphed the CAD based FEM to create a digital replica FEM for each printed turbine blade, generating unique stress/strain maps.

Each FEM was analyzed using dynamic frequency analysis. The analysis generated the first five mode shapes, and stress/strain values across the blade surface normalized to a maximum displacement of one unit distance.

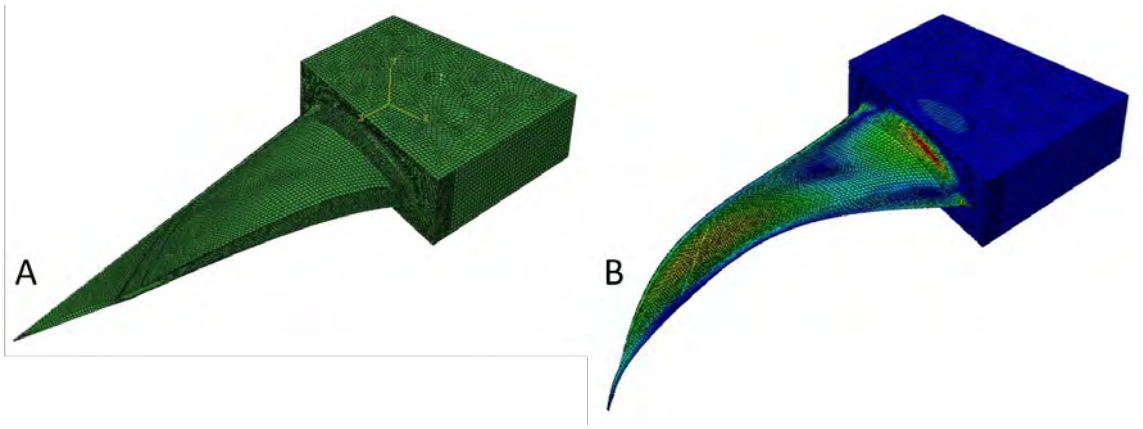

Figure 47. A) CAD based FEM of the turbine blade design. B) Turbine blade second bending mode.

5.3.3 Turbine Blade Testing

The AM turbine blades were tested using an Unholtz-Dickie 20K Electrodynamic Shaker Table and the fatigue life step method [92, 93]. The grip of the blade was

firmly clamped, and the blades were vibrated at their second natural frequencies of approximately 1460 Hz. Two strain gauges attached to the blade surfaces captured the experimental strain values. A Polytec OFV 500 Laser Vibrometer measured the peak blade velocity at a third point on each blade during testing. The laser vibrometer data held a linear relationship with the strain gauge measurements. By scaling the FEM stress/strain maps with the measured strain gauge values, a direct relationship between blade translation speed from the laser vibrometer and maximum applied stress to each turbine blade was developed. This process enabled a feedback control loop to set the maximum stress at each fatigue life step [77].

		Basquin Scaling	Strain Gauge Scaling	
	Experimental Life (N)	All FEMs Basquin $\Delta\sigma_{max}$ (MPa)	CAD FEM Exp. $\Delta\sigma_{max}$ (MPa)	Digital Replica FEM Exp. $\Delta\sigma_{max}$ (MPa)
Blade 01	1×10^6	1.075×10^3	1.158×10^3	1.174×10^3
Blade 02	5×10^5	1.197×10^3	1.003×10^3	9.260×10^2
Blade 03	1×10^6	1.075×10^3	1.303×10^3	1.358×10^3
Blade 04	1×10^7	7.506×10^2	6.958×10^2	6.603×10^2
Blade 05	1×10^5	1.538×10^3	1.431×10^3	1.443×10^3
Blade 06	5×10^6	8.362×10^2	7.793×10^2	7.521×10^2
Blade 07	5×10^6	8.362×10^2	9.179×10^2	9.714×10^2
Blade 08	1×10^7	7.506×10^2	6.761×10^2	8.793×10^2
Blade 09	5×10^5	1.197×10^3	1.068×10^3	1.034×10^3
Blade 10	1×10^5	1.538×10^3	1.523×10^3	1.464×10^3

Table 8. Computational and experimental maximum $\Delta\sigma$ values for each turbine blade based on the design life or the applied FEM.

Two different methods were applied to scale the FEM stress values from the displacement normalized values to actual values. The first method applied the Basquin Equation (Eq. 1) with the specimen design life to calculate the maximum applied stress range for the test specimen. Both the CAD based FEM and the digital replica FEMs were scaled by the ratio of the Basquin predicted maximum stress range over the FEM nominal maximum stress range. The second method to scale the FEM

stress values applied measured strain gauge values. The ratio between the attached strain gauges and the corresponding nominal strain values from the FEMs generated the scaling value to adjust the FEM stress maps. Table 8 annotates the maximum stress range on each turbine blade from each method. The strain gauge scaling all ranged within ±30% of the Basquin predicted maximum stress ranges. The corrected geometry of the digital replicas varied the maximum stress ranges within 10% of the CAD based FEM predictions.

While the geometric differences associated with the digital replicas did not create a large difference in the predicted maximum stress values from the CAD based model, there was a large difference in the maximum stress locations from the different models (Fig. 48). The maximum stress locations for Turbine Blades 01, 05, and 07 stayed near the leading edge with the global maximum stress point from the CAD based FEM. The digital replica FEMs for Turbine Blades 03 and 08 predicted the global maximum stress point to shift to the trailing edge of the blade. The remaining five turbine blade digital replica models predicted the maximum stress point along the center of the blade. The variations in the maximum stress location imply that the stress magnitudes also vary significantly between the CAD based FEM and the digital replica FEMs.

5.4 Defect Analysis

After testing, each fracture surface was analyzed on a Tescan Mira3 Scanning Electron Microscope (SEM). Crack growth tracing of the fracture surfaces identified the the defect that initiated the fatal fracture. From the SEM images, the fatal defect sizes and locations were identified. The area of each defect was determined by the SEM measurement software, which calculated an area based on the user defined defect boundary. The applied defect size, a, in Equation 15 was calculated from Equation

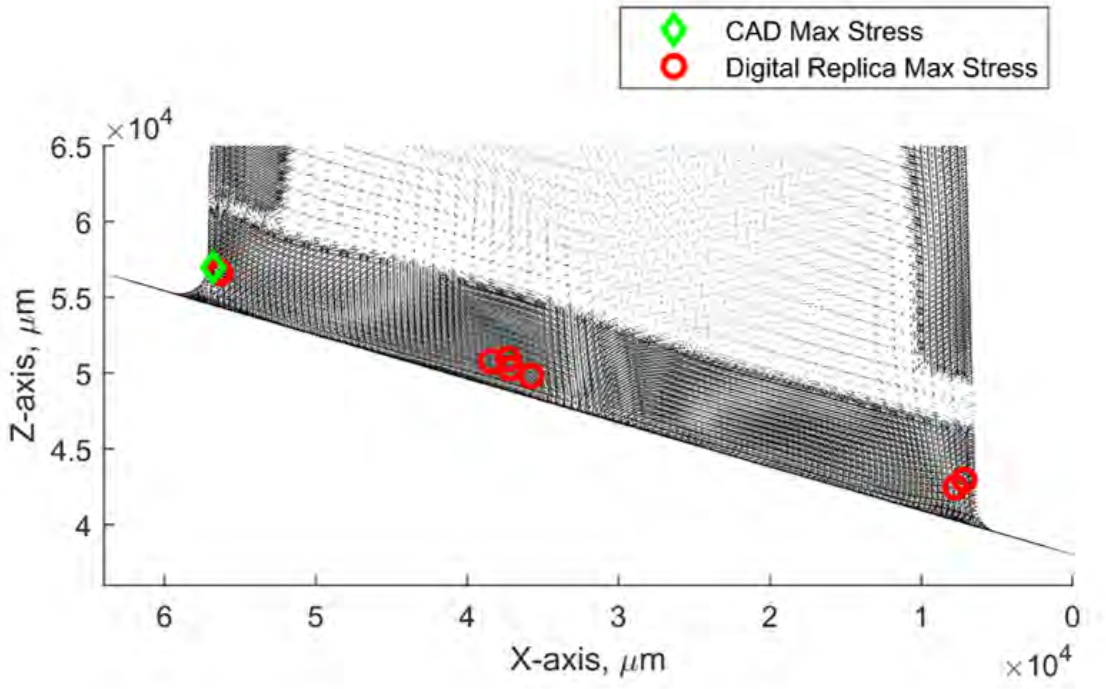

Figure 48. Maximums stress locations for the CAD based FEM (green diamond) and each digital replica FEM (red circles).

19.

$$a = \sqrt{area} \tag{19}$$

For the fatigue bars, the stress at the defect location was calculated from the applied force to the specimen and the cross-sectional area measured at the fracture plane. Applying defect size, experienced stress, and location relative to the surface into the finite fatigue life El-Haddad model generated fatigue life predictions (Table 9). Comparing the predicted life values in Table 9 to the experimental life values from Table 7, fourteen of the fifteen sample predictions were within 2x of the experimental data. Fatigue Bar 17 was the only anomaly where the predicted life was 16.4x lower than the experimental life. Analysis after the testing showed slip events during the testing, which invalidated that test result.

	Size (μm)	Defect $\Delta\sigma$ (MPa)	Surface Defect	Predicted Life (N)
Fatigue Bar 01	236	682.8	Yes	1.438×10^5
Fatigue Bar 02	262	1038.6	Yes	2.634×10^4
Fatigue Bar 03	314	436.7	Yes	4.285×10^5
Fatigue Bar 04	538	648.4	Yes	5.337×10^4
Fatigue Bar 05	448	1031.7	Yes	1.206×10^4
Fatigue Bar 06	425	438.4	Yes	2.762×10^5
Fatigue Bar 07	248	691.0	Yes	1.289×10^5
Fatigue Bar 08	402	1028.4	Yes	1.454×10^4
Fatigue Bar 09	269	440.6	No	2.075×10^6
Fatigue Bar 10	656	691.1	No	1.235×10^5
Fatigue Bar 12	370	1027.1	Yes	1.662×10^4
Fatigue Bar 13	261	433.5	Yes	5.675×10^5
Fatigue Bar 15	355	670.5	Yes	8.693×10^4
Fatigue Bar 16	330	1037.4	Yes	1.896×10^4
Fatigue Bar 17	351	440.0	Yes	3.578×10^5

Table 9. Model parameters of defect size, stress, surface location, and predicted life for the fatigue bar specimens.

For the turbine blades, the defect locations measured from the SEM imagery were applied to their appropriate digital replica FEM to find the stress value at the defect locations scaled according to the strain gauge measurements. A total of 432 defects were imaged across the ten turbine blade fracture surfaces. Table 10 describes the model parameters of defect size, stress, location relative to the surface, and predicted fatigue life for four different defect attributes. The first attribute is the defect that initiated crack growth as identified through the crack growth tracing. The other three attributes are shortest predicted life on each turbine blade, largest measured defect on each turbine blade, and the defect on each turbine blade that experienced the largest stress range. Across all ten specimens, in no case did the largest defect generate the shortest life prediction, and only four specimens predicted the defect at the highest stress value leading to the shortest predicted life. These results correlated well with the simulation results from prior work with the finite fatigue life El-Haddad model where 4% of cases predicted initial failure due to the largest defect and 30% of cases

predicted initial failure due to a defect at the maximum stress point [77].

	Failure Initiating Defect				Shortest Predicted Life			
	Size (μm)	Applied $\Delta\sigma$ (MPa)	Surface Defect	Predicted Life (N)	Size (μm)	Applied $\Delta\sigma$ (MPa)	Surface Defect	Predicted Life (N)
Blade 01	19	971.7	Yes	5.66×10^5	50	1029.6	Yes	1.92×10^5
Blade 02	41	818.6	No	1.53×10^6	33	706.6	Yes	1.36×10^6
Blade 03	195	768.0	Yes	1.23×10^5	114	1077.6	Yes	6.56×10^4
Blade 04	23	564.7	Yes	4.78×10^6	40	590.8	Yes	2.18×10^6
Blade 05	44	1162.9	No	2.58×10^5	44	1270.2	Yes	8.43×10^4
Blade 06	207	423.1	Yes	8.44×10^5	208	656.6	Yes	1.95×10^5
Blade 07	60	728.3	Yes	6.31×10^5	241	710.9	No	4.37×10^5
Blade 08	-	-	-	-	189	867.5	No	2.69×10^5
Blade 09	116	893.5	Yes	1.35×10^5	134	998.2	Yes	7.40×10^4
Blade 10	33	1095.6	Yes	2.11×10^5	68	1290.8	No	1.12×10^5
	Largest Defect				Largest Stress Range			
	Size (μm)	Applied $\Delta\sigma$ (MPa)	Surface Defect	Predicted Life (N)	Size (μm)	Applied $\Delta\sigma$ (MPa)	Surface Defect	Predicted Life (N)
Blade 01	206	505.7	No	1.83×10^6	50	1029.6	Yes	1.92×10^5
Blade 02	120	118.0	No	4.00×10^8	21	844.7	No	2.07×10^6
Blade 03	203	1067.8	No	1.01×10^5	114	1077.6	Yes	6.56×10^4
Blade 04	80	67.9	No	3.76×10^9	41	608.0	No	5.62×10^6
Blade 05	76	334.1	No	2.69×10^7	29	1349.8	No	1.41×10^5
Blade 06	588	211.9	No	7.24×10^6	195	666.1	No	7.26×10^5
Blade 07	397	205.0	No	1.39×10^7	60	728.3	yes	6.31×10^5
Blade 08	241	428.7	Yes	6.56×10^5	189	867.5	No	2.69×10^5
Blade 09	151	999.2	No	1.90×10^5	35	1006.3	No	6.25×10^5
Blade 10	122	131.5	No	2.83×10^8	35	1291.4	No	1.65×10^5

Table 10. Model parameters of defect size, stress, predicted life, and surface location. One defect is called out for each turbine blade based on the attributes of: initiated fracture, shortest predicted life, largest defect, highest stress at the defect location.

A large size difference was noted between the failure initiating defects of the axially loaded fatigue bars and the bending loaded turbine blades. Due to the geometry of the fatigue bars, approximately 28% of total volume experienced stresses at or near the maximum applied stress. In comparison, the turbine blade load case only allowed approximately 2.5% of the total blade volume to experience a stress value within 50% of the maximum applied stress. The large volume percentage of the fatigue bars allowed more opportunities for large defects to be placed where they could lead to failure. While large defects where found on the turbine blade fracture surfaces, they tended to form within the core of the blade where bending stresses were much lower.

There remains the potential across all of the samples that larger defects existed off of the fracture surface planes that were studied.

5.5 Model Assessment

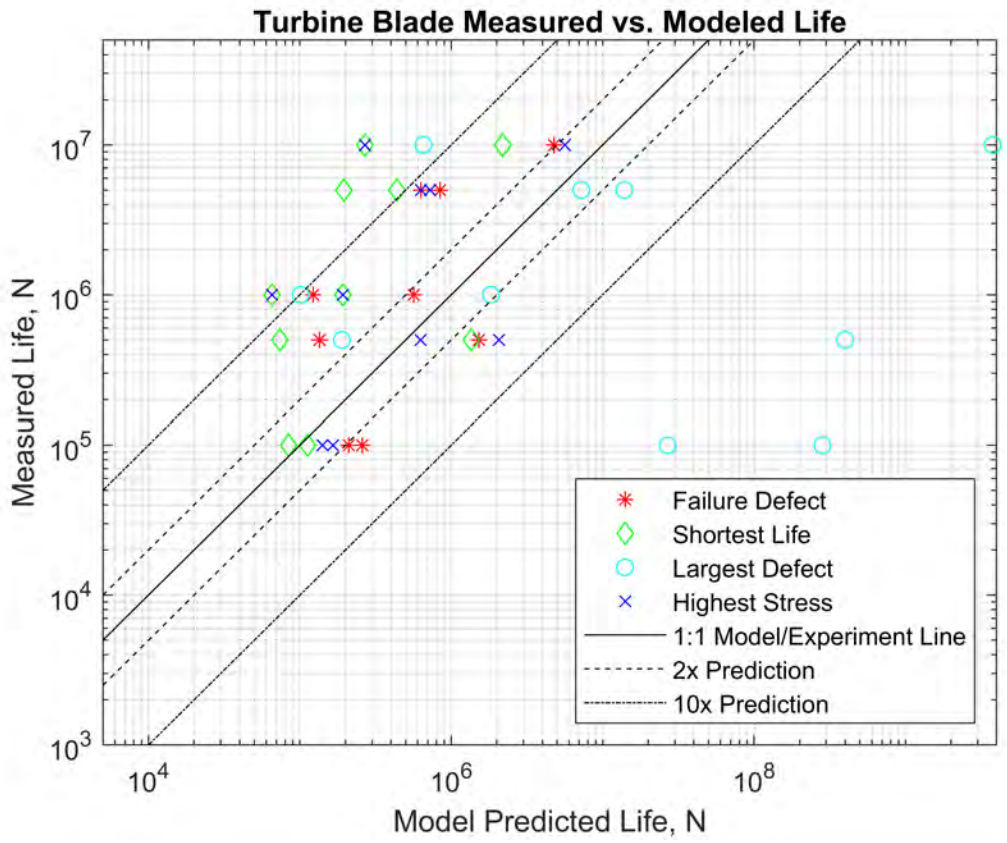

Figure 49. Measured life vs. modeled life for each turbine blade. Assessments on the defects that led to failure, the shortest predicted life defects, the largest measured defects, and the defects at the highest stress values.

Assessing the predicted life of each defect (Table 10) against the experimental life values (Table 8) produced Figure 49. The set of shortest predicted life defects averaged 10.3x lower life predictions than the experimental data with a standard deviation of 12.63, creating the most conservative of the data sets. The largest stress value predictor also created a conservative data set with a mean prediction of 6.6x lower than the experimental data and a standard deviation of 12.23. Applying the largest

measured defect predominately over predicted the component life with an average of 425x longer life predictions than the experimental data. This over prediction is attributed to the low stress locations that the largest defects formed at during the AM production. The failure initiating defects averaged predictions 2.4x below the experimental data with a standard deviation of 4.38. This created both the tightest grouping, and the most accurate predictions against the experimental data. Going forward, only the failure initiating defect set was assessed.

Applying the turbine blade defects identified as initiating failure with their experimental life values (Tables 8 & 10) and the failure inducing defects from the fatigue bar testing with their experimental life values (Tables 7 & 9) to the finite fatigue life El-Haddad model generated Figure 50. The Basquin fit line (Fig. 50A) was the Stress to Life (S-N) curve based on the material properties in Table 1, and assumed that the failure mechanism was solely due to the material fatigue limit. All of the experimental data from the turbine blades and fatigue bars fell below the Basquin fit line, implying that the Basquin fit did not accurately capture the failure mechanisms for AM components. By turning the finite fatigue life El-Haddad model, adjusted S-N curves were generated from discrete defect sizes to cause failure. The defect size dependent S-N curves included LEFM in addition to the material fatigue limit when predicting the S-N relationship. The failure defects from the fatigue bars and the turbine blades correlate with the El-Haddad predicted S-N curves. Figure 50A demonstrated that the turbine blades and fatigue bars followed different S-N trend lines based on the defect sizes that led to failure. The fatigue bar failure defects averaged 364 μm, and the experimental data was predominately between the 250 μm and 450 μm S-N trend lines. In contrast, the turbine blade failure defects averages 82 μm, and were clustered around the 50 μm S-N trend line.

Figure 50B plotted the experimental data against the traditional El-Haddad curves

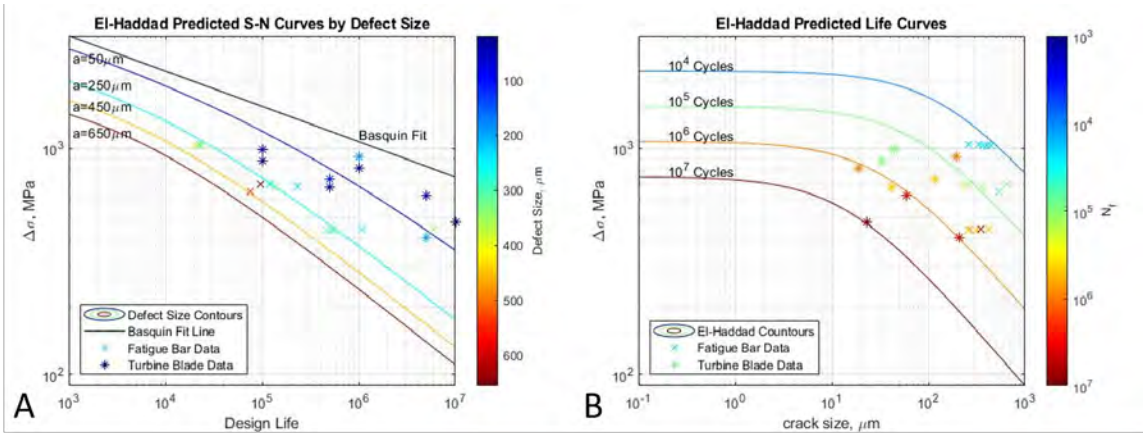

Figure 50. A) El-Haddad predicted S-N curves based on fixed defect sizes. B) El-Haddad finite life curves.

where each contour was a constant life value dependent on the defect size and applied stress range. The El-Haddad model demonstrated a good agreement between the test and prediction life values across three orders of magnitude for the design life. As with the S-N curves, there was a clear delineation between the fatigue bar data and the turbine blade data based on the defect size. The larger failure defects from the fatigue bars placed them in the LEFM dominated region of the El-Haddad curve. The smaller turbine blade failure defects pulled the data left enough to be within the bend of the El-Haddad plot. That region of the curve was influenced by both the material fatigue limit and LEFM.

5.6 Summary Remarks

This research demonstrated the validity of the finite fatigue life El-Haddad model using new experimental data. The data verified that the finite fatigue life El-Haddad generated a solid prediction of the fatigue life. Augmenting the model with FEM location dependencies emphasized the importance of defect location when predicting finite fatigue lives. The same model was applied to both the axial loaded fatigue bars and the bending loaded turbine blades, demonstrating a degree of independence in

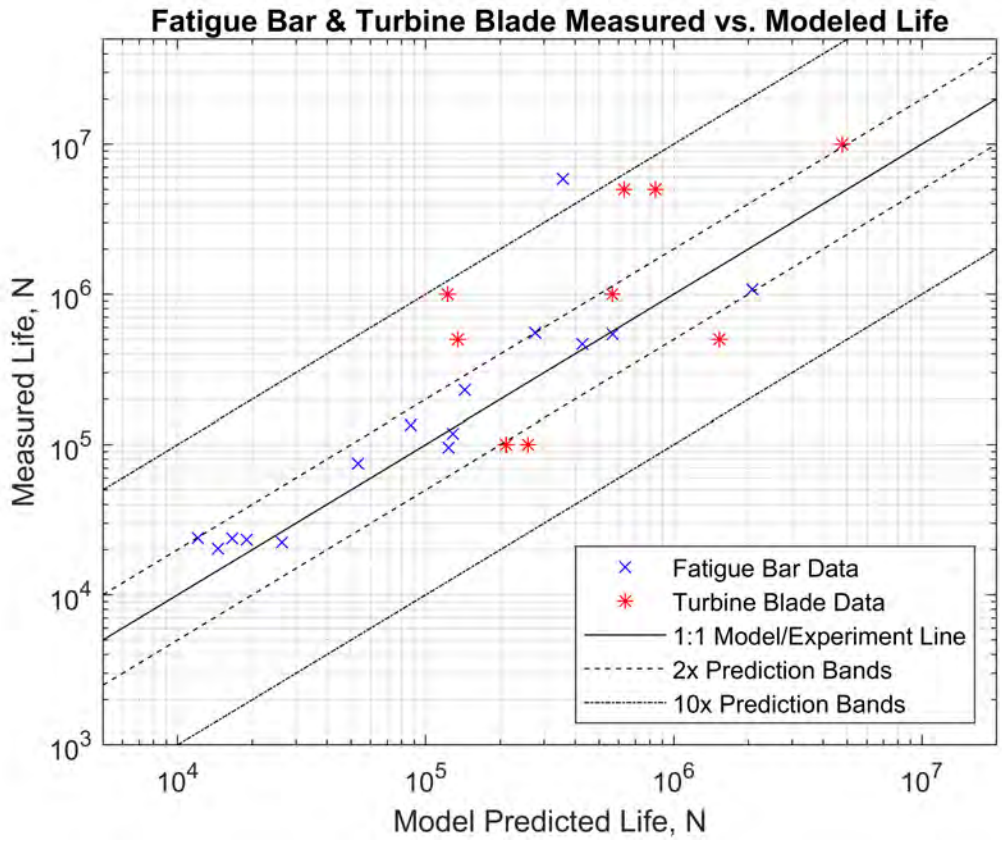

Figure 51. Measured life vs. modeled life for the fatal defects from the fatigue bars and the turbine blades. While the fatigue bar predictions held a tighter fit to the experimental data, the turbine blade predictions continued to trend with their experimental data.

the applied load case.

Figure 51 is the predicted fatigue life against the experimental fatigue life. Fatigue bar data was collected for values ranging from 10^4 through 10^6 cycles of fatigue life. With one exception, the finite fatigue life El-Haddad model predicted a failure life within 2x of the experimental values. The collected turbine blade data spanned 10^5 to 10^7 cycles of fatigue life. While the El-Haddad predicted life of the turbine blade data did not agree with the experimental data as well as the fatigue bar data did, the turbine blade predicted life values trended with the experimental results with a slightly conservative tendency in the predictions.

While the fatigue bar specimens all failed to large defects where LEFM was mod-

eled as the dominate failure mechanism, the experimental data from the turbine blades demonstrated that a large range of AM defects had the potential to limit the fatigue life. Failure defects in the ten tested turbine blade specimens ranged from 19 μm to 207 μm. The smaller initial defect sizes provided data along the blended region where both material fatigue properties and LEFM contributed to fracture. The largest of the failure defects were in the region dominated by LEFM.

VI. Satellite Application

6.1 Overview

Prior work has demonstrated that fatigue life is usually limited by relatively small defects in regions near the maximum stress locations [77, 95]. By developing the relationship between AM defect sizes, applied stress distributions, and fatigue life, the proposed model specifies the defect sizes that could lead to early fatigue failure and the structural locations that must be inspected.

The NASA Standard for Additively Manufacture Space Flight Hardware by Laser Powder Bed Fusion in Metals (MSFC-STD-3716) includes an intensive test campaign to document the fatigue life of an AM component and requires Non-Destructive Evaluation (NDE) [24]. The standard further leaves it up to the structural assessment community to define the critical flaw size for NDE. This paper specifies a method to define the critical flaw size based on the design life and applied stress. The proposed method also predicts critical inspection regions where AM defects could lead to fatigue life failure. Applying the predicted critical flaw size and failure locations enables customized NDE requirements based on the geometry and load to certify AM components for space within the scope of the NASA standard.

A prime candidate for limited life application of AM components are satellite structures. These are subject to a dominate vibration event during launch that defines the design life. During the launch event, the launch vehicle generates a significant amount of vibrational energy that the satellite structure must withstand across a wide range of frequencies [96]. After separation from the launch vehicle in space, the satellite experiences minimal cyclic loading. By designing a satellite structure to survive the short life required by launch with some margin, structures can be further optimized, reducing the total structure mass and freeing more of the mass budget for

payloads.

In this research, a technique was developed to predict the smallest defect size that could induce failure and bound the locations where larger defects could result in failure (Fig. 52). By applying the desired design life and the maximum applied stress range into Equation 15 for N and $\Delta\sigma$, a minimum failure inducing defect size was predicted. Any defects generated due to the AM process that were smaller than the predicted failure-inducing defect size were assessed as incapable of leading to fracture within the fatigue design life regardless of where they were generated. If the expected defect distribution contained defects larger than the minimum failure-inducing defect size, Equation 15 was applied with the design life for N and the largest expected defect for a to predict the minimum stress range that could potentially lead to failure before N cycles. By mapping the locations in the Finite Element Model (FEM) that experience the predicted minimum stress range, critical failure locations were identified that could grow a defect to early failure if the correct defect size was formed during the printing process. These critical failure regions define where NDE is needed most to certify a component for mission success.

6.2 Materials and Methodology

The method outlined in Figure 52 was verified using AM specimens printed in nickel-based super-alloy 718 (IN718). The AM process naturally generated small defects throughout the parts in relationship to the processing parameters. The relative density of the final products and potential defect sizes were controlled through the processing parameters such as laser power, scan speed, spot size, and hatch spacing [65, 66]. Figure 53 was the predicted defect distribution based on the applied processing parameters of laser power, scan speed, hatch spacing, and layer thickness [66].

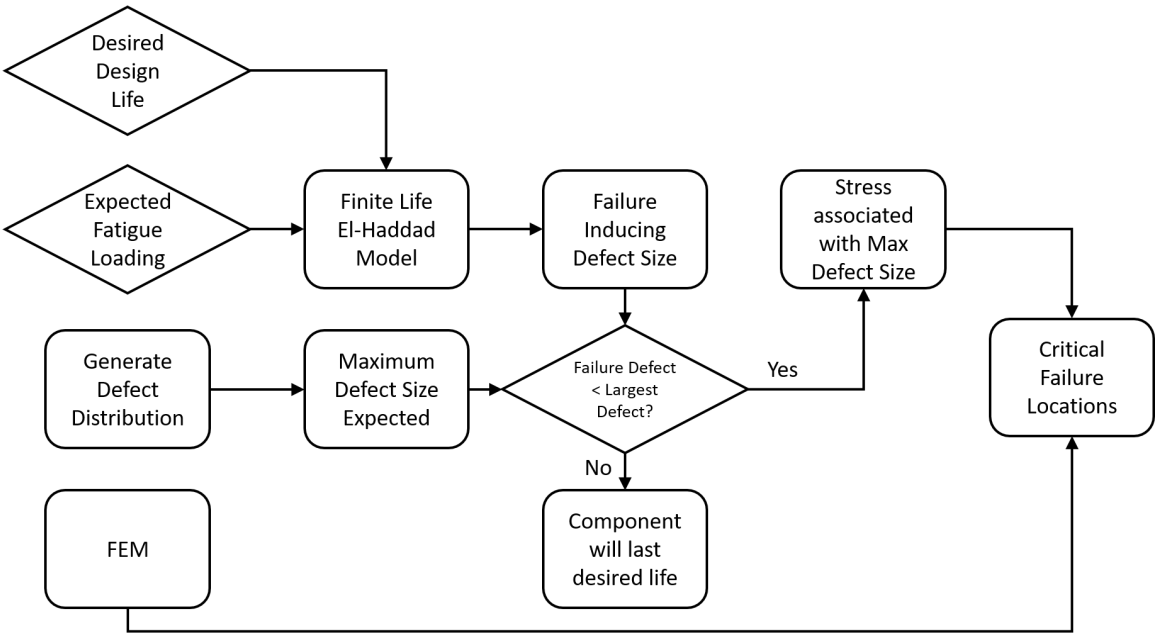

Figure 52. Process flow to predict minimum defect size of interest and potential failure regions.

Ten turbine blade and fifteen fatigue bar specimens were produced in one print on an M2 Cusing Laser Powder Bed Fusion (LPBF) printer. The turbine blades were fatigue tested by inducing the second bending vibration mode using the fatigue step test. The fatigue bars were axially loaded to a maximum force, and cycled at 20 Hz until failure [77]. The experimentally measured loads and final fatigue lives formed the finite fatigue life El-Haddad model inputs of design life and applied stresses. While the turbine blade geometry and IN718 material are not considered space structures, they provided the experimental data to validate the methodology in Figure 52.

6.2.1 Test Results

Each turbine blade specimen was vibrated at its unique second bending mode frequency according to the vibrational step test method until failure. A low force input was applied for N cycles, and then incremented up by 34.5 MPa (5 ksi) and ran for another N cycles. The final failure stress was calculated using Equation 20

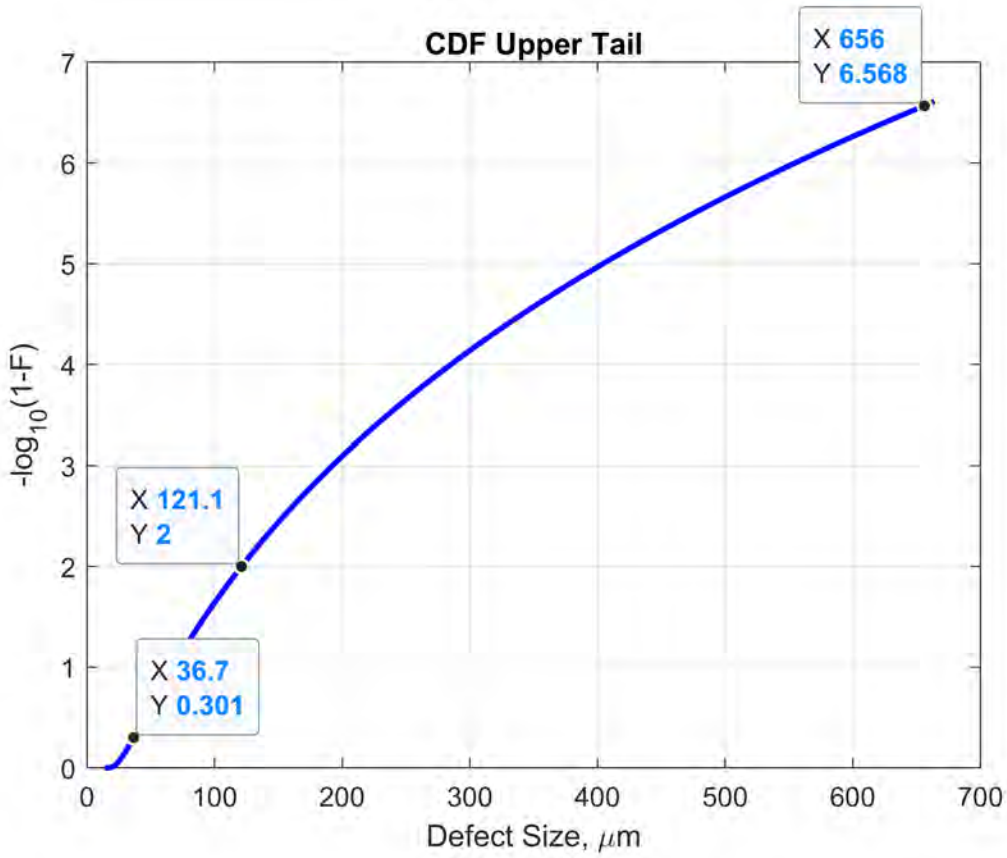

Figure 53. CDF for IN718 processes by Laser Powder Bed Fusion (LPBF). Half of all generated defects were predicted to be under 37 μm, and 99% of defects were predicted under 121 μm. The largest observed defect was 656 μm with an occurrence probability of less than 0.00003%.

based on the percentage of cycles ran in the final step [92, 93].

$$\sigma_a = \sigma_{pr} + \frac{N_f}{N_t}(\sigma_f - \sigma_{pr}) \tag{20}$$

The ten turbine blades were distributed into five groups of two and were tested on an Unholtz-Dickie 20K Electrodynamic Shaker Table at cycle counts of 1×10^5, 5×10^5, 1×10^6, 5×10^6, and 1×10^7. Each turbine blade was equipped with two strain gauges to scale the FEM stress/strain profiles according to the experienced strain at pre-set locations. Post-failure, the fracture surfaces were studied on a Tescan Mira3 Scanning Electron Microscope (SEM) to identify the origin of the failure crack and

Blade ID	Fatigue Life (N)	Applied $\Delta\sigma_{Max}$ (MPa)	Defect Size (μm)	Defect $\Delta\sigma$ (MPa)
01	10^6	1040	19	972
02	5×10^5	854	41	819
03	10^6	1187	195	768
04	10^7	591	23	565
05	10^5	1312	44	1163
06	5×10^6	670	207	423
07	5×10^6	857	60	728
08	10^7	872	-	-
09	5×10^5	964	116	894
10	10^5	1313	33	1096

Table 11. Defect sizes and applied stress ranges that experimentally caused failure for the turbine blades.

the initial defect size that caused failure. By mapping the defect location onto the turbine blade FEM, an applied stress for each failure defect was calculated (Table 11).

The fifteen fatigue bar specimen were broken up into three groups of five and tested on an 810 MTS Load Frame with a 100kN Load Cell. Each group was loaded to a different maximum stress value (221 MPa, 345 MPa, and 517 MPa) and cycled at 20 Hz under a fully reversed load profile until failure occurred. The fracture surfaces were analyzed on the SEM to find the initial defect that caused failure (Table 12). One of the fatigue bars from the 221 MPa set experienced testing anomalies and was removed from the set, leaving a total of fourteen fatigue bar specimens.

6.2.2 Minimum Defect Analysis

Following the initial steps in Figure 52, the experimental life and maximum applied stress ranges from the fatigue testing (Tables 11 & 12) were applied to the finite fatigue life El-Haddad Equation (Eq. 15). The output predicted a minimum defect size for both the turbine blades and fatigue bars (Table 13). From the experimental values, these would be the smallest possible defects that predicted the same fatigue life. The

Fatigue Bar ID	Fatigue Life (N)	Applied $\Delta\sigma_{Max}$ (MPa)	Defect Size (μm)	Defect $\Delta\sigma$ (MPa)
01	230,416	690	236	683
02	22,356	1034	262	1039
03	464,646	441	314	437
04	75,059	690	538	648
05	23,888	1034	448	1032
06	553,711	441	425	438
07	118,499	690	248	691
08	20,368	1034	402	1028
09	1,075,687	441	269	441
10	95,388	690	656	691
12	23,776	1034	370	1027
13	541,165	441	261	434
15	134,758	690	355	671
16	23,250	1034	330	1037

Table 12. Defect sizes and applied stress ranges that experimentally caused failure for the fatigue bars.

final S-N curves from the turbine blade testing performed near the Basquin Equation predicted lives, as a result the minimum predicted defect sizes were all under 50 μm. In three of the turbine blade samples the measured stress range and component life predicted a negative minimum defect size. In those cases, the measured stress range was larger than the Basquin predicted stress range (Eq. 1). The minimum defect size was set to zero indicating that those parts would not predict a better life even with a perfect manufacturing process.

In contrast, the fatigue bars predicted minimum defect sizes in the range of 150 μm to 400 μm. Correspondingly, the S-N relationship from the fatigue bar experimental data was significantly less than the Basquin Equation prediction for the material. For the fatigue bars, the AM defects measurably degraded the fatigue life.

Across all twenty four specimens, only three cases had the measured fatal defect less than the predicted minimum defect size. In Turbine Blade 02, the difference was 1 μm, and was within the tolerance for the defect measurements. Fatigue Bars 02 and

	Turbine Blades		Fatigue Bars	
ID	Minimum Defect Size (μm)	Minimum $\Delta\sigma$ (MPa)	Minimum Defect Size (μm)	Minimum $\Delta\sigma$ (MPa)
01	2	237	161	381
02	42	297	297	758
03	0	237	289	305
04	9	109	368	538
05	28	494	284	744
06	10	138	255	288
07	0	138	265	469
08	0	109	317	776
09	26	297	157	231
10	28	494	310	501
12			285	745
13			259	290
15			241	451
16			289	750

Table 13. Predicted minimum defect sizes and minimum applied stress ranges to cause failure based on the experimental lives. The minimum defect sizes applied the maximum stress range and the minimum stress range applied the largest observed defect size of 656 μm.

07 differed by 35 μm and 17 μm respectively. Both of those samples also measured a slightly higher stress range at the fracture surface than was nominally applied. For the fatigue bars, the maximum and applied stresses were based on average diameter measurements of the specimens. In both of these samples, the diameter at the fracture surface was measured as less than the average diameter along the length of the test gauge. To ensure this will not happen in an application problem, a factor of safety should be applied to the peak stress.

6.2.3 Minimum Stress Analysis

From the experimental data in Table 11 and Table 12, it was clear that defects existed in the samples larger than their minimum defect sizes. This meant that where the defects formed would impact the fatigue life. Continuing along the flow chart (Fig. 52), by applying the largest expected defect with the design life to Equation

15, a minimum applied stress range was produced (Table 13). In this case the largest expected defect was assumed to be the largest measured defect at 656 μm. Based published IN718 defect distributions [66], a defect of that size or larger had a probability of less than 0.00003% to form (Fig. 53).

For the turbine blade data every location that experienced a stress range greater than or equal to the calculated minimum stress range (Table 13) was identified on the FEM. Figure 54 plotted the critical locations for design lives of 10^5, 10^6, and 10^7 cycles fatigue life. As the design life increased, the potential areas where defects could grow to failure also increased. At the design life of 10^5 cycles, approximately 28% of the blade volume was assessed as potential failure initiation points. In contrast, when the turbine blade design life was increased to 10^7 cycles, the potential failure region increased to 60% of the total volume.

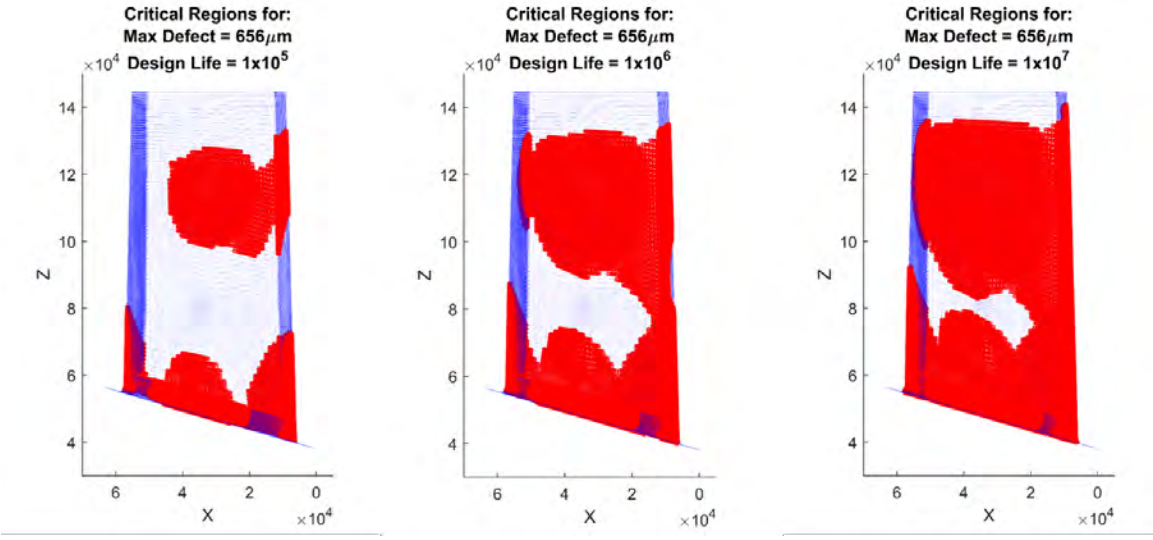

Figure 54. Potential defect forming locations on the turbine blade specimens based on the largest expected defect and the stress profile across the geometry.

The critical regions from Figure 54 were further refined by applying the fatigue lives and initial defect sizes that that led to failure for the turbine blades. Figure 55 depicted the critical regions for blades 01, 04, and 09. When applying the measured initial defect and fatigue life, the critical regions were restricted to very small regions

along the root of the blades. Developing the capability to better limit the largest expected defect would reduce the defined critical regions and constrain the required inspection volume.

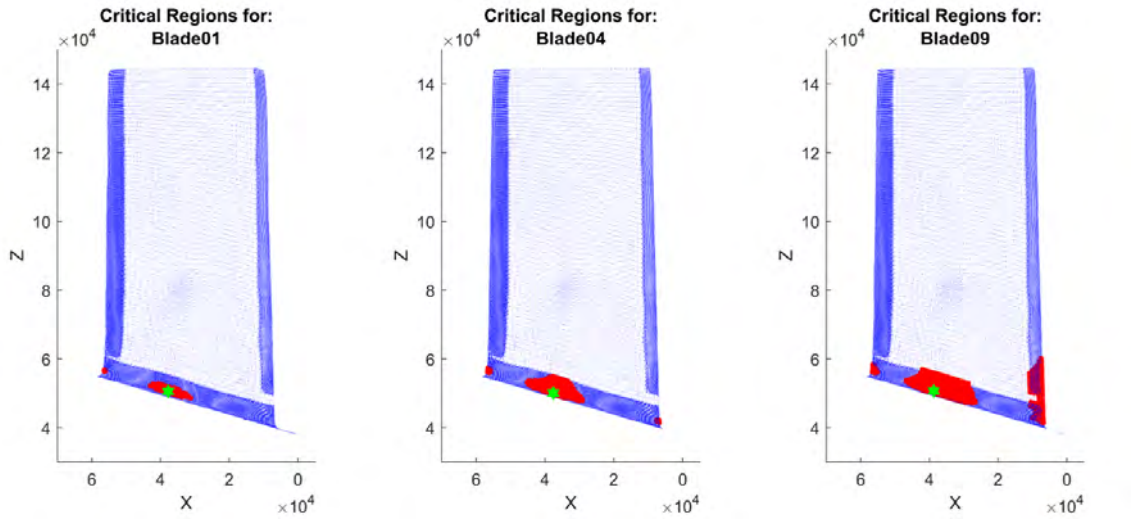

Figure 55. Predicted crack initiation regions for Turbine Blades 01, 04, and 09. The star was the experimental crack initiation point for each specimen.

By understanding the load case and the defect population from the AM process, bounds have been developed on defect size and applied stress range combinations that hold the potential to lead to failure. Figure 56 plotted the bounding defect sizes and stress ranges for Turbine Blade 01. Any defect and stress combination that fell above the target life curve could result in pre-mature failure. Combinations below the target life curve should survive at least the target cycle life.

6.3 Satellite Application

The process outlined in Figure 52 is directly applicable to satellites. The following section outlines how the finite fatigue life El-Haddad model was adapted to predict the minimum defect size that could generate fatigue failure and to predict the locations where AM defects create a failure concern. This analysis utilized the 12U CubeSat chassis shown in Figure 57. This particular chassis was selected for analysis because

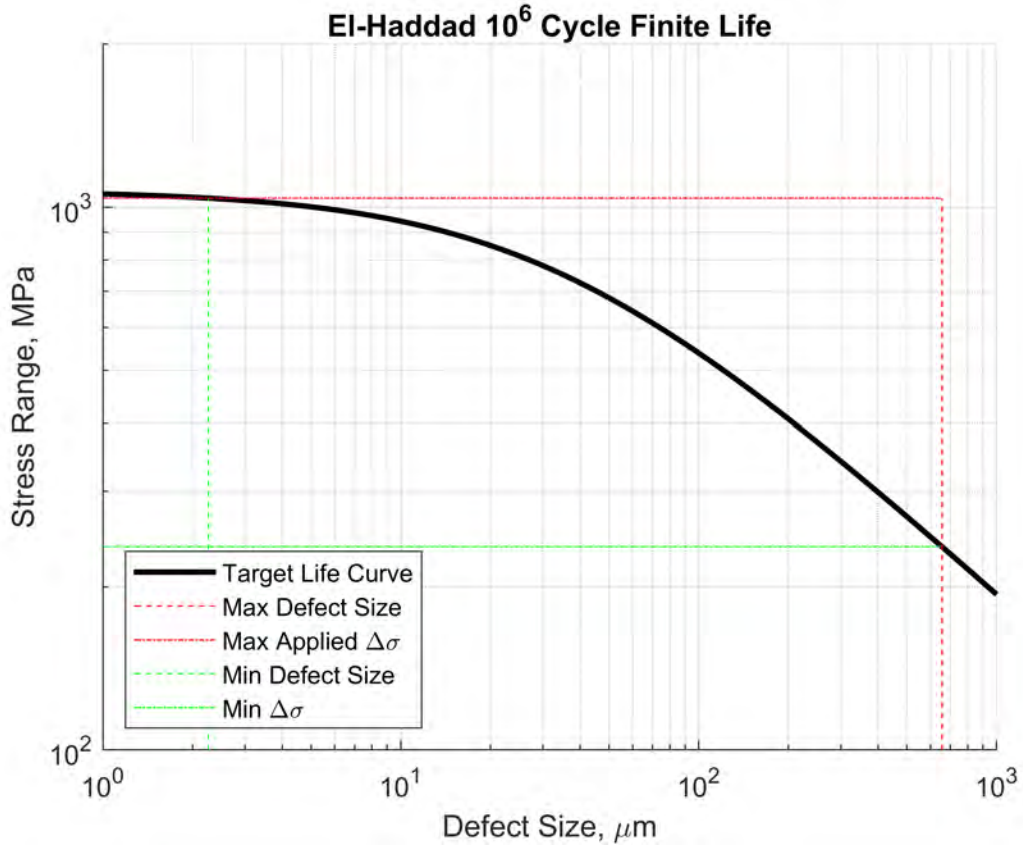

Figure 56. Bounding defect sizes and stress ranges that could lead to failure for Turbine Blade 01. The maximum stress range is from the maximum applied stress in the experimental data. The maximum defect size is the largest observed defect across all of the specimen at 656 μm.

vibrational testing data was readily available to set the stress profiles and the structure volume was within AM print volume capabilities. The 12U chassis was tested in the empty and maximum mass configurations on a vibration table. The experimental data provided the foundation to generate the required stress profiles. The FEM was validated at the component level through free-free vibration testing and at the assembly level through shaker table testing of the 12U CubeSat in both the empty and fully loaded configurations [13].

The satellite vibration environment is dominated by the launch. A typical launch generates less than ten minutes of strong vibration, covering the first and second stages [97]. Multiplying the launch duration by the primary axial vibration modes

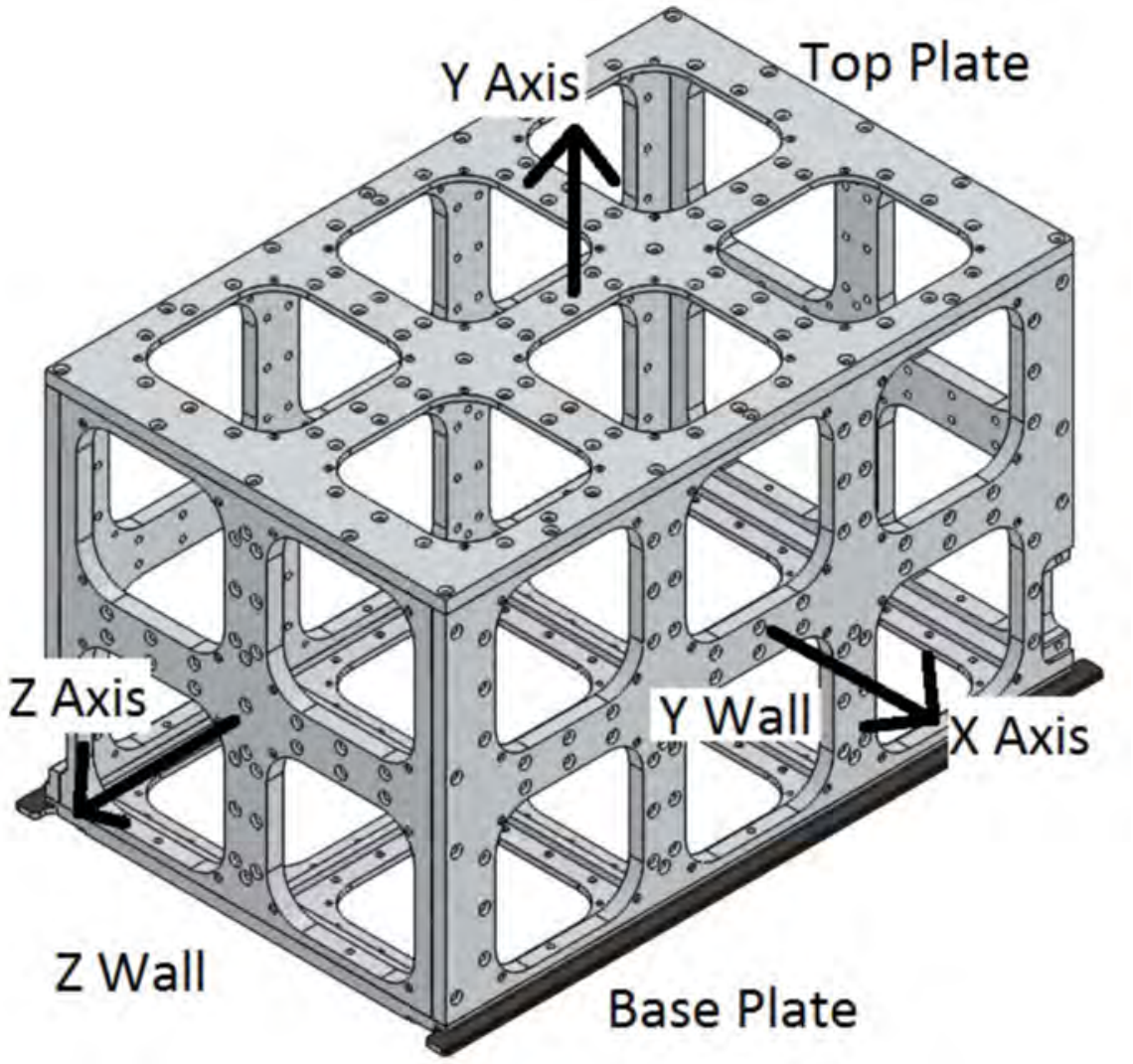

Figure 57. Empty configuration for the 12U CubeSat chassis [13].

generated a first order estimate of the required cyclic fatigue life to get on orbit. For the applied 12U CubeSat, the first natural frequencies along each axis ranged from 90 Hz to 500 Hz depending on the final load configuration. Figure 58 depicted the first three modes for the empty 12U CubeSat. When the Base Plate was constrained in the launch configuration, the chassis flexed along the X axis (Fig. 58A) at 343 Hz, along the Y axis (Fig. 58B) at 394 Hz, and along the Z axis (Fig. 58C) at 489 Hz. The additional mass in the fully loaded configuration reduced the vibrational frequencies, so that the X axis bending was reduced to 97 Hz [13]. Multiplying the largest of the

axial frequencies (500 Hz) with the launch duration of 10 minutes created an upper limit of 3×10^5 vibrational cycles experienced during launch.

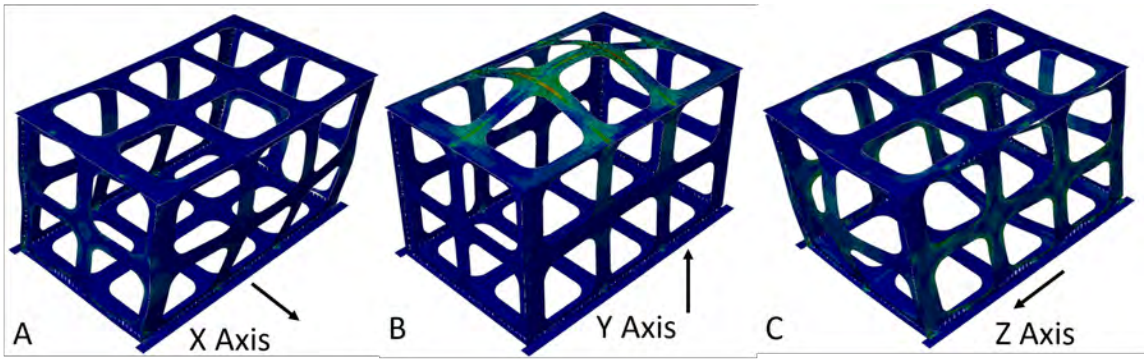

Figure 58. The first vibrational mode along each of the three primary axes. A) X Axis bending (343 Hz). B) Y Axis bending (394 Hz). C) Z Axis bending (489 Hz).

Before applying the method presented in Figure 52 to the 12U CubeSat chassis, several parameter updates were required. Changing the material from IN718 to printed aluminum required a new Basquin Equation (Eq. 1) and Paris Law (Eq. 5) to define the material fatigue properties and LEFM. A new defect distribution for aluminum predicted if failure inducing defects were a concern. Finally, the FEM stress map associated with the vibrational modes needed to be scaled based on the maximum expected load to generate the potential failure initiation regions.

Since every AM material has a range of processing parameters that generate different material properties and defect distributions [65,66]. In this application a notional set of properties were developed for printed aluminum based on experimental result in the literature.

6.3.1 Material Properties

The material properties of interest were the constants associated with the Basquin Equation (Eq. 1) and the Paris Law (Eq. 5). Both equations are linear in the log space with a coefficient and an exponent to define their respective relationships. The

Basquin Equation was defined off of data from Lee for fully reversed load cycling on traditionally manufactured Aluminum 7075-T6 [98] and produced Figure 59A. The produced fit was compared to several printed aluminum tests [38, 99, 100] and was found comparable to AlSi10Mg results along the range of 10^4 through 10^6 cycles of fatigue life. The Paris Law was fit used ASM Handbook, Volume 2 for the crack growth of Aluminum 7075-T6 [101] (Fig. 59B). Crack growth rates for AM aluminum alloy Scalmalloy measured very close to the ASM Handbook values [102]. Crack growth curves for printed AlSi10Mg generated a slightly slower crack growth rate for the fully reversed load case [5]. By retaining the faster crack growth rate in literature, the model generated a conservative assessment.

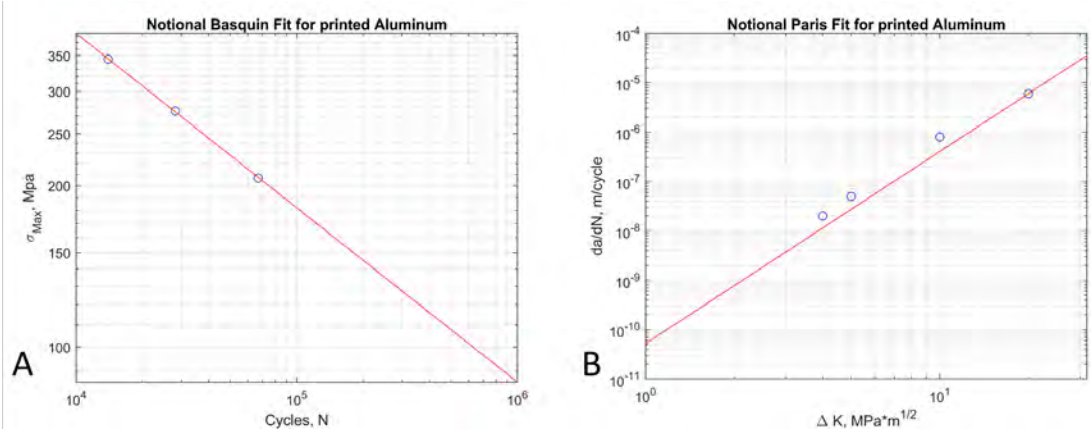

Figure 59. A) Basquin fit based off Al 7075-T6 experimental data. Fit parameters were A = 7711, and b = −0.3254. B) Paris fit from ASM Material Handbook, C = 5.205×10^{-11}, n = 3.892

6.3.2 Defect Distribution

One defect distribution set for printed Aluminum was selected for this analysis. The applied defect distribution (Fig. 60) was generated from the Weibull distribution based on data from Maskery *et al.*. The distribution was generated through X-ray computed tomography on AlSi10Mg [103]. The predicted aluminum defects were significantly smaller than those generated in IN718 (Fig. 53) with 99% of all

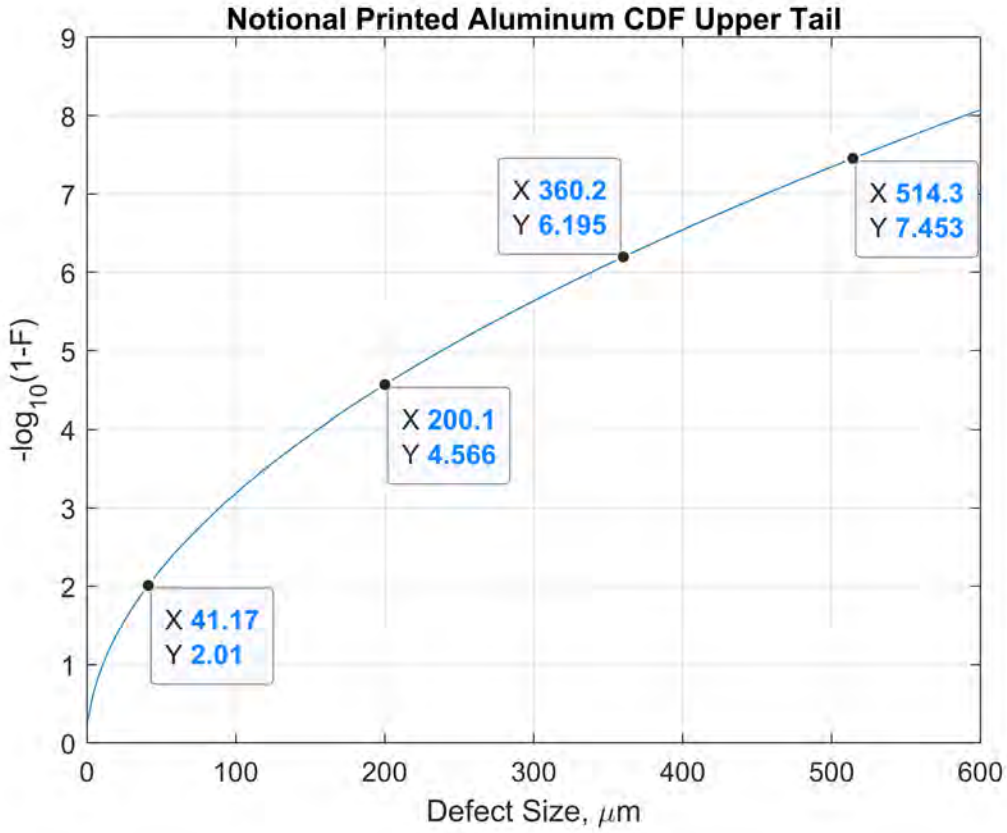

Figure 60. Notional CDF for printed Aluminum. Documented defects in aluminum prints were significantly smaller than those in IN718 (Fig. 53), however large defects have been observed.

predicted defects being less than 42 μm. Even with the smaller defect distribution, extreme defects have been seen in the literature. Maskery *et al.* [103] and Beretta [19] documented defects up to approximately 200 μm. Wu *et al.* identified defects up to 360 μm [38]. Finally Gumpinger *et al.* found a surface defect in printed aluminum that was 514 μm [70].

6.3.3 Load Case

For the analysis of this case, the defined load was derived from the NASA General Environmental Verification Standard (GEVS) which defined the applied acceleration spectral density (ASD) from 20 Hz to 2,000 Hz [96]. Sine sweeps across the frequency

range for the 12U chassis on an MB Dynamics shaker table generated an acceleration response per frequency for select locations. By multiplying the NASA GEVS profile with the gain per frequency and summing, a peak acceleration was calculated for each accelerometer location. The calculated accelerations were then applied to the FEM element closest to each accelerometer to identify the experienced stress and to scale the FEM stress profile. The maximum applied stress range to the 12U chassis varied from 135.5 MPa for the empty chassis down to 59 MPa for the completely loaded chassis.

6.3.4 Minimum Defect of Interest

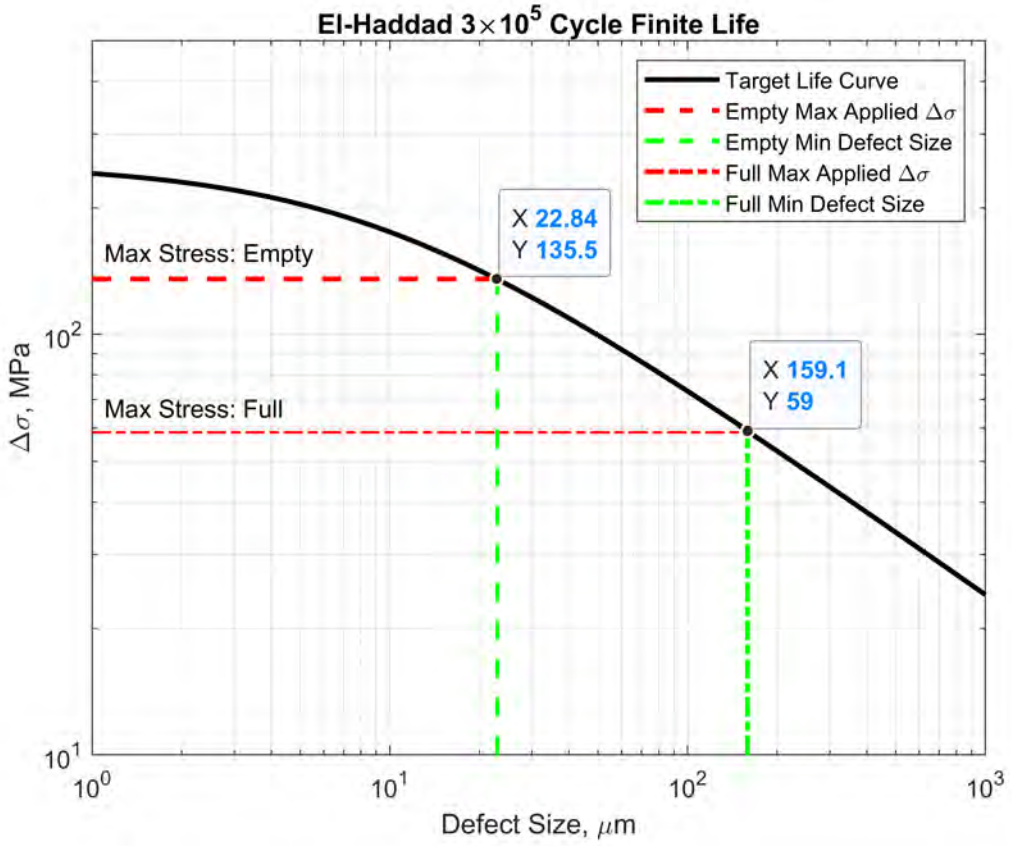

Figure 61. Minimum predicted defects sizes that could lead to failure within 3×10^5 cycles fatigue life.

Applying the design life of 3×10^5 cycles and the derived maximum stress ranges for the empty and full 12U CubeSat chassis into the finite fatigue life El-Haddad model (Eq. 15) generated Figure 61. For the empty 12U chassis, the smallest defect that could lead to failure was predicted at 22.8 μm. Based on the defect distribution in Figure 60, approximately 96.7% of all defects generated should be smaller. When the peak stress range associated with the full 12U CubeSat was checked, the minimum defect that could cause failure was calculated at 159.1 μm. This translated that 99.99% of all generated defects should be smaller than the minimum defect of interest.

6.3.5 Failure Prediction Regions

The next step in the process (Fig. 52) was to assess if defects larger than the failure inducing defect were possible from the AM process. Based on Figure 60, defects larger then 159 μm have been documented. In this example, the maximum defect was defined at 400 μm, which corresponded to approximately one out of five million defects. Applying the maximum defect size to the finite fatigue life El-Haddad model (Eq. 15) for the design life of 3×10^5 cycles predicted a minimum fracture stress range of 37.8 MPa (Fig. 62).

Finally, the FEM was filtered to identify every location that experienced the minimum fracture stress range along at least one of the three primary axis modes. Figure 63 highlighted every region in the empty 12U chassis that predicted a stress range of at least 37.8 MPa. Across the empty 12U geometry, less than 0.5% of the structural volume was assessed as potential locations to generate a fatal crack assuming a defect between 22.8 μm and 400 μm formed.

Performing the same analysis on the full 12U chassis (Fig. 64) predicted 0.3% of the total volume to be susceptible of fatigue failure within the applied design life of 3×10^5 cycles. None of the critical locations on the fully loaded 12U were associated

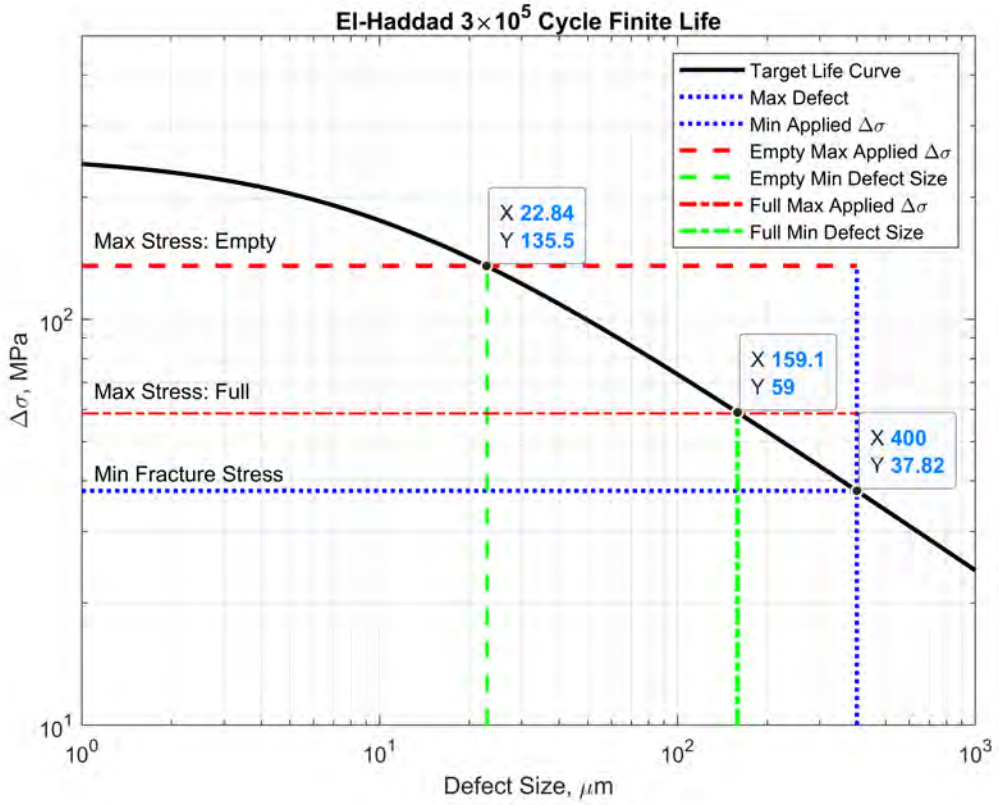

Figure 62. Addition of the minimum stress to cause fracture within 3^5 cycles of fatigue life. The minimum stress value assumed that no defects larger than 400 μm were generated from the AM process.

with the the external structure. Figure 65B pulled out a single mass stack from the full 12U chassis. All of the critical regions associated with the fully loaded 12U CubeSat were where the mass plates connected to their corner supports or where the support bars connected to the adaptor plates (Fig. 65A).

6.4 Summary Remarks

The application of the developed methodology in Figure 52 generated two key contributions associated with certifying AM components for space. First, by applying the required design life and expected maximum stress load into the finite fatigue life El-Haddad model, a minimum defect size was defined. The minimum defect size sets

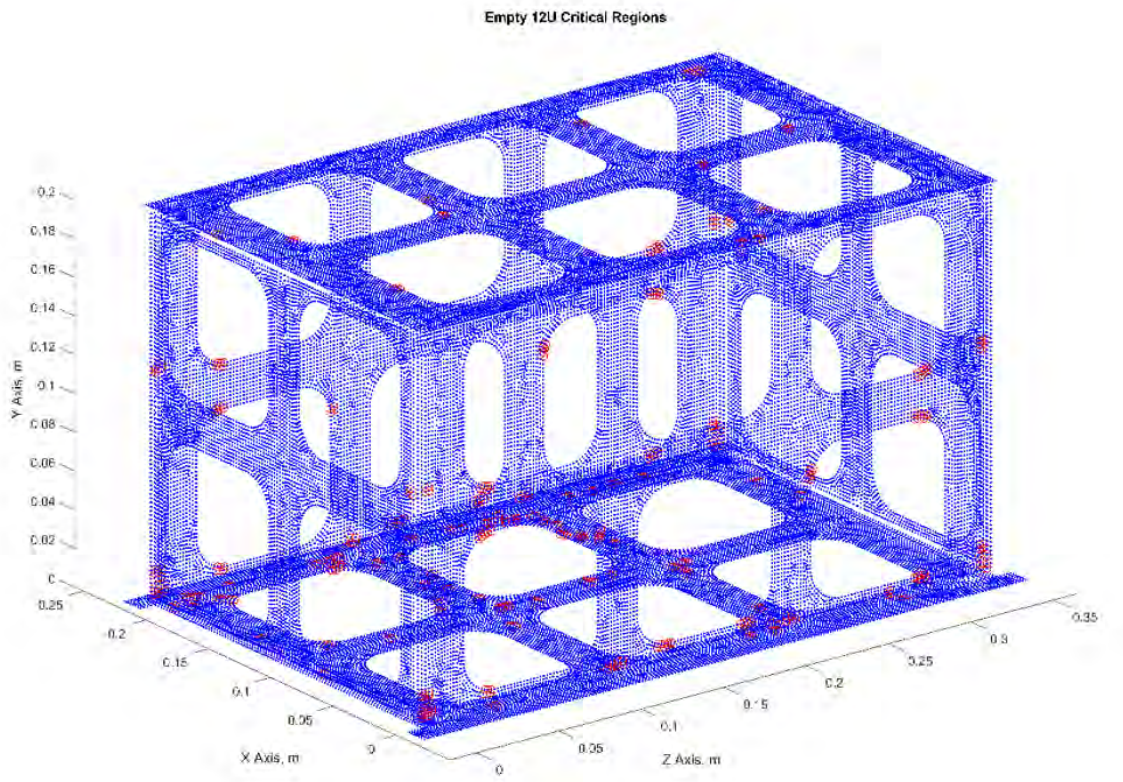

Figure 63. The critical regions where crack growth could initiate from for an empty 12U chassis. Predicted crack initiation regions were predominately found along the view-port corners and at screw connection locations.

the objective goal for NDE detection resolution and AM process improvements. If all defects were ensured to be smaller, then failure due to AM defects would not be an issue within the design life. While it might be feasible with the correct AM parameters and post-processing steps to keep the extreme defects below 159 μm for aluminum, there are no indications that the processes could reduce the extreme defects as far as 22.8 μm. Because AM defects will continue to be a concern in the foreseeable future, the second contribution identified the locations that would require inspection. By understanding the maximum defect size for a material and applied print parameters, the finite fatigue life El-Haddad model predicted a minimum applied stress range that

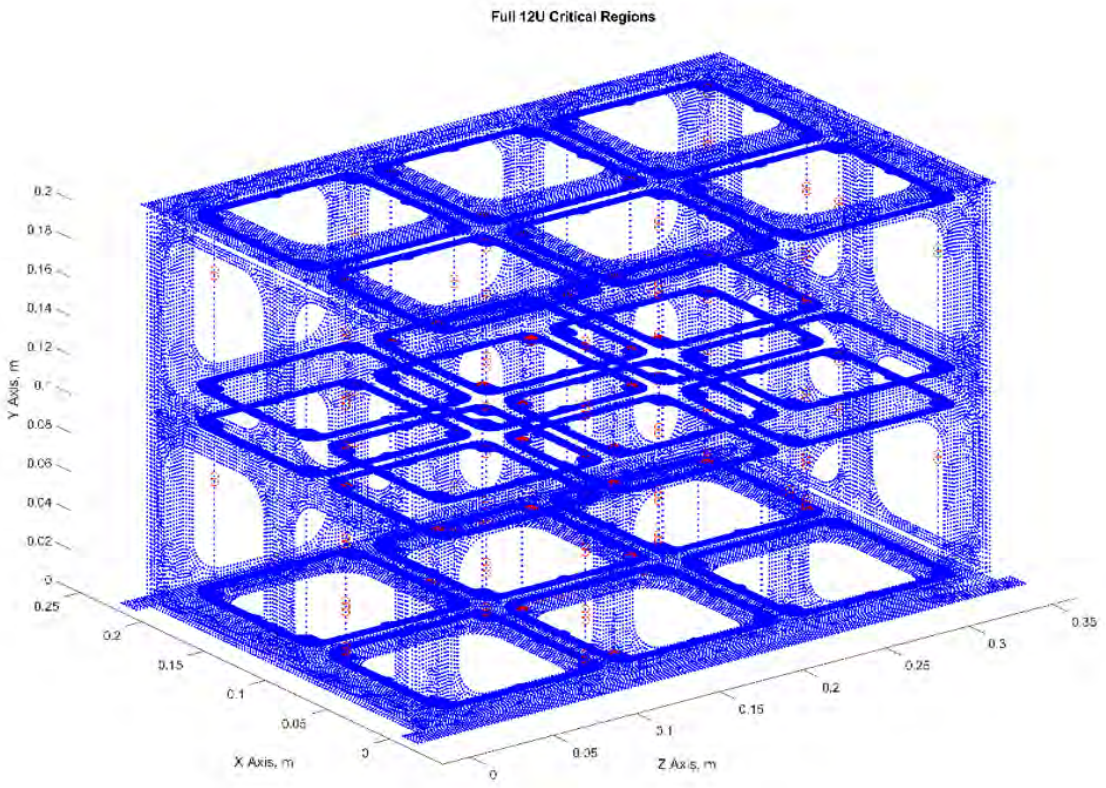

Figure 64. The critical regions where crack growth could initiate from for a fully loaded 12U chassis. Predicted crack initiation regions were solely found within the interior structural elements.

could lead to fracture within the design life. If all load cases were kept below this minimum fracture stress, then fatigue failure would not be a concern. In most cases, there will be experienced stresses between the stress to grow the largest expected defect and the largest stress on the component. By linking the potential failure stresses to a developed FEM, inspection location criteria was defined.

Further work to develop the model includes extending the defect population to be parameterized based on common AM processing parameters. In this paper, the defect population was generated from literature with no concern for how the parts were processed. By creating a defect population based on applied AM parameters,

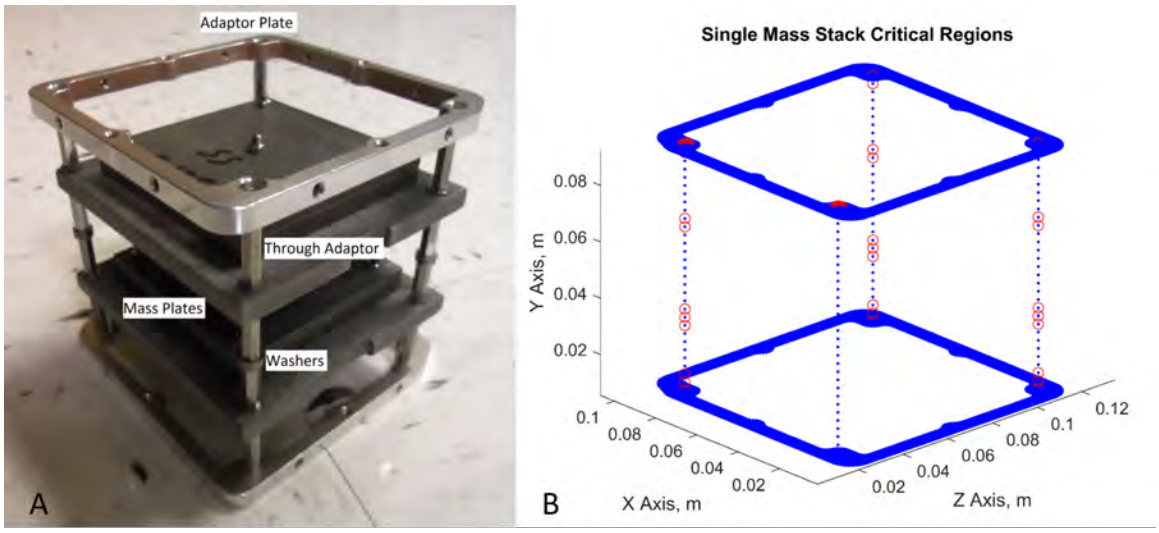

Figure 65. A) One mass stack. B) The assessed critical regions associated with the mass stack.

materials, and post-processing steps, a direct link will be created from print settings to potential failure regions. By balancing the costs associated with reducing the expected defect population with the costs of NDE techniques, bounds on the required AM parameters and NDE resolution can be developed.

VII. Conclusion

7.1 Summary Remarks

This research successfully developed a model to predict fatigue life based on measured defect size and location data. The finite fatigue life El-Haddad model generated the connection between fatigue life, defect size, and applied stress. By augmenting the El-Haddad model with an FEM of the desired geometry, the applied stress became dependent on defect location.

Material properties and final geometry measurements were taken for AM built samples and applied to the El-Haddad model and FEMs. Updates to the FEM improved the stress mapping. The measured stresses ranged between 40% and 230% of the predicted stresses when using the baseline geometry and material properties. When the measured geometry and material properties were applied, the measured stresses ranged from 90% to 110% of their predictions (Ch III).

The developed fatigue life model was validated through vibrational testing at AFRL/RQTI. A total of twenty five specimens were built, quantified, and fatigue tested to failure. Fifteen fatigue bars generated data on axial loading at three different load levels and demonstrated predicted fatigue lives within 2× of the experimental fatigue lives. The fatigue bar data validated that the applied model responded as previously published work. Ten turbine blade samples extended the experimental work to include bending load cases and analyzed the contributions of a complex geometry to the model. The turbine blade predicted lives stayed within 10× of the experimental lives (Ch V).

A second aspect of the research was to predict critical regions where AM defects had the potential to cause fatigue failure before the design life (Ch IV & VI). Identification of a critical region required knowledge of generated defect distributions and a

detailed understanding of the applied loading. Applying the largest expected defect and design life to the finite fatigue life El-Haddad model predicted a minimum stress value that could lead to failure. By filtering the FEM to identify locations predicted to experience at least the minimum stress value, critical regions were defined. Intensive analysis of the turbine blade fracture surfaces to identify initial defect sizes and locations demonstrated merit to the critical region assessments (Ch IV). Across the ten data points, the critical region assessments encompasses the fracture initiation points.

7.2 Future Research

There are several directions of research that will further the fatigue life analysis presented in this dissertation. Research to improve the input parameters would assist in early design application. There are several areas within the developed model that will benefit from additional experimentation and expansion efforts to address built in assumptions. Finally, application of this method will assist in many research applications.

7.2.1 Research into Inputs

Chapter III demonstrated the importance of properly characterizing the material properties and final geometry when applying state-of-the-practice FEM improvement techniques for AM production. To generate an accurate FEM for predicting the stress to location maps, accurate knowledge of Young's Modulus, density, and final geometry are required. Current methods involve experimental testing post print to generate final properties. Applying an intensive research campaign to relate the material properties to applied print parameters will minimize the necessity of post print testing. This has been performed once for the density of IN718 with a function

to predict the mean density based on laser power, scan speed, layer thickness and hatch spacing [66]. An experimental plan could be mounted to expand the work to fit Young's Modulus as well, and/or branch out to additional AM materials.

In addition to Young's Modulus and Density for the FEM development. The finite fatigue life El-Haddad model needs the material properties for crack growth and the Stress to Life (S-N) curve. While adjusting the model from IN718 to printed aluminum in Chapter VI, it was discovered that there is very little published on crack growth rate parameters or S-N parameters based on material, print settings, or load ratios. Research in those areas will enable a broader application of the finite fatigue life El-Haddad model.

Defect distributions are another area where the literature does not document clear input parameters. For this research, prior testing with the same material, and covering identical print parameters provided a defect distribution function [66]. However, that is rarely the case. The aluminum defect distribution applied in Chapter VI was generated from one parameter setting for AlSi10Mg, and there has been no discussion in literature on how the defect populations change based on print parameters or post-print processing.

While characterizing the defect distributions based on material and print parameters would inform on potential defect sizes, improving in-situ monitoring and post-print scanning would directly link defects with locations. Computed Tomography (CT) scans where discussed in Chapter II, and proposed in the original research plan. However, due to complications with processing the scan data, it was dropped in favor of post-fracture, Scanning Electron Microscope (SEM) imagery analysis. Improvements to the scanning process, and being capable of automating the identification of defect size and location would enable pre-test predictions of fatigue life. CT scan processing improvements would also enable further verification of the critical failure

region.

The in-situ monitoring is an active research field to identify defects as they form from data collected during the build. When the capability is proven, it has to potential to remove the need for CT scanning. Post-processing of collected in-situ data could reveal defect sizes and locations. Real-time processing of the in-situ data is the next step to enabling print corrections if a potential failure defect is formed within a critical failure region.

7.2.2 Model Broadening Efforts

The finite fatigue life El-Haddad model was validated through two geometries. The fatigue bars were tested under an axial load, and the turbine blades were tested through a bending vibration load. While that was sufficient to demonstrate the utility of the method; additional loads, geometries, and materials are required to prove the versatility. Chapter VI demonstrated the process to apply the finite fatigue life El-Haddad model to a different material and geometry. However, there is no experimental data to quantify the applicability of the model to the new geometry and material.

One of the assumptions built into the model was the application of the Basquin Equation 1 to approximate the defect free S-N relationship. The Basquin Equation breaks down at very high and low fatigue lives based on material properties. While the applied life ranges in this research did not push the boundaries, it will be important to develop the application limits of this model, and determine the appropriate model augmentations to adjust the fatigue life predictions when operating in the extremely high or low life regimes.

Another key assumption of this model was that only axial forces factored into fatigue life. The fatigue bar testing did not have any shear stresses by design, and

the bending tests only applied the axial portion of the stress to predict the fatigue life. A valuable research area is to expand the model to predict fatigue life based on shear stresses.

7.2.3 Future Applications

The capability to accurately predict the fatigue life of an AM component or to specify inspection criteria is great, however, this tool could be extremely powerful in the design phase. The application of a design life and defect distribution generates critical stresses and minimum defect sizes. The potential exists to apply those generated parameters into a multi-disciplinary optimization problem. The benefit would be an optimized print geometry that factors in load distributions and inspectable defect sizes. Optimizing to a fixed design life holds potential to further reduce the used material in any print. Tying the optimized geometry to a defect distribution creates links to optimal print parameters as well. Research into the multi-disciplinary optimization with the finite fatigue life El-Haddad model as an optimization function will enable cheap, limited function components with pre-determined inspection criteria to certify.

Appendix A. Matlab Code

1.1 Master Code

```
%% Maj Daniel Miller
% Master script for reading and processing Abaqus Mesh to interact with
% Fatigue Life Predictions

% Section 1) Structure Abaqus Data Files to be read in. Each row in the
% name files denotes a separate model to be processed.  ID the desired
% save names for the workspaces (Blade Data, Gauge Data)
% Custom Functions: None

% Section 2) Load the material properties: Basquin Equation Values and
% Crack Growth Values.
% Custom Functions: None

% Section 3) Generate the El-Haddad Finite Fatigue Life Model.
% Custom Functions: ElHaddadModel

% Section 4) Start of Blade Iteration For Loop.  Includes Sections 5-11.
% Iterates through each model data set called in Section 1.
% Custom Functions: None

% Section 5) Reads in the Mesh Connectivity (Element/Node Map), Element
% Volumes, Stress Map and Strain Map for the FEM Load Case.  ...
   Hardcoded to
% convert from inches to microns, inches^3 to microns^3 and psi to MPa
% respectivly.
% Custom Functions: ReadAbaqusMesh, ReadAbaqusStress
```

```
% Section 6) Splits the FEM model to remove un-nessesary elements.
% Function has a hardcoded separation plane to remove the structure grip
% from the blade.
% Custom Functions: PullBladeMesh

% Section 7) IDs the origin point for the FEM model being processed.
% Custom Functions: None

% Section 8) Convert stress and strain values from element values to ...
   nodal
% values.
% Custom Functions: NodalStressStrain

% Section 9) Pull all of the surface nodes in the model through an
% excel spreadsheet that pre-IDs the surface node desigation numbers.
% Custom Functions: None

% Section 10) Scale the nominal stress and strain values by the ...
   target life
% value for each model.
% Custom Functions: StressScaling

% Section 11) Stores the variables: BladeMesh, Mesh, Scale, Surface, and
% Origin into a super-structure.
% Custom Functions: None

% Section 12) Identify the nominal model values associated with a ...
   surface
% point to correspond with an applied strain gauge.
% Custom Functions: GaugeLocation
```

```
% Section 13) Develop and apply the scale factor to transform the ...
    nominal
% stress and strain values to match the experimental strain gauge ...
    values.
% Custom Functions: None

% Section 14) Save the workspaces for Blade Data and Gauge Data
% Custom Functions: None

clear all; close all; clc; %#ok<CLALL>
fprintf('Starting Master File \n');
fprintf(['Time Stamp: ',datestr(now,'HH:MM:SS'),'\n']);

%% 1) Model Files and Save Files

% Abaqus.inp file converted to Abaqus.txt
% Nodes Format: ID | X | Y | Z
% Element Format: ID | Node #1 | Node #2 | ... | Node #19 | Node #20
MeshFileName = ["Blade01_Quad_Morphed_Meas_TopBottomBC"; ...
    "Blade02_Quad_Morphed_Meas_TopBottomBC";...
                "Blade03_Quad_Morphed_Meas_TopBottomBC"; ...
                    "Blade04_Quad_Morphed_Meas_TopBottomBC";...
                "Blade05_Quad_Morphed_Meas_TopBottomBC"; ...
                    "Blade06_Quad_Morphed_Meas_TopBottomBC";...
                "Blade07_Quad_Morphed_Meas_TopBottomBC"; ...
                    "Blade08_Quad_Morphed_Meas_TopBottomBC";...
                "Blade09_Quad_Morphed_Meas_TopBottomBC"; ...
                    "Blade10_Quad_Morphed_Meas_TopBottomBC"];

% Abaqus.rpt files converted to Abaqus.txt
% Format: Element # | Von Mises | S11 | S22 | S33 | S12 | S13 | S23
```

```
StressFileName = ["Blade01_Freq2_MP_TBC_StressCentroid"; ...
    "Blade02_Freq2_MP_TBC_StressCentroid";...
                    "Blade03_Freq2_MP_TBC_StressCentroid"; ...
                        "Blade04_Freq2_MP_TBC_StressCentroid";...
                    "Blade05_Freq2_MP_TBC_StressCentroid"; ...
                        "Blade06_Freq2_MP_TBC_StressCentroid";...
                    "Blade07_Freq2_MP_TBC_StressCentroid"; ...
                        "Blade08_Freq2_MP_TBC_StressCentroid";...
                    "Blade09_Freq2_MP_TBC_StressCentroid"; ...
                        "Blade10_Freq2_MP_TBC_StressCentroid"];

% Format: Element # | Max Principle | E11 | E22 | E33 | E12 | E13 | E23
StrainFileName = ["Blade01_Freq2_MP_TBC_StrainCentroid"; ...
    "Blade02_Freq2_MP_TBC_StrainCentroid";...
                    "Blade03_Freq2_MP_TBC_StrainCentroid"; ...
                        "Blade04_Freq2_MP_TBC_StrainCentroid";...
                    "Blade05_Freq2_MP_TBC_StrainCentroid"; ...
                        "Blade06_Freq2_MP_TBC_StrainCentroid";...
                    "Blade07_Freq2_MP_TBC_StrainCentroid"; ...
                        "Blade08_Freq2_MP_TBC_StrainCentroid";...
                    "Blade09_Freq2_MP_TBC_StrainCentroid"; ...
                        "Blade10_Freq2_MP_TBC_StrainCentroid"];

% Format: Element # | Ele Volume
VolumeFileName = ["Blade01_Freq2_EleVolume_Base"; ...
    "Blade02_Freq2_EleVolume_Base";...
                    "Blade03_Freq2_EleVolume_Base"; ...
                        "Blade04_Freq2_EleVolume_Base";...
                    "Blade05_Freq2_EleVolume_Base"; ...
                        "Blade06_Freq2_EleVolume_Base";...
                    "Blade07_Freq2_EleVolume_Base"; ...
                        "Blade08_Freq2_EleVolume_Base";...
```

```
                    "Blade09_Freq2_EleVolume_Base"; ...
                        "Blade10_Freq2_EleVolume_Base"];

% Master Blade Save Name
SaveFile = 'AllBlades_Quad_Morphed_Meas_TopBottomBC.mat';
% Master Gauge Save Name
GaugeSave = 'AllBlades_Primary_Secondary_StrainGauges.mat';

%% 2) Material Properties for IN718
% Properties based on Sheridan's Paper: A Modified El Haddad Model For
% Versatile Defect Tolerant Design

% Loading and Shape Factors
Mat.R = -1; % Load Ratio (S_max/S_min)
Mat.Y1 = 1.12; % Crack Shape Factor (through crack at edge)
Mat.Y2 = 0.65; % Near surface pore

% Wroght IN718 Crack Growth Material Properties
Mat.A = 4623.4; % Material constant
Mat.b = -0.1558; % Material constant
Mat.gamma = 0.3727; % Material constant
Mat.C = 1e-13; % Material constant
Mat.n = 4; % Material constant
Mat.m = 0.75; % Material constant
Mat.K_Ic = 50; % Material constant (MPa*sqrt(m))

Mat.C_0 = Mat.C/(1-Mat.R)^(Mat.n*Mat.m);

fprintf('Finished Inputing Material Properties \n');
fprintf(['Time Stamp: ',datestr(now,'HH:MM:SS'),'\n']);

%% 3) Generate El-Haddad Model
```

```
% Applied the crack growth and Basquin Equation material properties to
% generate a finite life El-Haddad curve with the parameters of desired
% life, crack size, and applied stress.

Model = ElHaddadModel(Mat);
fprintf('Finished calculating El-Haddad Finite Fatigue Life \n');
fprintf(['Time Stamp: ',datestr(now,'HH:MM:SS'),'\n']);

%% 4) Start of Blade For Loop

for jj = 1:length(MeshFileName)

%% 5) Read in Mesh Data
% Name of file to read in, make sure to save the Abaqus input file ...
    as .txt
% first

% Reads in every node and element
% Mesh Input Units: inches
% Inputs: Mesh Name, Nodes Per Element
[Mesh.Nodes, Mesh.Elements] = ReadAbaqusMesh(MeshFileName(jj),20);
Mesh.NumNodes = size(Mesh.Nodes,1);

% Re-shape the element matrix to put each element on one line
% needed due to Abaqus output formatting with Quad Hex elements
Mesh.Elements = Mesh.Elements';
Mesh.Elements = Mesh.Elements(:);
Mesh.Elements = nonzeros(Mesh.Elements);
Mesh.NumEle = length(Mesh.Elements(:))/21;
Mesh.Elements = reshape(Mesh.Elements,21,Mesh.NumEle);
Mesh.Elements = Mesh.Elements';
% convert Node location from Inches to Microns
```

```
Mesh.Nodes(:,2:end) = Mesh.Nodes(:,2:end)*25400;
fprintf(['Finished Reading in the Mesh for Blade ...
    ',num2str(jj,'%02i'),' \n']);
fprintf(['Time Stamp: ',datestr(now,'HH:MM:SS'),'\n']);

% Read in element stress values
% Stress Input Units: psi
% Inputs: File Name, Number of columns in .txt file
Mesh.Freq2.Nom_Stress = ReadAbaqusStress(StressFileName(jj),8);
% Convert Stresses from psi to MPa
Mesh.Freq2.Nom_Stress(:,2:end) = ...
    Mesh.Freq2.Nom_Stress(:,2:end)*(0.00689476);
fprintf('Finished Reading in the Stress Map for Freq 2 \n');
fprintf(['Time Stamp: ',datestr(now,'HH:MM:SS'),'\n']);

% Pull elemental strain values
% Inputs: File Name, Number of columns in .txt file
Mesh.Freq2.Nom_Strain = ReadAbaqusStress(StrainFileName(jj),8);
fprintf('Finished Reading in the Strain Map for Freq 2 \n');
fprintf(['Time Stamp: ',datestr(now,'HH:MM:SS'),'\n']);

% Elemental Volume Data
% Volume Input Units: in^3
% Inputs: File Name, Number of columns in .txt file
Mesh.EleVolume = ReadAbaqusStress(VolumeFileName(jj),2);
% Convert from in^3 to micron^3
Mesh.EleVolume(:,2) = Mesh.EleVolume(:,2)*(25400^3);
fprintf('Finished Reading in the Element Volumes \n');
fprintf(['Time Stamp: ',datestr(now,'HH:MM:SS'),'\n']);

%% 6) Pull Blade Specific Data From Mesh
```

```
% Pull just the blade elements from the mesh to simplify plotting
% Function has the cutting plane hard coded inside (Line 17 of Function)
BladeMesh = PullBladeMesh(Mesh);
fprintf('Finished separating the Blade Mesh from Grip Mesh \n');
fprintf(['Time Stamp: ',datestr(now,'HH:MM:SS'),'\n']);

%% 7) Origin Location

% ID an origin location based on the lowest values of x, y, and z within
% the blade grip.
O_z = min(Mesh.Nodes(:,4));
[Ind_Oz,val] = find(Mesh.Nodes(:,4)<=(O_z+10)*10);
O_x = min(Mesh.Nodes(Ind_Oz,2));
O_y = min(Mesh.Nodes(Ind_Oz,3));

BladeMesh.Origin = [O_x, O_y, O_z];

fprintf('Finished IDing Model Origin Location \n');
fprintf(['Time Stamp: ',datestr(now,'HH:MM:SS'),'\n']);

%% 8) ID Nominal Max Stress & Stress Range at Each Node

% Pull the elemental stress and strain values that touch one node.  ...
    Store
% the largest value as the nodal stress/strain values.
BladeMesh = NodalStressStrain(BladeMesh);
BladeMesh.Freq2.Nom_NodalStressRange = BladeMesh.Freq2.Nom_NodalStress;
BladeMesh.Freq2.Nom_NodalStressRange(:,2:end) = ...
    (1-Mat.R)*BladeMesh.Freq2.Nom_NodalStress(:,2:end);

fprintf('Finished Generating Nominal Nodal Stress Values \n');
fprintf(['Time Stamp: ',datestr(now,'HH:MM:SS'),'\n']);
```

```
%% 9) Surface Mapping

% Pull the node map and stress/strain values associated with every ...
   surface
% node.

% Read in Surface Node IDs
SurfaceNodeIDs = xlsread('SurfaceNodes.xlsx');

fprintf('Finished Loading Surface Node IDs \n');
fprintf(['Time Stamp: ',datestr(now,'HH:MM:SS'),'\n']);

% Create array of surface node info
SurfaceMembership = ismember(BladeMesh.Nodes(:,1),SurfaceNodeIDs);
Surface.Nodes = [];
Surface.NodeStrain = [];

for ii = 1:BladeMesh.NumNodes
    if SurfaceMembership(ii) == 1
        Surface.Nodes = [Surface.Nodes; BladeMesh.Nodes(ii,:)];
        Surface.NodeStrain = [Surface.NodeStrain; ...
           BladeMesh.Freq2.Nom_NodalStrain(ii,:)];
    end
end

fprintf('Finished IDing Surface Node Location and Strain \n');
fprintf(['Time Stamp: ',datestr(now,'HH:MM:SS'),'\n']);

%% 10) Scale Stress Map by desired defect free life
```

```
% Use target life and Basquin Law to predict the max stress for the ...
    design
% life.  Design Max Stress / Nominal Max stress = Model Scale Value. ...
     Apply
% the scale value to saved nominal stress/strain values.

% Desired Defect Free Design Life
TargetLife = [1e6; 5e5; 1e6; 1e7; 1e5; 5e6; 5e6; 1e7; 5e5; 1e5];

[BladeMesh, BladeMesh.Freq2.Mod_Scale] = ...
    StressScaling(BladeMesh,Mat,TargetLife(jj));

fprintf('Finished Scaling the Blade Stress Map and Defect Stress ...
    Values \n');
fprintf(['Time Stamp: ',datestr(now,'HH:MM:SS'),'\n']);

%% 11) Store Data in SuperStructure

Mod_Blades{jj,1} = BladeMesh;
Mod_Mesh{jj,1} = Mesh;
Mod_Surface{jj,1} = Surface;

% Clear variables to prevent rollover artificats between modeling being
% processed.
clear BladeMesh Mesh Surface

end

%% 12) ID Gauge Locations

% Pick measure distances for where to place a gauge.  Apply the ...
    distances
```

```
% to the model surface to identify nodal location and associated
% stress/strain.
% Note: GaugeLocation is hardcoded for the applied turbine blade ...
    geometry.

% Measure Left from Right Edge
ML = 26400; % microns
% Measure Down from Top Edge
MD = 32200; % microns
PrimeGauge = GaugeLocation(ML,MD,Mod_Surface);
PrimeGauge.MaxStrain(jj,:) = ...
    max(Mod_Blades{jj,1}.Freq2.Nom_NodalStrain(:,2:5));

% Measure Left from Right Edge
ML = 31000; % microns
% Measure Down from Top Edge
MD = 86000; % microns
SecondGauge = GaugeLocation(ML,MD,Mod_Surface);
SecondGauge.MaxStrain(jj,:) = ...
    max(Mod_Blades{jj,1}.Freq2.Nom_NodalStrain(:,2:5));

fprintf(['Finished IDing Gauge Locations and Strains \n']);
fprintf(['Time Stamp: ',datestr(now,'HH:MM:SS'),'\n']);

%% 13) Experimental Strain Scaling

% Apply the measured strain at failure for both gauges
% Divide measured strain values by Model strain values at the gauge
% locations
% Average the scale factors for a single scale value per blade

% Failure Strain Values
```

```
PrimeGauge.FailureStrain = [1617.413; 1343.385; 1767.788; 965.448; ...
    1964.016; 1040.844; 1201.68; 1320.45; 1448.281; 2068.824]*1e-6;
SecondGauge.FailureStrain = [1159.531; 1068.243; 1362.922; 703.851; ...
    1471.868; 834.485; 1010.466; 1025.969; 1117.907; 1591.6]*1e-6;

% Calcuate Blade Scale Factor
G1_Ratio = PrimeGauge.FailureStrain./PrimeGauge.MeanStrain(:,4);
G2_Ratio = SecondGauge.FailureStrain./abs(SecondGauge.MeanStrain(:,4));

Exp_Scale = (G1_Ratio+G2_Ratio)./2;

% Scale Nominal Values to Experimental Scaling

for ii = 1:length(Mod_Blades)
    Mod_Blades{ii,1}.Freq2.Exp_NodalStress = ...
        Mod_Blades{ii,1}.Freq2.Nom_NodalStress;
    Mod_Blades{ii,1}.Freq2.Exp_NodalStress(:,2:end) = ...
        Mod_Blades{ii,1}.Freq2.Exp_NodalStress(:,2:end)*Exp_Scale(ii);

    Mod_Blades{ii,1}.Freq2.Exp_NodalStrain = ...
        Mod_Blades{ii,1}.Freq2.Nom_NodalStrain;
    Mod_Blades{ii,1}.Freq2.Exp_NodalStrain(:,2:end) = ...
        Mod_Blades{ii,1}.Freq2.Exp_NodalStrain(:,2:end)*Exp_Scale(ii);

    Mod_Blades{ii,1}.Freq2.Exp_Scale = Exp_Scale(ii);

end

%% 14) Save the Workspaces

save('El-Haddad_Model','Model')
```

```
save(SaveFile,'Mod_Blades','Mod_Mesh','Mod_Surface','Mat')
fprintf('Blade Workspace Saved \n');
fprintf(['Time Stamp: ',datestr(now,'HH:MM:SS'),'\n']);

save(GaugeSave,'PrimeGauge', 'SecondGauge')
fprintf('Gauge Values Saved \n');
fprintf(['Time Stamp: ',datestr(now,'HH:MM:SS'),'\n']);
```

1.1.1 El-Haddad Function

```
%% Maj Daniel Miller
% El-Haddad Fatigue Life Model

% Applies a material property set to a pre-set range of defect sizes and
% design lives.  Calculates the critical El-Haddad defect size and ...
   stress
% values.  Returns vectors for stess, defect size, and design life.

function Model = ElHaddadModel(Mat)

%% Input Parmeters
a = logspace(-7,-3,100); % Crack size of interest (meters)
N = logspace(3,7,100);  % Cycles to failure

%% Calculate dS

% Basquin Law with Walker Modification for stress ratio (R)
% Calculate applied stress range for per life and stress ratio
deltaS_N = (1-Mat.R) * Mat.A.*N.^Mat.b * ((1-Mat.R)/2)^(-Mat.gamma);

% fatal crack size
```

```
% Assuming any fatal crack will be a through crack
% Calculate failure crack size based on applied stress range
a_c = (1/pi)*(Mat.K_Ic*(1-Mat.R)/Mat.Y1./deltaS_N).^2;

% Paris Law
% Calculate starting crack size for given cycles to failure
a_0 = (a_c.^(1-Mat.n/2) - ...
    N.*((1-Mat.n/2)*Mat.C_0*(Mat.Y2*deltaS_N.*sqrt(pi)).^Mat.n)).^(1/(1-Mat.n/2));
% El-Haddad Equation
for ii = 1:length(deltaS_N)
    deltaS(ii,:) = deltaS_N(ii).*(sqrt(a_0(ii)./(a+a_0(ii))));
end

%% GridData
% Re-format the data for plotting

deltaS = deltaS';
deltaS_vector = deltaS(:);
a_vector = zeros(size(deltaS_vector'));
N_matrix = zeros(size(deltaS));

for ii = 1:100
    N_matrix(ii,:) = N;
end
N_vector = N_matrix(:);

for ii = 1:length(a)
    for jj = ii:100:length(deltaS_vector)
        a_vector(1,jj) = a(ii);
    end
end
```

```
Model.a_0 = a_0';
Model.deltaS_N = deltaS_N';
Model.a_N = a_vector';
Model.dS_N = deltaS_vector;
Model.N = N_vector;
end
```

1.1.2 Read Abaqus Mesh

```
%% Maj Daniel Miller
% Read in Abaqus Mesh Data

% Adapted from Mathworks question: Extract nodes and elements from ...
    abaqus
% input file to matlab
% https://www.mathworks.com/matlabcentral/answers/307258-extract- ...
% nodes-and-elements-from-abaqus-input-file-to-matlab

% Convert an Abaqus fileName.inp to fileName.txt and parses out node
% listings, locations, and element connection map
% Input: desired .inp file and an integer for the number of nodes per
% element
% Output: Matrix of Node IDs with locations, Matrix of Element IDs with
% nodal connections

% Runs a modified version of the Matlab function dlmread() called
% Moddlmread()

function [nodes, elements] = ReadAbaqusMesh(filename, NodesPerEle)
    fname = char(filename);
    fname = [fname,'.txt'];
```

```
    fid = fopen(fname,'rt');
    S = textscan(fid,'%s','Delimiter','\n');
    S = S{1} ;
    fclose(fid);
    %% Get the line number of mises
    idxN = strfind(S, 'Node');
    idx1 = find(not(cellfun('isempty', idxN)));
    idxE = strfind(S, 'Element');
    idx2 = find(not(cellfun('isempty', idxE)));
    idxElS = strfind(S, 'Elset');
    idx3 = find(not(cellfun('isempty',idxElS)));
    idxEnd = strfind(S, 'End');
    idx4 = find(not(cellfun('isempty', idxEnd)));

    %% pick  nodes
    nodes_temp = Moddlmread(fname,',',[idx1(1),0,idx2(1)-2,3]);
    nodes = zeros(nodes_temp(end,1),4);
    % space nodes to capture missing node indexes
    for ii = 1:length(nodes_temp)
        nodes(nodes_temp(ii,1),:) = nodes_temp(ii,:);
    end

    %% pick elements
    elements = Moddlmread(fname,',',[idx2(1),0,idx3(1)-2,NodesPerEle]);

end
```

1.1.3 Read Abaqus Stress

```
%% Maj Daniel Miller
% Read in Abaqus Stress Data
```

```
% convert fileName.rpt to fileName.txt
% Input: Name of File to be read, How many columns the output should ...
    have
% Output: Ele ID | Data column 1 | ... | Data column (Numcolumns-1)

% Runs a modified version of the Matlab function dlmread() called
% Moddlmread()

function stress = ReadAbaqusStress(filename,NumColumns)
    fname = char(filename);
    fname = [fname,'.txt'];
    fid = fopen(fname,'rt');
    S = textscan(fid,'%s','Delimiter','\n');
    S = S{1} ;
    fclose(fid);
    %% Get the line number of mises
    idxStart = strfind(S, '-----');
    idx1 = find(not(cellfun('isempty', idxStart)));
    idxEnd = strfind(S, 'Minimum');
    idx2 = find(not(cellfun('isempty', idxEnd)));

    %% pick elements
    stress = Moddlmread(fname,' ',[idx1(2),0,idx2-4,74]);
    zeroStress = [];
    v = nonzeros(stress');
    if v(1)==1 && v(2)==2
        v = [v(1);zeros(NumColumns-1,1);v(2:end)];
    end

    for ii = 9:length(v)-1
        if v(ii)==v(ii+1)-1 && v(ii)==v(ii-NumColumns)+1 && ...
```

```
            v(ii)~=v(ii+NumColumns)-1
             v = [v(1:ii);zeros(NumColumns-1,1);v(ii+1:end)];
             zeroStress = [zeroStress;ii,v(ii)];
        end
    end

    stress = reshape(v,NumColumns,length(stress))';


end
```

1.1.4 Modified dlmread File

```
% Added range(4) = size(result,2)-1; to correctly set the fourth range
% valuve (Line 156)

function result= dlmread(filename,delimiter,r,c,range)
%DLMREAD Read ASCII delimited file.
%   RESULT = DLMREAD(FILENAME) reads numeric data from the ASCII
%   delimited file FILENAME.  The delimiter is inferred from the ...
   formatting
%   of the file.
%
%   RESULT = DLMREAD(FILENAME,DELIMITER) reads numeric data from the ...
   ASCII
%   delimited file FILENAME using the delimiter DELIMITER.  The ...
   result is
%   returned in RESULT.  Use '\t' to specify a tab.
%
%   When a delimiter is inferred from the formatting of the file,
%   consecutive whitespaces are treated as a single delimiter.  By
```

```
%   contrast, if a delimiter is specified by the DELIMITER input, any
%   repeated delimiter character is treated as a separate delimiter.
%
%   RESULT = DLMREAD(FILENAME,DELIMITER,R,C) reads data from the
%   DELIMITER-delimited file FILENAME.  R and C specify the row R ...
   and column
%   C where the upper-left corner of the data lies in the file.  R ...
   and C are
%   zero-based so that R=0 and C=0 specifies the first value in the ...
   file.
%
%   All data in the input file must be numeric. DLMREAD does not operate
%   on files containing nonnumeric data, even if the specified rows and
%   columns for the read contain numeric data only.
%
%   RESULT = DLMREAD(FILENAME,DELIMITER,RANGE) reads the range specified
%   by RANGE = [R1 C1 R2 C2] where (R1,C1) is the upper-left corner of
%   the data to be read and (R2,C2) is the lower-right corner.  RANGE
%   can also be specified using spreadsheet notation as in RANGE = ...
   'A1..B7'.
%
%   DLMREAD fills empty delimited fields with zero.  Data files where
%   the lines end with a non-whitespace delimiter will produce a ...
   result with
%   an extra last column filled with zeros.
%
%   See also DLMWRITE, CSVREAD, TEXTSCAN, LOAD.

% Obsolete syntax:
%   RESULT= DLMREAD(FILENAME,DELIMITER,R,C,RANGE) reads only the ...
   range specified
%   by RANGE = [R1 C1 R2 C2] where (R1,C1) is the upper-left corner of
```

```
%   the data to be read and (R2,C2) is the lower-right corner.  RANGE
%   can also be specified using spreadsheet notation as in RANGE = ...
    'A1..B7'.
%   A warning will be generated if R,C or both don't match the upper
%   left corner of the RANGE.

%   Copyright 1984-2015 The MathWorks, Inc.

% Validate input args
fid = -1;
if nargin==0
    error(message('MATLAB:dlmread:Nargin'));
end

% Get Filename
if ~ischar(filename) && ~(isstring(filename) && isscalar(filename))
    error(message('MATLAB:dlmread:InvalidInputType'));
end
filename = char(filename);

% Get Delimiter
if nargin==1 % Guess default delimiter
    [fid, theMessage] = fopen(filename);
    if fid < 0
        error(message('MATLAB:dlmread:FileNotOpened', filename, ...
            theMessage));
    end
    str = fread(fid, 4096,'*char')';
    frewind(fid);
    delimiter = guessdelim(str);
    if isspace(delimiter);
        delimiter = '';
```

```
    end
else
    delimiter = sprintf(delimiter); % Interpret \t (if necessary)
    delimiter = char(delimiter);
end
if length(delimiter) > 1,
    error(message('MATLAB:dlmread:InvalidDelimiter'));
end

% Get row and column offsets
offset = 0;
if nargin<=2, % dlmread(file) or dlmread(file,dim)
    r = 0;
    c = 0;
    nrows = -1; % Read all rows
    range = [];
elseif nargin==3, % dlmread(file,delimiter,range)
    range = r;
    if ischar(range) || (isstring(range) && isscalar(range))
        range = char(range);
        range = local_str2rng(range);
    elseif length(r)==1 % Catch obsolete syntax ...
       dlmread(file,delimiter,r)
        warning(message('MATLAB:dlmread:ObsoleteSyntax'));
        result= dlmread(filename,delimiter,r,0);
        return
    end
    r = range(1);
    c = range(2);
    nrows = range(3) - range(1) + 1;
elseif nargin==4, % dlmread(file,delimiter,r,c)
    nrows = -1; % Read all rows
```

```
    range = [];
elseif nargin==5, % obsolete syntax dlmread(file,delimiter,r,c,range)
    if ischar(range) || (isstring(range) && isscalar(range))
        range = char(range);
        range = local_str2rng(range);
    end
    rold = r; cold = c;
    if r > range(3) || c > range(4), result= []; return, end
    if r ~= range(1) || c ~= range(2)
        warning(message('MATLAB:dlmread:InvalidRowsAndColumns'))
        offset = 1;
    end
    % For compatibility
    r = max(range(1),r);
    c = max(range(2),c);
    nrows = range(3) - r + 1;
end

% attempt to open data file
if fid == -1
    [fid, theMessage] = fopen(filename);
    if fid < 0
        error(message('MATLAB:dlmread:FileNotOpened', filename, ...
            theMessage));
    end
end

% Read the file using textscan
try
    tsargs = {...
        'HeaderLines',r,...
        'HeaderColumns',c,...
```

```
        'ReturnOnError',false,...
        'EmptyValue',0,...
        'CollectOutput',true,...
        'EndOfLine','\r\n'};

    if ~isempty(delimiter)
        delimiter = sprintf(delimiter);
        delimiter = char(delimiter);
        whitespace = setdiff(sprintf(' \b\t'),delimiter);
        tsargs = [tsargs, ...
            {'Delimiter',delimiter,'Whitespace',whitespace}];
    end

    result  = textscan(fid,'',nrows,tsargs{:});

catch exception
    fclose(fid);
    throw(exception);
end

% close data file
fclose(fid);
result = result{1};
range(4) = size(result,2)-1;
% textscan only trims leading columns, trailing columns may need ...
   clipping
if ~isempty(range)
    ncols = range(4) - range(2) + 1;

    % adjust ncols if necessary
    if ncols ~= size(result,2)
        result= result(:,1:ncols);
```

```
    end
end

% num rows should be correct, textscan clips
if nrows > 0 && nrows ~= size(result,1)
    error(message('MATLAB:dlmread:InternalSizeMismatch'))
end


% When passed in 5 args, we have an offset and a range.  If the ...
   offset is
% not equal to the top left corner of the range the user wanted to read
% range Ai..Bj and start looking in that matrix at rold and cold.  For
% backwards compatibility we create a result the same size as the ...
   specified
% range and place the data in the result at the requested offset.

% For example, given a file with [1 2 3; 4 5 6], reading A1..C2 with ...
   offset
% 1,2 produces this result:
% 0 0 0
% 0 5 6

if nargin==5 && offset
    rowIndex = rold+1:rold+nrows;
    columnIndex = cold+1:cold+ncols;
    if rold == 0
        rowIndex = rowIndex + 1;
    end
    if cold == 0
        columnIndex = columnIndex + 1;
    end
```

```
    % assign into a new matrix of the desired size
    % need to create temp matrix here cuz we want the
    % offset region filled with zeros
    new_result(rowIndex,columnIndex) = result;
    result = new_result;
end

function m=local_str2rng(str)
    m = [];

    % convert to upper case
    str = upper(str);

    % parse the upper-left and bottom-right cell locations
    k = strfind(str,'..');
    if length(k)~=1, return; end % Couldn't find '..'

    ulc = str(1:k-1);
    brc = str(k+2:end);

    % get upper-left col
    k = find(~isletter(ulc), 1 );
    if isempty(k) || k<2, return; end
    topl(2) = sum(cumprod([1 26*ones(1,k-2)]).*(ulc(k-1:-1:1)-'A'+1))-1;
    topl(1) = str2double(ulc(k:end))-1;

    % get bottom-right col
    k = find(~isletter(brc), 1 );
    if isempty(k) || k<2, return; end
    botr(2) = sum(cumprod([1 26*ones(1,k-2)]).*(brc(k-1:-1:1)-'A'+1))-1;
    botr(1) = str2double(brc(k:end))-1;
```

```
    m=[topl botr];
```

1.1.5 Separate Blade Mesh

```
%% Maj Daniel Miller
% Separate the Abaqus Mesh File

% Creates a cutting plane, and separates the FEM data (Lines 14 & 15)
% Removed majority of the FEM data to improve processing speeds

function BladeMesh = PullBladeMesh(Mesh)

BladeElements = [];
BladeVolume = [];
BladeEleStress = [];
BladeEleStrain = [];
% Plane equation in microns
NodeLocation = 541784032*Mesh.Nodes(:,2) - 1870964000*Mesh.Nodes(:,4);
NodeLocation = find(NodeLocation<= -71096632000000);

BladeNodes = Mesh.Nodes(NodeLocation,:);

for ii = 1:Mesh.NumEle
    if sum(ismember(Mesh.Elements(ii,2:end),NodeLocation)>0)
        BladeElements = [BladeElements;Mesh.Elements(ii,:)];
        BladeVolume = [BladeVolume;Mesh.EleVolume(ii,:)];
        BladeEleStress = [BladeEleStress;Mesh.Freq2.Nom_Stress(ii,:)];
        BladeEleStrain = [BladeEleStrain;Mesh.Freq2.Nom_Strain(ii,:)];
    end
end
```

```
BladeMesh.NumNodes = length(BladeNodes);
BladeMesh.NumEle = length(BladeElements);
BladeMesh.Nodes = BladeNodes;
BladeMesh.Elements = BladeElements;
BladeMesh.EleVolume = BladeVolume;
BladeMesh.Freq2.Nom_Stress = BladeEleStress;
BladeMesh.Freq2.Nom_Strain = BladeEleStrain;

end
```

1.1.6 ID Nodal Stress and Strain Values

```
%% Maj Daniel Miller
% Find Max Stress touching each Node

function Mesh = NodalStressStrain(Mesh)

Stress = zeros(Mesh.NumNodes,4);
Strain = Stress;

for ii = 1:Mesh.NumNodes
    [row,col] = find(Mesh.Elements(:,2:end)==Mesh.Nodes(ii,1));
    TempStress = Mesh.Freq2.Nom_Stress(row,2:5);
    [x,Ind] = max(TempStress(:,1));
    Stress(ii,:) = TempStress(Ind,:);
    TempStrain = Mesh.Freq2.Nom_Strain(row,2:5);
    [x,Ind] = max(TempStrain(:,1));
    Strain(ii,:) = TempStrain(Ind,:);
    Mesh.NodalNearElements{ii,1} = Mesh.Elements(row,:);
end
```

```
Mesh.Freq2.Nom_NodalStress = [Mesh.Nodes(:,1), Stress];
Mesh.Freq2.Nom_NodalStrain = [Mesh.Nodes(:,1), Strain];

end
```

1.1.7 Scale the Stress

```
%% Maj Daniel Miller
% Scale the max stress and stress range on BladeMesh and Defects ...
    according
% to the desired defect free system life

% Abaqus vibrational analysis normalizes the stress and strain values
% This function predictes the peak stress based on the Basquin Equantion
% and scales the stress and strain based on the predicted value.

%%
function [BladeMesh, Scale] = StressScaling(BladeMesh, Mat, TargetLife)

BladeMesh.Freq2.TargetLife = TargetLife;

BladeMesh.Freq2.dS_Target = ...
    (1-Mat.R)*Mat.A*BladeMesh.Freq2.TargetLife.^Mat.b;
Scale = ...
    BladeMesh.Freq2.dS_Target/(max(BladeMesh.Freq2.Nom_Stress(:,2))*2); ...
    % Scale by Von Mises Stress

BladeMesh.Freq2.Scale_Stress = BladeMesh.Freq2.Nom_Stress;
BladeMesh.Freq2.Scale_Stress(:,2:end) = ...
    BladeMesh.Freq2.Nom_Stress(:,2:end)*Scale;
```

```
BladeMesh.Freq2.Scale_Strain = BladeMesh.Freq2.Nom_Strain;
BladeMesh.Freq2.Scale_Strain(:,2:end) = ...
    BladeMesh.Freq2.Nom_Strain(:,2:end)*Scale;

BladeMesh.Freq2.Scale_NodalStress = BladeMesh.Freq2.Nom_NodalStress;
BladeMesh.Freq2.Scale_NodalStress(:,2:end) = ...
    BladeMesh.Freq2.Nom_NodalStress(:,2:end)*Scale;

BladeMesh.Freq2.Scale_NodalStrain = BladeMesh.Freq2.Nom_NodalStrain;
BladeMesh.Freq2.Scale_NodalStrain(:,2:end) = ...
    BladeMesh.Freq2.Nom_NodalStrain(:,2:end)*Scale;

BladeMesh.Freq2.Scale_NodalStressRange = ...
    BladeMesh.Freq2.Nom_NodalStressRange;
BladeMesh.Freq2.Scale_NodalStressRange(:,2:end) = ...
    BladeMesh.Freq2.Nom_NodalStressRange(:,2:end)*Scale;

end
```

1.1.8 Analyze Gauge Locations

```
%% Maj Daniel Miller
% Assessment of Strain Gauge Quality at one point across all blades

function CommonGauge = GaugeLocation(ML,MD,All_Surface)

r_target = 2000;

for jj = 1:length(All_Surface)
```

```
%% Measure Placement from top
Top = max(All_Surface{jj,1}.Nodes(:,4));

ind = find(All_Surface{jj,1}.Nodes(:,4)>0.999*Top);
Mean_Top = mean(All_Surface{jj,1}.Nodes(ind,4));

Z_coord = Mean_Top - MD;

%% Measure Placement from Right
ind = find(All_Surface{jj,1}.Nodes(:,4)>Z_coord*0.9 & ...
    All_Surface{jj,1}.Nodes(:,4)<Z_coord*1.1);
MinX = min(All_Surface{jj,1}.Nodes(ind,2));
index = find(All_Surface{jj,1}.Nodes(ind,2)<(MinX+0.1*MinX));

Mean_X = mean(All_Surface{jj,1}.Nodes(ind(index),2));
Mean_Y = mean(All_Surface{jj,1}.Nodes(ind(index),3));

theta_temp = [];
D2TS = [];

% Search Algorithm to find angle to top surface
theta_temp(1) = 0.8;
X_coord = ML/sqrt(1+tan(theta_temp(end))^2) + Mean_X;
Y_coord = (X_coord-Mean_X)*tan(theta_temp(end)) + Mean_Y;

r = sqrt((All_Surface{jj,1}.Nodes(:,2)-X_coord).^2 ...
       + (All_Surface{jj,1}.Nodes(:,3)-Y_coord).^2 ...
       + (All_Surface{jj,1}.Nodes(:,4)-Z_coord).^2);
D2TS(1) = min(r);
theta_temp(2) = theta_temp(end)-0.01;
X_coord = ML/sqrt(1+tan(theta_temp(end))^2) + Mean_X;
Y_coord = (X_coord-Mean_X)*tan(theta_temp(end)) + Mean_Y;
```

```
r = sqrt((All_Surface{jj,1}.Nodes(:,2)-X_coord).^2 ...
       + (All_Surface{jj,1}.Nodes(:,3)-Y_coord).^2 ...
       + (All_Surface{jj,1}.Nodes(:,4)-Z_coord).^2);
D2TS(2) = min(r);
while D2TS(end)<D2TS(end-1)
    theta_temp(end+1) = theta_temp(end)-0.01;
    X_coord = ML/sqrt(1+tan(theta_temp(end))^2) + Mean_X;
    Y_coord = (X_coord-Mean_X)*tan(theta_temp(end)) + Mean_Y;

    r = sqrt((All_Surface{jj,1}.Nodes(:,2)-X_coord).^2 ...
           + (All_Surface{jj,1}.Nodes(:,3)-Y_coord).^2 ...
           + (All_Surface{jj,1}.Nodes(:,4)-Z_coord).^2);
    D2TS(end+1) = min(r);
end
theta_L = theta_temp(end-2);
theta_U = theta_temp(end);
D2TS_L = D2TS(end-2);
D2TS_U = D2TS(end);
Interval = abs(theta_L - theta_U);

while Interval>0.0001
    theta_a = theta_L-0.33*Interval;
    theta_b = theta_L-0.66*Interval;

    X_coord = ML/sqrt(1+tan(theta_a)^2) + Mean_X;
    Y_coord = (X_coord-Mean_X)*tan(theta_a) + Mean_Y;

    r = sqrt((All_Surface{jj,1}.Nodes(:,2)-X_coord).^2 ...
           + (All_Surface{jj,1}.Nodes(:,3)-Y_coord).^2 ...
           + (All_Surface{jj,1}.Nodes(:,4)-Z_coord).^2);
    D2TS_a = min(r);
```

```
    X_coord = ML/sqrt(1+tan(theta_b)^2) + Mean_X;
    Y_coord = (X_coord-Mean_X)*tan(theta_b) + Mean_Y;

    r = sqrt((All_Surface{jj,1}.Nodes(:,2)-X_coord).^2 ...
           + (All_Surface{jj,1}.Nodes(:,3)-Y_coord).^2 ...
           + (All_Surface{jj,1}.Nodes(:,4)-Z_coord).^2);
    D2TS_b = min(r);


    if D2TS_a < D2TS_b
        theta_U = theta_b;
        Interval = abs(theta_L - theta_U);
    elseif D2TS_a > D2TS_b
        theta_L = theta_a;
        Interval = abs(theta_L - theta_U);
    else
        theta_L = theta_a;
        theta_U = theta_b;
        Interval = abs(theta_L - theta_U);
    end
end
theta = (theta_U + theta_L)/2;

indexes = find(r<=r_target);

NodeCluster = All_Surface{jj,1}.Nodes(indexes,:);
NodeStrains = All_Surface{jj,1}.NodeStrain(indexes,:);
StrainRange = ...
   abs(max(NodeStrains(:,2:end))-min(NodeStrains(:,2:end)));
MeanStrain = mean(NodeStrains(:,2:end));
```

```
    CommonGauge.Centroid(jj,:) = [X_coord,Y_coord,Z_coord];
    CommonGauge.theta(jj,:) = theta;
    CommonGauge.StrainRange(jj,:) = StrainRange;
    CommonGauge.MeanStrain(jj,:) = MeanStrain;
    CommonGauge.NodeCluster{jj,1} = NodeCluster;
    CommonGauge.NodeStrains{jj,1} = NodeStrains;

end

end
```

1.2 Defect Processing

```
%% Maj Daniel Miller
% Takes the meta-data files from the Mira SEM imager and translates the
% coordinates to the base coordinates for the part

% Needed Files: Data collection centered on the origin of the part ...
   and at
% known +X and +Y locations

% Data collection centered on the defects of interest

% SEM Table data denoting defect area

clear all; close all; clc;

%%
fprintf('SEM Defect Data Processing \n')
fprintf(['Time Stamp: ',datestr(now,'HH:MM:SS'),'\n']);
```

```
%% Load Blade Data

load AllBlades_Quad_Morphed_Meas_TopBottomBC.mat

fprintf('Loaded Blade Meshes \n');
fprintf(['Time Stamp: ',datestr(now,'HH:MM:SS'),'\n']);

%% Blade 01

% Blade 01 Grip Measurements (meters)
B01.X_Meas = 62.56/1000;
B01.Y_Meas = 18.75/1000;

% Copy over SEM data files and save as .txt files
% Read in SEM Data
FileName = 'Blade01_TiltRotate_Origin00-jpg';
B01.Origin = ReadSEMData(FileName);
FileName = 'Blade01_TiltRotate_+X00-jpg';
B01.XAxis = ReadSEMData(FileName);
FileName = 'Blade01_TiltRotate_+Y00-jpg';
B01.YAxis = ReadSEMData(FileName);

DefectNum = 68; % Final count of imaged defects
for ii = 0:DefectNum
    LocFileName = ['Blade01_LoFDefects_',num2str(ii,'%02i'),'-jpg'];
    B01.Defect{ii+1,1} = ReadSEMData(LocFileName);
    B01.Position(ii+1,:) = PositionTransform(B01,ii+1);

    DefFileName = ['Blade01_LoF',num2str(ii,'%02i'),'_Table'];
    [B01.DefectSize(ii+1,1), B01.ShapeFactor(ii+1,1)] = ...
       ReadSEMTable(DefFileName);
end
```

```
BladeNumber = 1;
B01.MeshOrigin = Mod_Blades{BladeNumber,1}.Origin'; % microns

% Map defect to closest FEM Node
% Map largest and smallest stress within a radius of the measured defect
% location
Radius = 500; % microns
B01 = MeasuredDefectMapping(B01,Mod_Blades{BladeNumber,1},Radius);

% Calculate predicted life for each defect size/stress combo
B01.min_Life = DefectStressSizetoLife(B01,'min',Mat);
B01.max_Life = DefectStressSizetoLife(B01,'max',Mat);
B01.Life = DefectStressSizetoLife(B01,'avg',Mat);

save('Blade01_MeasuredDefects.mat','B01')
fprintf(['Finished with Blade',num2str(BladeNumber,'%02i'),' Defects ...
    \n']);
fprintf(['Time Stamp: ',datestr(now,'HH:MM:SS'),'\n']);

%% Blade 02

% Blade 02 Grip Measurements (meters)
B02.X_Meas = 62.45/1000;
B02.Y_Meas = 18.81/1000;

% Copy over SEM data files and save as .txt files
% Read in SEM Data
FileName = 'Blade02_TiltRotate_Origin00-jpg';
B02.Origin = ReadSEMData(FileName);
FileName = 'Blade02_TiltRotate_+X00-jpg';
B02.XAxis = ReadSEMData(FileName);
```

```
FileName = 'Blade02_TiltRotate_+Y00-jpg';
B02.YAxis = ReadSEMData(FileName);

DefectNum = 20; % Final count of imaged defects
for ii = 0:DefectNum
    LocFileName = ['Blade02_LoFDefects_',num2str(ii,'%02i'),'-jpg'];
    B02.Defect{ii+1,1} = ReadSEMData(LocFileName);
    B02.Position(ii+1,:) = PositionTransform(B02,ii+1);

    DefFileName = ['Blade02_LoF',num2str(ii,'%02i'),'_Table'];
    [B02.DefectSize(ii+1,1), B02.ShapeFactor(ii+1,1)] = ...
        ReadSEMTable(DefFileName);
end

% Move data from second Blade 2 Set to first set
% Blade 02 Grip Measurements (meters)
B02_S2.X_Meas = 62.45/1000;
B02_S2.Y_Meas = 18.81/1000;
% Copy over SEM data files and save as .txt files
% Read in SEM Data
FileName = 'Blade02_Set2_TiltRotate_Origin00-jpg';
B02_S2.Origin = ReadSEMData(FileName);
FileName = 'Blade02_Set2_TiltRotate_+X00-jpg';
B02_S2.XAxis = ReadSEMData(FileName);
FileName = 'Blade02_Set2_TiltRotate_+Y00-jpg';
B02_S2.YAxis = ReadSEMData(FileName);

DefectNum = 0; % Final count of imaged defects
for ii = 0:DefectNum
    LocFileName = ...
        ['Blade02_Set2_LoFDefects_',num2str(ii,'%02i'),'-jpg'];
    B02_S2.Defect{ii+1,1} = ReadSEMData(LocFileName);
```

```
    B02_S2.Position(ii+1,:) = PositionTransform(B02_S2,ii+1);

    DefFileName = ['Blade02_Set2_LoF',num2str(ii,'%02i'),'_Table'];
    [B02_S2.DefectSize(ii+1,1), B02_S2.ShapeFactor(ii+1,1)] = ...
       ReadSEMTable(DefFileName);
end
B02.Defect(end+1,1) = B02_S2.Defect;
B02.Position(end+1,:) = B02_S2.Position;
B02.DefectSize(end+1,1) = B02_S2.DefectSize;
B02.ShapeFactor(end+1,1) = B02_S2.ShapeFactor;
clear B02_S2;

BladeNumber = 2;
B02.MeshOrigin = Mod_Blades{BladeNumber,1}.Origin'; % microns

% Map defect to closest FEM Node
% Map largest and smallest stress within a radius of the measured defect
% location
Radius = 500; % microns
B02 = MeasuredDefectMapping(B02,Mod_Blades{BladeNumber,1},Radius);

% Calculate predicted life for each defect size/stress combo
B02.min_Life = DefectStressSizetoLife(B02,'min',Mat);
B02.max_Life = DefectStressSizetoLife(B02,'max',Mat);
B02.Life = DefectStressSizetoLife(B02,'avg',Mat);

save('Blade02_MeasuredDefects.mat','B02')
fprintf(['Finished with Blade',num2str(BladeNumber,'%02i'),' Defects ...
   \n']);
fprintf(['Time Stamp: ',datestr(now,'HH:MM:SS'),'\n']);

%% Blade 03
```

```
% Blade 03 Grip Measurements (meters)
B03.X_Meas = 62.58/1000;
B03.Y_Meas = 18.77/1000;

% Copy over SEM data files and save as .txt files
% Read in SEM Data
FileName = 'Blade03_TiltRotate_Origin00-jpg';
B03.Origin = ReadSEMData(FileName);
FileName = 'Blade03_TiltRotate_+X00-jpg';
B03.XAxis = ReadSEMData(FileName);
FileName = 'Blade03_TiltRotate_+Y00-jpg';
B03.YAxis = ReadSEMData(FileName);

DefectNum = 23; % Final count of imaged defects
for ii = 0:DefectNum
    LocFileName = ['Blade03_LoFDefects_',num2str(ii,'%02i'),'-jpg'];
    B03.Defect{ii+1,1} = ReadSEMData(LocFileName);
    B03.Position(ii+1,:) = PositionTransform(B03,ii+1);

    DefFileName = ['Blade03_LoF',num2str(ii,'%02i'),'_Table'];
    [B03.DefectSize(ii+1,1), B03.ShapeFactor(ii+1,1)] = ...
       ReadSEMTable(DefFileName);
end

BladeNumber = 3;
B03.MeshOrigin = Mod_Blades{BladeNumber,1}.Origin'; % microns

% Map defect to closest FEM Node
% Map largest and smallest stress within a radius of the measured defect
% location
Radius = 500; % microns
```

```
B03 = MeasuredDefectMapping(B03,Mod_Blades{BladeNumber,1},Radius);

% Calculate predicted life for each defect size/stress combo
B03.min_Life = DefectStressSizetoLife(B03,'min',Mat);
B03.max_Life = DefectStressSizetoLife(B03,'max',Mat);
B03.Life = DefectStressSizetoLife(B03,'avg',Mat);

save('Blade03_MeasuredDefects.mat','B03')
fprintf(['Finished with Blade',num2str(BladeNumber,'%02i'),' Defects ...
    \n']);
fprintf(['Time Stamp: ',datestr(now,'HH:MM:SS'),'\n']);

%% Blade 04

% Blade 04 Grip Measurements (meters)
B04.X_Meas = 62.63/1000;
B04.Y_Meas = 18.77/1000;

% Copy over SEM data files and save as .txt files
% Read in SEM Data
FileName = 'Blade04_TiltRotate_Origin00-jpg';
B04.Origin = ReadSEMData(FileName);
FileName = 'Blade04_TiltRotate_+X00-jpg';
B04.XAxis = ReadSEMData(FileName);
FileName = 'Blade04_TiltRotate_+Y00-jpg';
B04.YAxis = ReadSEMData(FileName);

DefectNum = 84; % Final count of imaged defects
for ii = 0:DefectNum
    LocFileName = ['Blade04_LoFDefects_',num2str(ii,'%02i'),'-jpg'];
    B04.Defect{ii+1,1} = ReadSEMData(LocFileName);
    B04.Position(ii+1,:) = PositionTransform(B04,ii+1);
```

```
    DefFileName = ['Blade04_LoF',num2str(ii,'%02i'),'_Table'];
    [B04.DefectSize(ii+1,1), B04.ShapeFactor(ii+1,1)] = ...
        ReadSEMTable(DefFileName);
end

BladeNumber = 4;
B04.MeshOrigin = Mod_Blades{BladeNumber,1}.Origin'; % microns

% Map defect to closest FEM Node
% Map largest and smallest stress within a radius of the measured defect
% location
Radius = 500; % microns
B04 = MeasuredDefectMapping(B04,Mod_Blades{BladeNumber,1},Radius);

% Calculate predicted life for each defect size/stress combo
B04.min_Life = DefectStressSizetoLife(B04,'min',Mat);
B04.max_Life = DefectStressSizetoLife(B04,'max',Mat);
B04.Life = DefectStressSizetoLife(B04,'avg',Mat);

save('Blade04_MeasuredDefects.mat','B04')
fprintf(['Finished with Blade',num2str(BladeNumber,'%02i'),' Defects ...
   \n']);
fprintf(['Time Stamp: ',datestr(now,'HH:MM:SS'),'\n']);

%% Blade 05

% Blade 05 Grip Measurements (meters)
B05.X_Meas = 62.52/1000;
B05.Y_Meas = 18.78/1000;

% Copy over SEM data files and save as .txt files
```

```
% Read in SEM Data
FileName = 'Blade05_TiltRotate_Origin00-jpg';
B05.Origin = ReadSEMData(FileName);
FileName = 'Blade05_TiltRotate_+X01-jpg';
B05.XAxis = ReadSEMData(FileName);
FileName = 'Blade05_TiltRotate_+Y00-jpg';
B05.YAxis = ReadSEMData(FileName);

DefectNum = 30; % Final count of imaged defects
for ii = 0:DefectNum
    LocFileName = ['Blade05_LoFDefects_',num2str(ii,'%02i'),'-jpg'];
    B05.Defect{ii+1,1} = ReadSEMData(LocFileName);
    B05.Position(ii+1,:) = PositionTransform(B05,ii+1);

    DefFileName = ['Blade05_LoF',num2str(ii,'%02i'),'_Table'];
    [B05.DefectSize(ii+1,1), B05.ShapeFactor(ii+1,1)] = ...
       ReadSEMTable(DefFileName);
end

BladeNumber = 5;
B05.MeshOrigin = Mod_Blades{BladeNumber,1}.Origin'; % microns

% Map defect to closest FEM Node
% Map largest and smallest stress within a radius of the measured defect
% location
Radius = 500; % microns
B05 = MeasuredDefectMapping(B05,Mod_Blades{BladeNumber,1},Radius);

% Calculate predicted life for each defect size/stress combo
B05.min_Life = DefectStressSizetoLife(B05,'min',Mat);
B05.max_Life = DefectStressSizetoLife(B05,'max',Mat);
B05.Life = DefectStressSizetoLife(B05,'avg',Mat);
```

```
save('Blade05_MeasuredDefects.mat','B05')
fprintf(['Finished with Blade',num2str(BladeNumber,'%02i'),' Defects ...
    \n']);
fprintf(['Time Stamp: ',datestr(now,'HH:MM:SS'),'\n']);

%% Blade 06

% Blade 06 Grip Measurements (meters)
B06.X_Meas = 62.43/1000;
B06.Y_Meas = 18.77/1000;

% Copy over SEM data files and save as .txt files
% Read in SEM Data
FileName = 'Blade06_TiltRotate_Origin00-jpg';
B06.Origin = ReadSEMData(FileName);
FileName = 'Blade06_TiltRotate_+X00-jpg';
B06.XAxis = ReadSEMData(FileName);
FileName = 'Blade06_TiltRotate_+Y00-jpg';
B06.YAxis = ReadSEMData(FileName);

DefectNum = 50; % Final count of imaged defects
for ii = 0:DefectNum
    LocFileName = ['Blade06_LoFDefects_',num2str(ii,'%02i'),'-jpg'];
    B06.Defect{ii+1,1} = ReadSEMData(LocFileName);
    B06.Position(ii+1,:) = PositionTransform(B06,ii+1);

    DefFileName = ['Blade06_LoF',num2str(ii,'%02i'),'_Table'];
    [B06.DefectSize(ii+1,1), B06.ShapeFactor(ii+1,1)] = ...
        ReadSEMTable(DefFileName);
end
```

```
BladeNumber = 6;
B06.MeshOrigin = Mod_Blades{BladeNumber,1}.Origin'; % microns

% Map defect to closest FEM Node
% Map largest and smallest stress within a radius of the measured defect
% location
Radius = 500; % microns
B06 = MeasuredDefectMapping(B06,Mod_Blades{BladeNumber,1},Radius);

% Calculate predicted life for each defect size/stress combo
B06.min_Life = DefectStressSizetoLife(B06,'min',Mat);
B06.max_Life = DefectStressSizetoLife(B06,'max',Mat);
B06.Life = DefectStressSizetoLife(B06,'avg',Mat);

save('Blade06_MeasuredDefects.mat','B06')
fprintf(['Finished with Blade',num2str(BladeNumber,'%02i'),' Defects ...
    \n']);
fprintf(['Time Stamp: ',datestr(now,'HH:MM:SS'),'\n']);

%% Blade 07

% Blade 07 Grip Measurements (meters)
B07.X_Meas = 62.41/1000;
B07.Y_Meas = 18.77/1000;

% Copy over SEM data files and save as .txt files
% Read in SEM Data
FileName = 'Blade07_TiltRotate_Origin00-jpg';
B07.Origin = ReadSEMData(FileName);
FileName = 'Blade07_TiltRotate_+X00-jpg';
B07.XAxis = ReadSEMData(FileName);
FileName = 'Blade07_TiltRotate_+Y00-jpg';
```

```
B07.YAxis = ReadSEMData(FileName);

DefectNum = 58; % Final count of imaged defects
for ii = 0:DefectNum
    LocFileName = ['Blade07_LoFDefects_',num2str(ii,'%02i'),'-jpg'];
    B07.Defect{ii+1,1} = ReadSEMData(LocFileName);
    B07.Position(ii+1,:) = PositionTransform(B07,ii+1);

    DefFileName = ['Blade07_LoF',num2str(ii,'%02i'),'_Table'];
    [B07.DefectSize(ii+1,1), B07.ShapeFactor(ii+1,1)] = ...
       ReadSEMTable(DefFileName);
end

BladeNumber = 7;
B07.MeshOrigin = Mod_Blades{BladeNumber,1}.Origin'; % microns

% Map defect to closest FEM Node
% Map largest and smallest stress within a radius of the measured defect
% location
Radius = 500; % microns
B07 = MeasuredDefectMapping(B07,Mod_Blades{BladeNumber,1},Radius);

% Calculate predicted life for each defect size/stress combo
B07.min_Life = DefectStressSizetoLife(B07,'min',Mat);
B07.max_Life = DefectStressSizetoLife(B07,'max',Mat);
B07.Life = DefectStressSizetoLife(B07,'avg',Mat);

save('Blade07_MeasuredDefects.mat','B07')
fprintf(['Finished with Blade',num2str(BladeNumber,'%02i'),' Defects ...
   \n']);
fprintf(['Time Stamp: ',datestr(now,'HH:MM:SS'),'\n']);
```

```
%% Blade 08

% Blade 08 Grip Measurements (meters)
B08.X_Meas = 62.37/1000;
B08.Y_Meas = 18.75/1000;

% Copy over SEM data files and save as .txt files
% Read in SEM Data
FileName = 'Blade08_TiltRotate_Origin00-jpg';
B08.Origin = ReadSEMData(FileName);
FileName = 'Blade08_TiltRotate_+X00-jpg';
B08.XAxis = ReadSEMData(FileName);
FileName = 'Blade08_TiltRotate_+Y00-jpg';
B08.YAxis = ReadSEMData(FileName);

DefectNum = 23; % Final count of imaged defects
for ii = 0:DefectNum
    LocFileName = ['Blade08_LoFDefects_',num2str(ii,'%02i'),'-jpg'];
    B08.Defect{ii+1,1} = ReadSEMData(LocFileName);
    B08.Position(ii+1,:) = PositionTransform(B08,ii+1);

    DefFileName = ['Blade08_LoF',num2str(ii,'%02i'),'_Table'];
    [B08.DefectSize(ii+1,1), B08.ShapeFactor(ii+1,1)] = ...
       ReadSEMTable(DefFileName);
end

BladeNumber = 8;
B08.MeshOrigin = Mod_Blades{BladeNumber,1}.Origin'; % microns

% Map defect to closest FEM Node
% Map largest and smallest stress within a radius of the measured defect
% location
```

```
Radius = 500; % microns
B08 = MeasuredDefectMapping(B08,Mod_Blades{BladeNumber,1},Radius);

% Calculate predicted life for each defect size/stress combo
B08.min_Life = DefectStressSizetoLife(B08,'min',Mat);
B08.max_Life = DefectStressSizetoLife(B08,'max',Mat);
B08.Life = DefectStressSizetoLife(B08,'avg',Mat);

save('Blade08_MeasuredDefects.mat','B08')
fprintf(['Finished with Blade',num2str(BladeNumber,'%02i'),' Defects ...
    \n']);
fprintf(['Time Stamp: ',datestr(now,'HH:MM:SS'),'\n']);

%% Blade 09

% Blade 09 Grip Measurements (meters)
B09.X_Meas = 62.44/1000;
B09.Y_Meas = 18.76/1000;

% Copy over SEM data files and save as .txt files
% Read in SEM Data
FileName = 'Blade09_TiltRotate_Origin00-jpg';
B09.Origin = ReadSEMData(FileName);
FileName = 'Blade09_TiltRotate_+X00-jpg';
B09.XAxis = ReadSEMData(FileName);
FileName = 'Blade09_TiltRotate_+Y00-jpg';
B09.YAxis = ReadSEMData(FileName);

DefectNum = 34; % Final count of imaged defects
for ii = 0:DefectNum
    LocFileName = ['Blade09_LoFDefects_',num2str(ii,'%02i'),'-jpg'];
    B09.Defect{ii+1,1} = ReadSEMData(LocFileName);
```

```
    B09.Position(ii+1,:) = PositionTransform(B09,ii+1);

    DefFileName = ['Blade09_LoF',num2str(ii,'%02i'),'_Table'];
    [B09.DefectSize(ii+1,1), B09.ShapeFactor(ii+1,1)] = ...
       ReadSEMTable(DefFileName);
end

BladeNumber = 9;
B09.MeshOrigin = Mod_Blades{BladeNumber,1}.Origin'; % microns

% Map defect to closest FEM Node
% Map largest and smallest stress within a radius of the measured defect
% location
Radius = 500; % microns
B09 = MeasuredDefectMapping(B09,Mod_Blades{BladeNumber,1},Radius);

% Calculate predicted life for each defect size/stress combo
B09.min_Life = DefectStressSizetoLife(B09,'min',Mat);
B09.max_Life = DefectStressSizetoLife(B09,'max',Mat);
B09.Life = DefectStressSizetoLife(B09,'avg',Mat);

save('Blade09_MeasuredDefects.mat','B09')
fprintf(['Finished with Blade',num2str(BladeNumber,'%02i'),' Defects ...
   \n']);
fprintf(['Time Stamp: ',datestr(now,'HH:MM:SS'),'\n']);

%% Blade 10

% Blade 10 Grip Measurements (meters)
B10.X_Meas = 62.46/1000;
B10.Y_Meas = 18.74/1000;
```

```
% Copy over SEM data files and save as .txt files
% Read in SEM Data
FileName = 'Blade10_TiltRotate_Origin00-jpg';
B10.Origin = ReadSEMData(FileName);
FileName = 'Blade10_TiltRotate_+X00-jpg';
B10.XAxis = ReadSEMData(FileName);
FileName = 'Blade10_TiltRotate_+Y00-jpg';
B10.YAxis = ReadSEMData(FileName);

DefectNum = 41; % Final count of imaged defects
for ii = 0:DefectNum
    LocFileName = ['Blade10_LoFDefects_',num2str(ii,'%02i'),'-jpg'];
    B10.Defect{ii+1,1} = ReadSEMData(LocFileName);
    B10.Position(ii+1,:) = PositionTransform(B10,ii+1);

    DefFileName = ['Blade10_LoF',num2str(ii,'%02i'),'_Table'];
    [B10.DefectSize(ii+1,1), B10.ShapeFactor(ii+1,1)] = ...
       ReadSEMTable(DefFileName);
end

BladeNumber = 10;
B10.MeshOrigin = Mod_Blades{BladeNumber,1}.Origin'; % microns

% Map defect to closest FEM Node
% Map largest and smallest stress within a radius of the measured defect
% location
Radius = 500; % microns
B10 = MeasuredDefectMapping(B10,Mod_Blades{BladeNumber,1},Radius);

% Calculate predicted life for each defect size/stress combo
B10.min_Life = DefectStressSizetoLife(B10,'min',Mat);
B10.max_Life = DefectStressSizetoLife(B10,'max',Mat);
```

```
B10.Life = DefectStressSizetoLife(B10,'avg',Mat);

save('Blade10_MeasuredDefects.mat','B10')
fprintf(['Finished with Blade',num2str(BladeNumber,'%02i'),' Defects ...
    \n']);
fprintf(['Time Stamp: ',datestr(now,'HH:MM:SS'),'\n']);

%%
Mod_Defects{1,1} = B01;
Mod_Defects{2,1} = B02;
Mod_Defects{3,1} = B03;
Mod_Defects{4,1} = B04;
Mod_Defects{5,1} = B05;
Mod_Defects{6,1} = B06;
Mod_Defects{7,1} = B07;
Mod_Defects{8,1} = B08;
Mod_Defects{9,1} = B09;
Mod_Defects{10,1} = B10;

save('AllBlades_MeasuredDefects.mat','Mod_Defects')
fprintf('Finished saving Measured Defect Data \n');
fprintf(['Time Stamp: ',datestr(now,'HH:MM:SS'),'\n']);
```

1.2.1 Read SEM Data

```
%% Maj Daniel Miller

% SEM Image data to pull out tilt, WD, and X,Y,Z of image center
% SEM defaults to units of meters for distance and degrees for ...
    rotation, no
% unit conversion is applied
```

```
% Input: FileName of SEM image data
% Output: Defect Data Structure with variables for the SEM image
% coordinates (Meters, degrees)

%% Image Data Selection Function
function DefectData = ReadSEMData(filename)

% fileID = fopen('Blade05_LoFDefects_30_Mod-jpg.txt');
filename = char(filename);
fname = [filename,'.txt'];
fid = fopen(fname);
S = textscan(fid,'%s','Delimiter','\n');
S = S{1};
fclose(fid);
ind = find(S{55}=='=');
DefectData.Tilt = double(string(S{55}(ind+1:end)));
ind = find(S{56}=='=');
DefectData.X = double(string(S{56}(ind+1:end)));
ind = find(S{57}=='=');
DefectData.Y = double(string(S{57}(ind+1:end)));
ind = find(S{58}=='=');
DefectData.Z = double(string(S{58}(ind+1:end)));
ind = find(S{63}=='=');
DefectData.WD = double(string(S{63}(ind+1:end)));

end
```

1.2.2 Read SEM Table

```
%% Maj Daniel Miller
```

```
% Pull out defect size and depth from SEM Image processing Table data
% Process SEM image to generate a defect area, re-label defect area to
% 'LoFXX'.
% If the defect area contains any fracture regions, collect their
% area and re-label 'SX' for subtraction
% If Blade edge is visible in the image, measure the normal distance ...
   from
% blade edge to defect center, re-label 'Depth'

% The code scans the .txt files for the defect area: 'L', any ...
   reductions in
% area: 'S', and the depth from surface: 'D'.  If items are labeled
% differently, this code won't funciton correctly, and no errors ...
   will be
% reported

% Defect Size is assumed as square root of area ('L'-'S'), SEM table ...
   defaults to
% microns for measurement values.

% Shape Factor is 0.65 for a defect at the surface and 0.5 for a defect
% inside the structure based on the ratio of the defect radius (Size/2)
% divided by the depth ('D')

% Input: FileName for SEM table
% Output: Defect Size (microns), Shape Factor for each defect


%% Defect Size Selection Function
function [DefectSize, ShapeFactor] = ReadSEMTable(filename)
```

```
filename = char(filename);
fname = [filename,'.txt'];
fid = fopen(fname);
S = textscan(fid,'%s','Delimiter','\n');
S = S{1};
fclose(fid);

AreaSub = 0;
Depth = Inf;
for ii = 1:length(S)
    if S{ii}(1)=='S'
        values = regexp(S{ii},'\d*','Match');
        AreaSub = ...
            AreaSub+str2double(values{2})+str2double(values{3})/100;
    elseif S{ii}(1)=='L'
        values = regexp(S{ii},'\d*','Match');
        AreaDef = str2double(values{2})+str2double(values{3})/100;
    elseif S{ii}(1)=='D'
        values = regexp(S{ii},'\d*','Match');
        Depth = str2double(values{1})+str2double(values{2})/100;
    end
end

% Units: microns
DefectSize = sqrt(AreaDef - AreaSub);

Ratio = (DefectSize/2)/Depth;
if Ratio <0.8
    ShapeFactor = 0.5;
else
    ShapeFactor = 0.65;
end
```

```
end
```

1.2.3 Coordinate Transformation

```
%% Maj Daniel Miller

% Runs transformation to convert from SEM coordinate system to Blade
% coordinate system.

% Uses images aligned with the Blade Origin, at a known location ...
    along the
% blade X-Axis, and at a known location along the blde Y-Axis

% Measurement values generate a rotation angle to account for ...
    variations in
% the part placement in the SEM

% Measured Blade X & Y dimentions enable scaling of SEM measured ...
    values to
% the actual part dimentions

% Input: Blade (Measured Defect Structure), BladeIndex (which defect is
% being processed)
% Output: Calcluated defect location in Blade Coordinates (microns)

%% Coordinate Transform Function
function DefectLocation = PositionTransform(Blade,BladeIndex)

tilt = Blade.Origin.Tilt;
% Calculations
```

```
Rotation = atan2(Blade.XAxis.X-Blade.Origin.X,-1*...
                 (Blade.XAxis.Y-Blade.Origin.Y));

X_scale = Blade.X_Meas/(norm([Blade.XAxis.X;Blade.XAxis.Y]-...
                             [Blade.Origin.X;Blade.Origin.Y])*cosd(tilt));
Y_scale = Blade.Y_Meas/norm([Blade.YAxis.X;Blade.YAxis.Y]-...
                            [Blade.Origin.X;Blade.Origin.Y]);

% Units: Meters
X = ...
    X_scale*((Blade.Defect{BladeIndex}.X-Blade.Origin.X)*sin(Rotation)-...
              (Blade.Defect{BladeIndex}.Y-Blade.Origin.Y)*cos(Rotation))...
               *cosd(tilt);
Y = ...
    Y_scale*((Blade.Defect{BladeIndex}.X-Blade.Origin.X)*cos(Rotation)-...
              (Blade.Defect{BladeIndex}.Y-Blade.Origin.Y)*sin(Rotation))...
               + 0.0005; % adding 0.5 mm
Z = (Blade.Defect{end}.Z-Blade.Defect{BladeIndex}.WD)*cosd(tilt)...
     +0.012; % adding 12 mm

% Units: microns
DefectLocation = [X, Y, Z].*1e6;

end
```

1.2.4 Map Defects to FEM

```
%% Maj Daniel Miller
% Connect Measured Defect Location to closest FEM point
% Add in FEM stress value to Measured Defect Structure
```

```
%% Map FEM stresses to Defect Locations
function DefectSet = MeasuredDefectMapping(DefectSet,BladeMesh,Radius)

O_x = DefectSet.MeshOrigin(1);
O_y = DefectSet.MeshOrigin(2);
O_z = DefectSet.MeshOrigin(3);

for ii = 1:length(DefectSet.DefectSize)
    % Units: microns
    r_Node = ...
        sqrt((BladeMesh.Nodes(:,2)-(DefectSet.Position(ii,1)+O_x)).^2+...
                    (BladeMesh.Nodes(:,3)-(DefectSet.Position(ii,2)+O_y)).^2+...
                    (BladeMesh.Nodes(:,4)-(DefectSet.Position(ii,3)+O_z)).^2);
    % ID closest point to measured defect location
    [~,ind1] = min(r_Node);
    % Pull stress values assiciated with the closest point
    % Units: MPa
    DefectSet.dStress(ii,:) = ...
        BladeMesh.Freq2.Nom_NodalStressRange(ind1,:);
    DefectSet.dStress(ii,2:5) = ...
        abs(BladeMesh.Freq2.Nom_NodalStressRange(ind1,2:5).*BladeMesh.Freq2.Mod_Scale);

    % ID all nodes within R of measured defect location
    tempInd = find(r_Node<=Radius);
    % ID nodal dStress values
    if isempty(tempInd)
        TempdStress = BladeMesh.Freq2.Nom_NodalStressRange(ind1,:);
    else
        TempdStress = BladeMesh.Freq2.Nom_NodalStressRange(tempInd,:);
    end

    % Pull min/max stress values within assigned measurement error
```

```
    [~,minInd] = min(abs(TempdStress(:,5)));
    [~,maxInd] = max(abs(TempdStress(:,5)));

    DefectSet.min_dStress(ii,:) = abs(TempdStress(minInd,:));
    DefectSet.max_dStress(ii,:) = abs(TempdStress(maxInd,:));

    DefectSet.min_dStress(ii,2:5) = ...
        abs(TempdStress(minInd,2:5)).*BladeMesh.Freq2.Mod_Scale;
    DefectSet.max_dStress(ii,2:5) = ...
        abs(TempdStress(maxInd,2:5)).*BladeMesh.Freq2.Mod_Scale;
end
end
```

1.2.5 Predict Defect Life

```
%% Maj Daniel Miller
% Use the defect and material structures to search for the optimum ...
    number
% of cycles required to fit the modeled defect size and FEM stress ...
    results

% First function finds 2 cycle values that bracket the target FEM stress
% results.  Then checks the half value point to refine the search area
% until the upper and lower bounds are within 1 cycle of eachother.

% Input: Defect Structure, Material Properties Structure
% Output: Defect Structure
function TargetLife = DefectStressSizetoLife(DefectSet,LifeSet,Mat)

%% Set Inital Bounds Around Target Stress
% Initial point for Number of Cycles
```

```
delta = 10;
UpperLimit = 1e10;
% No data point should have fewer cycles than delta

% Pull target stress and defect size for each defect being processed
if LifeSet == 'min'
    D_sig_map = DefectSet.max_dStress(:,5);
elseif LifeSet == 'max'
    D_sig_map = DefectSet.min_dStress(:,5);
elseif LifeSet == 'avg'
    D_sig_map = DefectSet.dStress(:,end);
else
    error('Second function variable needs to: min, max, or avg')
end
% Convert defect size from microns to Meters
a = DefectSet.DefectSize.*1e-6;

% Shape Factor vector
ShapeFactor = DefectSet.ShapeFactor;
% For use on Worst Case Analysis (Y = 0.65 for all defects)
% ShapeFactor = 0.65*ones(size(DefectSet.DefectSize));

% Set up initial points for number of cycles
Cycles(:,1) = delta*ones(length(a),1);
Cycles(:,2) = Cycles(:,1) + 1.618*Cycles(:,1);

Values = SolveForSig(Cycles(:,1),Mat,a,ShapeFactor);
F(:,1) = Values.D_sig;
Values = SolveForSig(Cycles(:,2),Mat,a,ShapeFactor);
F(:,2) = Values.D_sig;
ii = 2;
```

```
% Incrament number of cycles up until target stress is captured
while sum(F(:,ii) > D_sig_map) >0
    ii = ii+1;
    Cycles(:,ii) = Cycles(:,ii-1) + 1.618^(ii-1)*delta;
    Values = SolveForSig(Cycles(:,ii),Mat,a,ShapeFactor);
    F(:,ii) = Values.D_sig;
end

% Set initial Lower Bound, Upper Bound and interval

F = F - D_sig_map;
F(F<=0) = nan;
[val,col] = min(F,[],2);

alpha_L = zeros(length(a),1);
alpha_U = zeros(length(a),1);
for ii = 1:length(a)
    alpha_L(ii) = Cycles(ii,col(ii));
    alpha_U(ii) = Cycles(ii,col(ii)+1);
    if alpha_L(ii) >UpperLimit
        alpha_L(ii) = UpperLimit;
        alpha_U(ii) = UpperLimit;
    end
end
I = alpha_U - alpha_L;

%% Halfing Search To ID Number of Cycles to Hit Target Stress
% While the interval is wider than 1 cycle, check calculated stress
% against target stress, and shrink search area by 1/2
while sum(I > 1) >0
    alpha_a = alpha_L + 0.5*I;
```

```
    Values = SolveForSig(alpha_a,Mat,a,ShapeFactor);
    D_sig_a = Values.D_sig;

    for ii = 1:length(a)
        if D_sig_a(ii) < D_sig_map(ii)
            alpha_U(ii) = alpha_a(ii);
        elseif D_sig_a(ii) > D_sig_map(ii)
            alpha_L(ii) = alpha_a(ii);
        else
            alpha_L(ii) = alpha_a(ii);
            alpha_U(ii) = alpha_a(ii);
        end
    end
    I = alpha_U - alpha_L;
end

% Save out final results
Average = (alpha_U+alpha_L)/2;
Values = SolveForSig(Average,Mat,a,ShapeFactor);
TargetLife.Scale_N_f_BackSolve = Average;
TargetLife.Scale_a_0_BackSolve = Values.a_0;
TargetLife.Scale_a_c_BackSolve = Values.a_c;

end

%% Function
% Input: Number of Cycles (Guess), Material Properties, Defect Size
% Output: Model Parameters (Stored in Structure)
function Values = SolveForSig(N, Mat, a, ShapeFactor)

D_sig_N = 2*Mat.A*N.^Mat.b;
a_c = (2*Mat.K_Ic./(Mat.Y1*D_sig_N)).^2/pi;
```

```
a_0 = (a_c.^(1-Mat.n/2) - ...
    N*(1-Mat.n/2)*Mat.C_0.*(ShapeFactor.*D_sig_N.*sqrt(pi)).^Mat.n).^(1/(1-Mat.n/2));
D_sig = D_sig_N.*sqrt(a_0./(a+a_0));

Values.N = N;
Values.D_sig_N = D_sig_N;
Values.a_c = a_c;
Values.a_0 = a_0;
Values.D_sig = D_sig;
end
```

Bibliography

1. Oak Ridge National Laboratory, *ORNL Researchers Demonstrate New Class of Superalloys For Additive Manufacturing*, 2021.

2. P. Yadav, O. Rigo, C. Arvieu, E. Le Guen, and E. Lacoste, "In situ monitoring systems of the slm process: On the need to develop machine learning models for data processing," *Crystals*, vol. 10, no. 6, p. 524, 2020.

3. K. Solberg and F. Berto, "Notch-defect interaction in additively manufactured inconel 718," *International Journal of Fatigue*, vol. 122, pp. 35–45, 2019.

4. L. Sheridan, *Primary Processing Parameters and Their Influence on Porosity and Fatigue Life of Additively Manufactured Alloy 718*. Ph.D. Dissertation, Wright State University, Dayton, OH, 2020.

5. S. Romano, A. Brückner-Foit, A. Brandão, J. Gumpinger, T. Ghidini, and S. Beretta, "Fatigue properties of alsi10mg obtained by additive manufacturing: Defect-based modelling and prediction of fatigue strength," *Engineering Fracture Mechanics*, vol. 187, pp. 165–189, 2018.

6. J. Homan, "Description of a s-n curve," *Fatec Engineering*, 2018.

7. T. Anderson, *Fracture Mechanics*. Taylor & Francis Group, third edition ed., 2005.

8. S. Beretta, M. Gargourimotlagh, S. Foletti, A. du Plessis, and M. Riccio, "Fatigue strength assessment of "as built" alsi10mg manufactured by slm with different build orientations," *International Journal of Fatigue*, vol. 139, p. 105737, 2020.

9. R. Aigner, S. Pusterhofer, S. Pomberger, M. Leitner, and M. Stoschka, "A probabilistic kitagawa-takahashi diagram for fatigue strength assessment of cast aluminium alloys," *Materials Science and Engineering: A*, vol. 745, pp. 326–334, 2019.

10. S. Romano, S. Beretta, S. Miccoli, and M. Gschweitl, "Probabilistic framework for defect tolerant fatigue assessment of am parts applied to a space component," *ASTM Sel. Tech. Pap.*, vol. 1620, 2019.

11. L. Sheridan, "A modified el-haddad model for versatile defect tolerant design," *International Journal of Fatigue*, vol. 145, p. 106062, 2021.

12. A. E466-15, *Standard Practice for Conducting Force Controlled Constant Amplitude Axial Fatigue Tests of Metallic Materials*. ASTM International, West Conshohocken, PA, 2015.

13. D. G. Miller, "Vibrational analysis of a 12U chassis," MS Thessis, Dept. Aeronautics & Astronautics, AFIT, Wright-Patterson Air Force Base, OH, 2016.

14. L. Sheridan, O. E. Scott-Emuakpor, T. George, and J. E. Gockel, "Relating porosity to fatigue failure in additively manufactured alloy 718," *Materials Science and Engineering: A*, vol. 727, pp. 170 – 176, 2018.

15. M. Tang and P. C. Pistorius, "Oxides, porosity and fatigue performance of alsi10mg parts produced by selective laser melting," *International Journal of Fatigue*, vol. 94, pp. 192–201, 2017.

16. C. Li, Z. Liu, X. Fang, and Y. Guo, "Residual stress in metal additive manufacturing," *Procedia CIRP*, vol. 71, pp. 348 – 353, 2018. 4th CIRP Conference on Surface Integrity (CSI 2018).

17. D. J. Newell, R. P. O'Hara, G. R. Cobb, A. N. Palazotto, M. M. Kirka, L. W. Burggraf, and J. A. Hess, "Mitigation of scan strategy effects and material anisotropy through supersolvus annealing in lpbf in718," *Materials Science and Engineering: A*, vol. 764, p. 138230, 2019.

18. M. Kirka, D. Greeley, C. Hawkins, and R. Dehoff, "Effect of anisotropy and texture on the low cycle fatigue behavior of inconel 718 processed via electron beam melting," *International Journal of Fatigue*, vol. 105, pp. 235–243, 2017.

19. S. Beretta and S. Romano, "A comparison of fatigue strength sensitivity to defects for materials manufactured by am or traditional processes," *International Journal of Fatigue*, vol. 94, pp. 178–191, 2017. Fatigue and Fracture Behavior of Additive Manufactured Parts.

20. A. Fatemi, R. Molaei, S. Sharifimehr, N. Phan, and N. Shamsaei, "Multiaxial fatigue behavior of wrought and additive manufactured ti-6al-4v including surface finish effect," *International Journal of Fatigue*, vol. 100, no. 1, pp. 347–366, 2017.

21. M. Ciavarella and F. Monno, "On the possible generalizations of the kitagawa–takahashi diagram and of the el haddad equation to finite life," *International Journal of Fatigue*, vol. 28, no. 12, pp. 1826–1837, 2006.

22. M. El-Haddad, K. Smith, and T. Topper, "Fatigue crack propagation of short cracks," *Journal of Engineering Materials and Technology*, vol. 101, pp. 42 – 46, 1979.

23. S. Romano, P. Nezhadfar, N. Shamsaei, M. Seifi, and S. Beretta, "High cycle fatigue behavior and life prediction for additively manufactured 17-4 ph stainless steel: Effect of sub-surface porosity and surface roughness," *Theoretical and Applied Fracture Mechanics*, vol. 106, p. 102477, 2020.

24. National Aeronautics And Space Administration, George C. Marshall Space Flight Center, *Standard For Additively Manufactured Spaceflight Hardware By Laser Powder Bed Fusion In Metals*, 2017.

25. T. W. Simpson, "Book review: Additive manufacturing for the aerospace industry," *AIAA Journal*, vol. 58, no. 4, pp. 1901–1902, 2020.

26. P. Zelinski, "What is the role for additive manufacturing in aircraft structural components?," *Additive Manufacturing*, 2019.

27. A. Kestilä, K. Nordling, V. Miikkulainen, M. Kaipio, T. Tikka, M. Salmi, A. Auer, M. Leskelä, and M. Ritala, "Towards space-grade 3d-printed, ald-coated small satellite propulsion components for fluidics," *Additive manufacturing*, vol. 22, pp. 31–37, 2018.

28. W. W. Wits, S. J. Weitkamp, and J. van Es, "Metal additive manufacturing of a high-pressure micro-pump," *Procedia Cirp*, vol. 7, pp. 252–257, 2013.

29. P. Gaudenzi, S. Atek, V. Cardini, M. Eugeni, G. G. Nisi, L. Lampani, M. Pasquali, and L. Pollice, "Revisiting the configuration of small satellites structures in the framework of 3d additive manufacturing," *Acta Astronautica*, vol. 146, pp. 249–258, 2018.

30. M. A. Macchia, "Application of meta-materials for multi-functional satellite bus enabled via additive manufacturing," MS Thessis, Dept. Aeronautics & Astronautics, AFIT, Wright-Patterson Air Force Base, OH, 2019.

31. A. A. Shapiro, J. Borgonia, Q. Chen, R. Dillon, B. McEnerney, R. Polit-Casillas, and L. Soloway, "Additive manufacturing for aerospace flight applications," *AIAA Journal of Spacecraft and Rockets*, pp. 952–959, 2016.

32. S. Romano, A. Brandão, J. Gumpinger, M. Gschweitl, and S. Beretta, "Qualification of am parts: Extreme value statistics applied to tomographic measurements," *Materials & Design*, vol. 131, pp. 32–48, 2017.

33. M. Schimmerohn, M. Bierdel, M. Gulde, D. Sholes, A. Pfaff, M. Pielok, K. Hoschke, and C. Horch, "Additive manufactured structures for the 12u nanosatellite ernst," in *Small Satellite Conference*, (Logan, Utah), pp. SSC18–WKVII–06, Journal of Small Satellites, 2018.

34. B. Horais, L. Love, and R. Dehoff, "The use of additive manufacturing for fabrication of multi-function small satellite structures," in *Small Satellite Conference*, (Logan, Utah), pp. SSC13–III–6, Journal of Small Satellites, 2013.

35. B. Blakey-Milner, P. Gradl, G. Snedden, M. Brooks, J. Pitot, E. Lopez, M. Leary, F. Berto, and A. du Plessis, "Metal additive manufacturing in aerospace: A review," *Materials & Design*, vol. 209, p. 110008, 2021.

36. M. Grasso and B. M. Colosimo, "Process defects and in situ monitoring methods in metal powder bed fusion: A review," *Measurement Science and Technology*, vol. 28, p. 044005, feb 2017.

37. R. Russell, D. Wells, J. Waller, B. Poorganji, E. Ott, T. Nakagawa, H. Sandoval, N. Shamsaei, and M. Seifi, "Qualification and certification of metal additive manufactured hardware for aerospace applications," *Additive Manufacturing for the Aerospace Industry*, pp. 33–66, 2019.

38. Z. Wu, S. Wu, J. Bao, W. Qian, S. Karabal, W. Sun, and P. J. Withers, "The effect of defect population on the anisotropic fatigue resistance of alsi10mg alloy fabricated by laser powder bed fusion," *International Journal of Fatigue*, vol. 151, p. 106317, 2021.

39. M. M. Opgenoord and K. E. Willcox, "Design methodology for aeroelastic tailoring of additively manufactured lattice structures using low-order methods," *AIAA Journal*, vol. 57, no. 11, pp. 4903–4914, 2019.

40. Special Metals Corporation, *Inconel Alloy 719*, 2007.

41. C. Pei, D. Shi, H. Yuan, and H. Li, "Assessment of mechanical properties and fatigue performance of a selective laser melted nickel-base superalloy inconel 718," *Materials Science and Engineering: A*, vol. 759, pp. 278 – 287, 2019.

42. United States Air Force, *U.S. Air Force 2030 Science and Technology Strategy*, 2019.

43. United States Department of Defense, *Mil-Handbook 1783B - Engine Structural Integrity Program*, 2004.

44. J. D. Deaton and R. V. Grandhi, "A survey of structural and multidisciplinary continuum topology optimization: Post 2000," *Structural and Multidisciplinary Optimization*, vol. 49, no. 1, pp. 1–38, 2014.

45. T. Zegard and G. H. Paulino, "Bridging topology optimization and additive manufacturing," *Structural and Multidisciplinary Optimization*, vol. 53, no. 1, pp. 175–192, 2016.

46. A. T. Gaynor and J. K. Guest, "Topology optimization considering overhang constraints: Eliminating sacrificial support material in additive manufacturing through design," *Structural and Multidisciplinary Optimization*, vol. 54, no. 5, pp. 1157–1172, 2016.

47. M. Peto, E. Ramírez-Cedillo, A. Hernández, and H. R. Siller, "Structural design optimization of knee replacement implants for additive manufacturing," *Procedia Manufacturing*, vol. 34, pp. 574–583, 2019.

48. A. Nazir, K. M. Abate, A. Kumar, and J.-Y. Jeng, "A state-of-the-art review on types, design, optimization, and additive manufacturing of cellular structures," *The International Journal of Advanced Manufacturing Technology*, vol. 104, no. 9, pp. 3489–3510, 2019.

49. M. A. El-Sayed, K. Essa, M. Ghazy, and H. Hassanin, "Design optimization of additively manufactured titanium lattice structures for biomedical implants," *The International Journal of Advanced Manufacturing Technology*, vol. 110, no. 9, pp. 2257–2268, 2020.

50. A. Goldin, "Structural dynamic and inherent damping characterization of additively manufactured airfoil components," MS Thesis, Dept. Aeronautics & Astronautics, AFIT, Wright-Patterson Air Force Base, OH, 2020.

51. W. D. Cowie, "Turbine engine structural integrity program/ensip," *Journal of Aircraft*, vol. 12, no. 4, pp. 366–369, 1975.

52. N. Hou, Z. Wen, Q. Yu, and Z. Yue, "Application of a combined high and low cycle fatigue life model on life prediction of sc blade," *International Journal of Fatigue*, vol. 31, no. 4, pp. 616–619, 2009.

53. J. Huo, D. Sun, H. Wu, W. Wang, and lin Xue, "Multi-axis low-cycle creep/fatigue life prediction of high-pressure turbine blades based on a new critical plane damage parameter," *Engineering Failure Analysis*, vol. 106, p. 104159, 2019.

54. S. P. Murray, K. M. Pusch, A. T. Polonsky, C. J. Torbet, G. G. Seward, N. Zhou, S. A. Forsik, P. Nandwana, M. M. Kirka, R. R. Dehoff, *et al.*, "A defect-resistant co–ni superalloy for 3d printing," *Nature communications*, vol. 11, no. 1, pp. 1–11, 2020.

55. L. Panning, W. Sextro, and K. Popp, "Spatial dynamics of tuned and mistuned bladed disks with cylindrical and wedge-shaped friction dampers," *International Journal of Rotating Machinery*, vol. 9, no. 3, pp. 219–228, 2003.

56. A. Chudzik and B. WArdA, "Fatigue life prediction of a radial cylindrical roller bearing subjected to a combined load using fem," *Eksploatacja i Niezawodność*, vol. 22, no. 2, 2020.

57. S. Romano, S. Miccoli, and S. Beretta, "A new fe post-processor for probabilistic fatigue assessment in the presence of defects and its application to am parts," *International Journal of Fatigue*, vol. 125, pp. 324 – 341, 2019.

58. L. Huynh, J. Rotella, and M. D. Sangid, "Fatigue behavior of in718 microtrusses produced via additive manufacturing," *Materials & Design*, vol. 105, pp. 278 – 289, 2016.

59. J.-P. Kruth, L. Froyen, J. Van Vaerenbergh, P. Mercelis, M. Rombouts, and B. Lauwers, "Selective laser melting of iron-based powder," *Journal of Materials Processing Technology*, vol. 149, no. 1-3, pp. 616–622, 2004.

60. M. Daňa, I. Zetková, J. Mach, *et al.*, "Mechanical properties of inconel alloy 718 produced by 3d printing using dmls," *Manufacturing Technology*, vol. 18, no. 4, pp. 559–562, 2018.

61. S. Li, S. Yuan, J. Zhu, W. Zhang, H. Zhang, and J. Li, "Multidisciplinary topology optimization incorporating process-structure-property-performance relationship of additive manufacturing," *Structural and Multidisciplinary Optimization*, vol. 63, no. 5, pp. 2141–2157, 2021.

62. H. Gong, *Generation and Detection of Defects in Metallic Parts Fabricated by Selective Laser Melting and Electron Beam Melting and Their Effects on Mechanical Properties*. Ph.D. Dissertation, University of Louisville, Louisville, KY, 2013.

63. J.-B. Forien, N. P. Calta, P. J. DePond, G. M. Guss, T. T. Roehling, and M. J. Matthews, "Detecting keyhole pore defects and monitoring process signatures during laser powder bed fusion: A correlation between in situ pyrometry and ex situ x-ray radiography," *Additive Manufacturing*, vol. 35, p. 101336, 2020.

64. International Symposium on Electromachining, *Feedback Control of Selective Laser Melting*, University of Nebraska-Lincoln, apr 2007.

65. H. Gong, K. Rafi, H. Gu, T. Starr, and B. Stucker, "Analysis of defect generation in ti-6al-4v parts made using powder bed fusion additive manufacturing processes," *Additive Manufacturing*, vol. 1, pp. 87–98, 2014.

66. L. Sheridan, J. E. Gockel, and O. E. Scott-Emuakpor, "Primary processing parameters, porosity production, and fatigue prediction for additively manufactured alloy 718," *Journal of Materials Engineering and Performance*, vol. 28, no. 9, pp. 5387–5397, 2019.

67. M. Ni, C. Chen, X. Wang, P. Wang, R. Li, X. Zhang, and K. Zhou, "Anisotropic tensile behavior of in situ precipitation strengthened inconel 718 fabricated by additive manufacturing," *Materials Science and Engineering: A*, vol. 701, pp. 344 – 351, 2017.

68. Y. Hu, S. Wu, Z. Wu, X. Zhong, S. Ahmed, S. Karabal, X. Xiao, H. Zhang, and P. Withers, "A new approach to correlate the defect population with the fatigue life of selective laser melted ti-6al-4v alloy," *International Journal of Fatigue*, vol. 136, p. 105584, 2020.

69. A. Fatemi, R. Molaei, J. Simsiriwong, N. Sanaei, J. Pegues, B. Torries, N. Phan, and N. Shamsaei, "Fatigue behaviour of additive manufactured

materials: An overview of some recent experimental studies on ti-6al-4v considering various processing and loading direction effects," *Fatigue & fracture of engineering materials & structures*, vol. 42, no. 5, pp. 991–1009, 2019.

70. J. Gumpinger, A. D. Brandão, E. Beevers, T. Rohr, T. Ghidini, S. Beretta, and S. Romano, *Expression of Additive Manufacturing Surface Irregularities Through a Flaw-Based Assessment*. ASTM International, 2020.

71. P. D'Antuono, "An analytical relation between the weibull and basquin laws for smooth and notched specimens and application to constant amplitude fatigue," *Fatigue & Fracture of Engineering Materials & Structures*, vol. 43, no. 5, pp. 991–1004, 2020.

72. Y. Murakami, "Analysis of stress intensity factors of modes i, ii and iii for inclined surface cracks of arbitrary shape," *Engineering Fracture Mechanics*, vol. 22, no. 1, pp. 101–114, 1985.

73. Y. Murakami, *Metal Fatigue: Effects of Small Defects and Nonmetallic Inclusions*. Academic Press, 2019.

74. Y. Yamashita, T. Murakami, R. Mihara, M. Okada, and Y. Murakami, "Defect analysis and fatigue design basis for ni-based superalloy 718 manufactured by selective laser melting," *International Journal of Fatigue*, vol. 117, pp. 485–495, 2018.

75. L. Sheridan, J. E. Gockel, and O. E. Scott-Emuakpor, "Stress-defect-life interactions of fatigued additively manufactured alloy 718," *International Journal of Fatigue*, vol. 143, p. 106033, 2021.

76. D. Taylor and J. Knott, "Fatigue crack propagation behaviour of short cracks; the effect of microstructure," *Fatigue & Fracture of Engineering Materials & Structures*, vol. 4, pp. 147 – 155, 1981.

77. D. Miller, R. Kemnitz, R. Grandhi, and L. Sheridan, "Fatigue life modeling and experimental validation of additively manufactured turbine blade with respect to defect size and location," in *SciTech*, (San Diego, CA), pp. AIAA–2022–0671, AIAA, 2022.

78. A. Du Plessis and S. Beretta, "Killer notches: The effect of as-built surface roughness on fatigue failure in alsi10mg produced by laser powder bed fusion," *Additive Manufacturing*, vol. 35, p. 101424, 2020.

79. S. Beretta, M. Carboni, and M. Madia, "Modelling of fatigue thresholds for small cracks in a mild steel by "strip-yield" model," *Engineering Fracture Mechanics*, vol. 76, no. 10, pp. 1548–1561, 2009.

80. J. M. Brown, A. A. Kaszynski, D. L. Gillaugh, E. B. Carper, and J. A. Beck, "Optimization of airfoil blend limits with as-manufactured geometry finite element models," *Journal of Engineering for Gas Turbines and Power*, vol. 144, no. 3, 2022.

81. D. L. Gillaugh, A. A. Kaszynski, J. M. Brown, J. A. Beck, and J. C. Slater, "Mistuning evaluation comparison via as-manufactured models, traveling wave excitation, and compressor rigs," *Journal of Engineering for Gas Turbines and Power*, vol. 141, no. 6, 2019.

82. "Inconel alloy 718," tech. rep., Special Metals Corporation, 2007.

83. A. Kaszynski, J. Brown, and J. Beck, "Experimental validation of an optically measured geometric mistuning model using a system id approach," in *17th AIAA Non-Deterministic Approaches Conference*, (Kissimmee, FL), p. 1371, 2015.

84. V. Popovich, E. Borisov, A. Popovich, V. S. Sufiiarov, D. Masaylo, and L. Alzina, "Functionally graded inconel 718 processed by additive manufacturing: Crystallographic texture, anisotropy of microstructure and mechanical properties," *Materials & Design*, vol. 114, pp. 441–449, 2017.

85. P. S. Prevéy, "The effect of cold work on the thermal stability of residual compression in surface enhanced in718," tech. rep., LAMBDA RESEARCH CINCINNATI OH, 2000.

86. D. J. Munk and J. D. Miller, "Topology optimization of aircraft components for increased sustainability," *AIAA Journal*, vol. 60, no. 1, pp. 445–460, 2022.

87. W. Sisson, P. Karve, and S. Mahadevan, "Digital twin approach for component health-informed rotorcraft flight parameter optimization," *AIAA Journal*, pp. 1–14, 2021.

88. R. d'Ippolito, S. Donders, M. Hack, G. Van der Linden, D. Vandepitte, and D. Moens, "Reliability-based design of a slat-track fatigue life using mesh morphing technology," *AIAA journal*, vol. 46, no. 1, pp. 154–165, 2008.

89. M. A. Ba-Abbad, R. K. Kapania, and E. Nikolaidis, "Reliability-based structural optimization of an elastic-plastic beam," *AIAA journal*, vol. 41, no. 8, pp. 1573–1582, 2003.

90. I. 25178-2, *Geometrical Product Specifications (GPS) - Surface Texture: Areal - Part 2: Terms, Definitions and Surface Texture Parameters*. International Organization for Standardization, Geneva, Switzerland, 2012.

91. A. 2774-G, *Heat Treatment Nickel Alloy and Cobalt Alloy Parts*. SAE Technical Standards Board, 2020.

92. O. Scott-Emuakpor, M.-H. H. Shen, T. George, C. J. Cross, and J. Calcaterra, "Development of an improved high cycle fatigue criterion," *Journal of Engineering for Gas Turbines and Power*, vol. 129, pp. 162–169, 2007.

93. D. C. Maxwell and T. Nicholas, "A rapid method for generation of a haigh diagram for high cycle fatigue," in *Fatigue and Fracture Mechanics: 29th Volume*, ASTM International, 1999.

94. Y. Nadot, C. Nadot-Martin, W. H. Kan, S. Boufadene, M. Foley, J. Cairney, G. Proust, and L. Ridosz, "Predicting the fatigue life of an alsi10mg alloy manufactured via laser powder bed fusion by using data from computed tomography," *Additive Manufacturing*, vol. 32, p. 100899, 2020.

95. D. Miller, R. Kemnitz, R. Grandhi, and L. Sheridan, "Fatigue life model using defect size, stress, and life validated by axial and bending vibration testing," in *Aviation Conference*, (Chicago, Il), pp. AIAA–2022–0671, AIAA, 2022.

96. National Aeronautics And Space Administration, NASA Goddard Space Flight Center, *General Environmental Verification Standard (GEVS) For GSFC Flight Programs and Projects*, 2013.

97. NASA, "Mars oddyssey: Launch sequence description," 2020.

98. M. H. Lee, *Fatigue Life, Fatigue Crack Propagation and Fracture Toughness Study of 7075 Aluminum Alloy Subjected to Thermomechanical Processing.* Ph.D. Dissertation, Oregon State University, Corvallis, OR, 1984.

99. N. T. Aboulkhair, M. Simonelli, L. Parry, I. Ashcroft, C. Tuck, and R. Hague, "3d printing of aluminium alloys: Additive manufacturing of aluminium alloys using selective laser melting," *Progress in materials science*, vol. 106, p. 100578, 2019.

100. R. S. Haridas, S. Thapliyal, P. Agrawal, and R. S. Mishra, "Defect-based probabilistic fatigue life estimation model for an additively manufactured aluminum alloy," *Materials Science and Engineering: A*, vol. 798, p. 140082, 2020.

101. ASM, "Metals handbook vol. 2," *Properties and Selection: Nonferrous Alloys and Special-Purpose Materials, Atlanta: ASM International*, 1990.

102. R. Jones, J. Cizek, O. Kovarik, J. Lang, A. Ang, and J. G. Michopoulos, "Describing crack growth in additively manufactured scalmalloy," *Additive Manufacturing Letters*, vol. 1, p. 100020, 2021.

103. I. Maskery, N. Aboulkhair, M. Corfield, C. Tuck, A. Clare, R. K. Leach, R. D. Wildman, I. Ashcroft, and R. J. Hague, "Quantification and characterisation of porosity in selectively laser melted al-si10-mg using x-ray computed tomography," *Materials Characterization*, vol. 111, pp. 193–204, 2016.

REPORT DOCUMENTATION PAGE

Form Approved
OMB No. 0704–0188

1. REPORT DATE *(DD–MM–YYYY)*	2. REPORT TYPE	3. DATES COVERED *(From — To)*
15–09–2022	Doctoral Dissertation	Sept 2019 — Sept 2022

4. TITLE AND SUBTITLE

FINITE FATIGUE LIFE PREDICTION OF ADDITIVELY MANUFACTURED AIRCRAFT ENGINE TURBINE BLADE FOR INTERNAL DEFECT SIZE AND LOCATION

5a. CONTRACT NUMBER

5b. GRANT NUMBER

5c. PROGRAM ELEMENT NUMBER

6. AUTHOR(S)

Miller, Daniel G, Maj, USAF

5d. PROJECT NUMBER

5e. TASK NUMBER

5f. WORK UNIT NUMBER

7. PERFORMING ORGANIZATION NAME(S) AND ADDRESS(ES)

Air Force Institute of Technology
Graduate School of Engineering and Management (AFIT/EN)
2950 Hobson Way
WPAFB OH 45433-7765

8. PERFORMING ORGANIZATION REPORT NUMBER

AFIT-ENY-DS-22-S-132

9. SPONSORING / MONITORING AGENCY NAME(S) AND ADDRESS(ES)

Intentionally Left Blank

10. SPONSOR/MONITOR'S ACRONYM(S)

11. SPONSOR/MONITOR'S REPORT NUMBER(S)

12. DISTRIBUTION / AVAILABILITY STATEMENT

DISTRIBUTION STATEMENT A:
APPROVED FOR PUBLIC RELEASE; DISTRIBUTION UNLIMITED.

13. SUPPLEMENTARY NOTES

14. ABSTRACT

Current fatigue life modeling techniques with respect to defects emphasize the dependence on the defect size with respect to fatigue life, but does not account for the effects of where a defect might be located. This research outlines a process to include defect location into the model analysis for a more precise prediction of the number of cycles to failure and where the finial failure could occur within a component. The focus is on a turbine blade structure using IN718 subjected to a pure vibratory load. The basic model predicts component life using a stress map from the frequency analysis of the developed Finite Element Model (FEM) and synthetically generated defect sizes and location. Test specimen printed in IN718 are used to create experimental data to validate the model parameters, defect distributions, and predictions. The proposed results will be a map denoting the critical locations that may cause failure and predictions of fatigue life when both defect size and location are taken into consideration.

15. SUBJECT TERMS

Additive Manufacturing, IN718, Fatigue Life, El-Haddad Model, Finite Element Model

16. SECURITY CLASSIFICATION OF:			17. LIMITATION OF ABSTRACT	18. NUMBER OF PAGES	19a. NAME OF RESPONSIBLE PERSON
a. REPORT	b. ABSTRACT	c. THIS PAGE			Dr. Ramana Grandhi, AFIT/ENY
U	U	U	U	197	19b. TELEPHONE NUMBER *(include area code)* (937)255-3636 x4723; Ramana.Grandhi@afit.edu